Distances, Masses, Radii, and Metallicities of the Small Stars in the Solar Neighborhood

Citation

Dittmann, Jason. 2016. Distances, Masses, Radii, and Metallicities of the Small Stars in the Solar Neighborhood. Doctoral dissertation, Harvard University, Graduate School of Arts & Sciences.

Distances, Masses, Radii, and Metallicities of the Small Stars in the Solar Neighborhood

A dissertation presented

by

Jason Adam Dittmann

to

The Department of Astronomy

in partial fulfillment of the requirements

for the degree of

Doctor of Philosophy

in the subject of

Astronomy & Astrophysics

Harvard University

Cambridge, Massachusetts

April 2016

Dissertation Advisor: Professor David Charbonneau Jason Adam Dittmann

Distances, Masses, Radii, and Metallicities of the Small Stars in the Solar Neighborhood

Abstract

Data from the NASA *Kepler* spacecraft indicate that small planets are common around the smallest main sequence stars (M dwarfs). Rocky planets transiting M dwarfs will be the best targets for atmospheric characterization with the next generation of scientific instruments. Ground based transit and radial velocity surveys, and the upcoming NASA *TESS* mission are expected to reveal the transiting terrestrial exoplanets that are nearest to the Sun. Understanding these worlds requires that we first understand their host stars. In this thesis, I present better estimates of the distances, masses, radii, and metallicities of these target stars.

I used data from the MEarth-North transit survey to obtain trigonometric distances to 1507 mid-to-late M dwarfs with a precision of 5 milliarcseconds. I use these distance measurements to obtain better estimates of the masses and radii of these stars than available from photometry alone, and prioritize targets to monitor at high cadence for transiting planets. I find that the M dwarf census in the northern hemisphere is mostly complete to a distance of 25 parsecs for stars of spectral type M5.5V and earlier, and mostly complete for stars earlier than M7.0V out to 20 parsecs.

I present calibrated *MEarth* optical photometry of 1844 MEarth-North targets with a typical precision of 1.5%. By combining these measurements with trigonometric distances, spectroscopic metallicities, and extant near infrared (NIR) magnitudes, I derive a color-magnitude-metallicity relation with a precision of 0.1 dex. I find that the median metallicity for Solar Neighborhood M dwarfs is [Fe/H] $= -0.030 \pm 0.008$, indistinguishable from the solar neighborhood G dwarfs.

I present the MEarth-South discovery of LP 661-13, a low-mass double lined eclipsing binary system with an orbital period of 4.7 days. I determine the component masses to be 0.3050 ± 0.0056 and 0.1937 ± 0.0027 $M_\odot$ and the radii to be 0.3192 ± 0.0037 and 0.2159 ± 0.0061 $R_\odot$. While each component is marginally consistent with stellar models, the sum of the radii is well constrained and is inflated 5% compared to stellar models, which cannot be ascribed to metallicity or age effects. LP 661-13 joins the small sample of low-mass stars with precisely measured masses and radii that serves as a robust test of models of fully convective dwarf stars.

I present calibrated *griz* photometry of 150 of the MEarth-North target stars with a typical precision of 1%. I find that no combination of *griz* filters alone can reliably determine the metallicity of an M dwarf. However, interpolation in the $(g - i,\, i - K)$ color plane can estimate the metallicity with a typical standard deviation of 0.1 dex. This precision is comparable to that from NIR spectroscopic methods that have been recently developed. Overlap between the upcoming Large Synoptic Survey Telescope (LSST) sources and the VISTA Hemisphere Survey sources will provide a sample of M dwarfs with estimated metallicities that can in turn be used as a chemical probe of the Milky Way Galaxy.

Contents

Acknowledgments

I thank my advisor, David Charbonneau, for his support as my thesis advisor during these past 5 years. I thank him for taking the time to teach me to be the type of scientist I had always hoped to be. I thank him for pushing me to take on projects that at first seemed daunting and to stay with them until the finish. It has been a privilege to work under him as a graduate student, and I hope one day to be half as inspiring a mentor as he has been to me.

I thank Jonathan Irwin for making this thesis possible. From keeping 16 telescopes working, to teaching me so many things about M dwarf stars, to always being willing to share a beer; nothing describe in this thesis would have happened without his input, support, and blood, sweat and tears.

I thank Alicia Soderberg for her patience in teaching an exoplanet-minded graduate student about explosions, and showing me that low mass can mean up to 10 times the mass of the Sun. Her patience as she helped me broaden my research horizon has made me a better, more well-rounded scientist and I am grateful for the opportunity that she provide me.

I thank the other members of the MEarth team - Zachory Berta-Thompson and Elisabeth Newton for their support during the past 6 years. The journey of hunting for small planets around small stars would not have been the same without Zach and Elisabeth as companions, and I would not have wanted to do it with any other people.

I thank my committee - David Latham, Alyssa Goodman, John Johnson, and Todd Henry for their support, ideas, and input during this thesis. It was always a joy to run into Todd at a conference and to discuss all things within 10, 20, or even 50 parsecs.

I thank my undergraduate mentors - Laird Close, Drew Milsom, Donald Huffman, Juan Restrepo, and Betsy Green, for preparing me for grad school and offering their mentorship and support as I began my research career. I thank Betsy Green for first teaching me to use a telescope and for supporting my first foray into exoplanet research. I thank Laird Close for teaching me on as his undergraduate student, for preparing me for research, and for his unending support. I thank Juan Restrepo for taking me on as a freshman undergraduate student in oceanography theory, and for supporting me when I fell down the exoplanet rabbit-hole. I thank Drew Milsom for his mentorship and for his no-nonsense attitude. He has shaped me as a student and challenged me as a scientist. I thank Donald Huffman for teaching me laboratory techniques and allowing me to build an atmospheric science instrument almost independently. He created in me a love and desire for laboratory work that I hope to foster in the future and I would not have embarked on this path without him.

I thank the astronomy graduate students for the support, experiences, and - of course - beer. They have made the hard parts of grad school easier and the easy parts of grad school more fun.

I thank my family for their support of me as I continued to stay in school, and never said that 21st grade was large enough. I particularly thank my godmother, Liz, for instilling in me at a young age a love of science and curiosity about the world. Even though perhaps owning a planet and studying dinosaurs might have been better, I hope she is ok with me studying planets and having a pet dinosaur.

Finally, I thank my partner Rachelle Baker for her support through undergrad, a

3000 mile journey, and a 6 year adventure in science. There is no one else in the world I would want to have this journey with, and I look forward to many more years of science, adventure, and celebration. This thesis is as much her journey as mine, and this thesis would have ended at these acknowledgements without her input.

Chapter 1

Introduction

In 2010, I came to Harvard University from the University of Arizona to begin my dissertation research in the field of exoplanets. At Arizona, I had conducted several studies of hot Jupiters, searching for transit timing variations (Dittmann et al. 2009b,a, 2010, 2012). At that time, NASA's *Kepler* spacecraft had only just begun collecting data and discovering the underlying statistical population of planets from large gas giants to small rocky bodies. During my six years at Harvard University, I have worked primarily with the MEarth Project (Nutzman & Charbonneau 2008). MEarth aims to uncover the nearby, rocky planets around the closest, smallest stars to the Sun. It is these planets that will be most amenable to future characterization. However, I realized that one major bottleneck in the search for these planets is our understanding of their host stars and that for the foreseeable future our understanding of the host star and our understanding of exoplanets will be intertwined. With this problem in mind, I set out to characterize the nearby, low-mass stars, as these stars are the optimal planet hosts and the planets they harbor will be intensely studied over the coming decades.

Our understanding and method of studying exoplanets is fundamentally different than how we study the planets in our Solar System. No spacecraft has ever flown past an exoplanet and no probe has ever been dropped into an exoplanet's atmosphere. Only a handful of the thousands of exoplanets discovered to date have ever been directly observed. The detection and study of exoplanets has largely been carried out through indirect means, particularly through the radial velocity and the transit techniques. Both methods require extracting information about the planetary system through photons that originated in the star. Therefore, it is important to keep in mind that our understanding of exoplanets is facilitated by and limited by our understanding of their host stars.

1.1 The Role of Stars in Shaping Our Understanding of Planets

The presence of multiple bodies in a stellar system cause all the objects in the system to orbit around their common center of mass. If the orbit is not perpendicular to the sky, for portions of the orbit the star is moving radially towards and away from the Earth, producing a periodic Doppler shift in its spectrum. For binary star systems, this effect can be quite dramatic, with each stellar component's spectrum shifting several km s^{-1}. However, for less massive bodies like planets, this effect can still be reliably observed. The amplitude of the radial velocity signal from a star's doppler wobble is sensitive to the masses of the planet (M_p), star (M_*), and the inclination of the orbit (i) in the plane of the sky. With only a radial velocity curve, it is possible to measure only the quantity $M_p \sin i/(M_p + M_\star)^{2/3}$. Improvements in the RV precision in instrumentation can allow us to detect smaller mass planets but also higher mass planets with smaller orbital inclinations. For 51 Peg b, a Jupiter mass object with an orbital period of 4.2 days, the radial velocity of the star has an amplitude of 56 m s^{-1} (Mayor & Queloz 1995). Recent advances in RV spectroscopy (Iodine cells, instrument stabilization, for example) have demonstrated m s^{-1} precision, and work is currently ongoing to refine these techniques and others further. Each improvement in RV precision allows us to measure masses more precisely and to start measuring lower mass companions.

Discovering lower mass planets requires more precise measurements, and in pursuit of these objects new instruments, like the HARPS spectrograph (Rupprecht et al. 2004), Automated Planet Finder (Radovan et al. 2014), and the Planet Finder Spectrograph (Crane et al. 2010), among others, have been developed. Since its inception in 2003, HARPS has searched for extrasolar planets in the Southern hemisphere (Faria et al. 2016), probed the atmosphere of giant plant HD 189733b (Wyttenbach et al. 2015), and provided follow up observations to small transiting planets (Berta-Thompson et al. 2015). A copy of HARPS in the northern hemisphere, HARPS-N (Cosentino et al. 2012), began operations in 2012. In addition to discovering planets around northern hemisphere stars, HARPS-N has been hunting for long period planets in systems already known to harbor planets through the GAPS program (Biazzo et al. 2015), hunted for rocky planets around nearby stars (Motalebi et al. 2015), observed the Sun as a star in order to better understand the astrophysical noise inherent in RV observations (Dumusque et al. 2015), and provided important follow-up observations for planets discovered via the transit method by NASA's *Kepler* mission (Hébrard et al. 2013; Dumusque et al. 2014; Gettel et al. 2016).

These systems that show a transiting geometry are very valuable as we are given additional observables: the depth of the transit, the duration of the ingress and egress, and the total duration of the transit. The depth of the transit light curves tells us the radius of the planet, but only *relative to the radius of the star.* The transit duration and the duration of the ingress and egress of the transit can tell us the inclination of the planet's orbit and the mean density of the star. The transiting geometry also enables transmission spectroscopy studies while the planet is transiting the star (Seager & Sasselov 2000; Charbonneau et al. 2002; Moutou et al. 2001; Snellen 2004)

The first exoplanet system discovered to exhibit transiting geometry was HD 209458b (Charbonneau et al. 2000). Following this discovery, ground-based wide-field surveys such as HAT (Bakos et al. 2002), WASP (Pollacco et al. 2006), XO (McCullough et al. 2005), TrES (Dunham et al. 2004), and KELT (Pepper et al. 2007), among others, began operating to attempt to discover more of these systems. Together the WASP survey (Pollacco et al. 2006) and HAT survey (Bakos et al. 2002), as well as their more recent southern hemisphere counterparts (Hellier et al. 2011; Penev et al. 2013) have discovered hundreds of transiting planets, nearly all hot Jupiters. These systems were the tip of the exoplanet iceberg and after the launch of NASA's *Kepler* mission we know of thousands of planetary systems (Coughlin et al. 2015). *Kepler*'s unprecedented precision and 4-year baseline has allowed us to investigate the occurrence rates of rocky and gas giant planets in close-in orbits around main sequence stars. Howard et al. (2012) found that 13% of FGK stars have a $2 - 4$ $R_\oplus$ planet with a period less than 85 days and that this fraction increases for cooler stars. Fressin et al. (2013) found that 16.5% of FGK stars have a planet between 0.8 and 1.25 $R_\oplus$ with an orbital period less than 85 days. A further study out to longer periods found that there are approximately 0.77 planets per star between 0.75 $R_\oplus$ and 2.5 $R_\oplus$ with orbital periods between 50 and 300 days (Burke et al. 2015). In the M dwarf regime, Petigura et al. (2013) found that there are approximately 0.48 planets per M dwarf with a period less than 50 days. This rate was revised slightly upwards by Dressing & Charbonneau (2015) who found that there are approximately 0.56 planets with radii between 1 and 1.5 $R_\oplus$ per M dwarf that have an orbital period less than 50 days. While the projected value for the number of habitable Earth-sized planets per star varies slightly, it is clear that *small, rocky planets are common* in the Galaxy, and that this occurrence rate persists towards lower mass stars and may even be larger than for solar type stars. It is towards this lower mass end that the field has now turned, in the hopes of discovering a habitable planet suited for subsequent observations to determine whether or not it is also inhabited. Moving away from Sun-like stars poses its own set of challenges, which must be overcome.

1.1.1 The Push Towards M Dwarfs and the Challenges they Pose

For exoplanetary systems, the fundamental properties of the planet can be inferred only relative to the properties of its host star, and therefore our understanding of planetary astrophysics hinges on our understanding of stellar astrophysics. More crucially, from a feasibility standpoint, if we want to characterize smaller and less massive planets, both the observed radial velocity amplitude and transit depth become larger for smaller host stars. The radial velocity amplitude of the Sun due to the Earth is 9 cm s^{-1}, and its transit depth is only 84 parts per million. A planet the size of the Earth receiving the same total amount of energy that the Earth receives from the Sun orbiting a star with 0.2 $M_\odot$ would exert a radial velocity amplitude of 65 cm s^{-1} and have a transit depth of

2100 parts per million.

Searching for planets around stars smaller than the Sun has an additional striking advantage - the period of a planet with an equilibrium temperature that can support the existence of liquid water on its surface is much smaller than one year. Because the planet would transit more often, this significantly decreases the time it takes to collect enough data to detect the planet and collect more detailed follow-up data. Furthermore, planets that reside closer to their host stars have a much wider range of angles in which they will show transiting geometries. The criterion for a planet to show a transiting geometry is

$$\sin(90 - i) < \frac{R_*}{a} \tag{1.1}$$

where i is the inclination of the orbit in the plane of the sky, R_* is the radius of the host star, and a is the semi-major axis of the planet. For a star with 0.2 $M_\odot$, its radius would be approximately 5× smaller than the Sun's, but the habitable zone will be 20 times closer to the star than the Earth is to the Sun, increasing the range of orbital inclinations that would show transiting geometry.

From signal to noise and accessibility standpoints, smaller stars are better hunting grounds for searching for rocky habitable planets, and understanding their masses, radii, luminosities, and other physical properties is crucial in order to understand the planetary systems that orbit them. Out of every 10 stars in the Milky Way, 7 of them are M dwarfs; 248 of the 366 stars within 10 parsecs of the Sun are M dwarfs (Henry et al. 2006). Yet, of the approximately 6000 stars in night sky visible to the naked eye, *none* of them are M dwarfs. This fact underscores the reality that M dwarfs - the majority of stars and planet hosting stars - are less luminous than stars like the Sun, and the potentially habitable planets that orbit them are subject to different radiative environments than the Earth.

If we are to search for habitable planets and eventually life in these systems, then we must begin by understanding the star whose light we will be observing in our telescope. The M dwarfs make up the lowest mass end of the stellar spectral sequence, with M0 beginning at approximately 0.6 $M_\odot$ (Tarter et al. 2007). The M dwarf spectral sequence ends when a star is no longer massive enough to sustain nuclear fusion in its core, at approximately 0.08 $M_\odot$ (Dieterich et al. 2014), although this boundary can change depending on metallicity and other factors (Helling & Casewell 2014). This mass range is equal to the mass range spanned by the entire F, G, and K spectral sequences combined. Therefore, it isn't surprising that major structural changes occur between earlier, more massive M dwarfs and later, less massive M dwarfs, even though both are classified as an M spectral type star.

Down this mass sequence, the rate of nuclear burning decreases. Consequently, the energy output of the star drops and less energy needs to be transported from the core to the surface of the star (Chabrier et al. 1996). At approximately 0.33 $M_\odot$, convection can more efficiently transport energy towards the surface of the star throughout its interior, and stars of this mass and lower are fully convective. This contrasts with solar type stars, whose interiors transport energy largely through radiative diffusion.

The fully convective nature of such a star has consequences for the behavior of the star over its lifetime, and also for the environment a planet may find itself in. For stars like the Sun, the magnetic field is generated at the interface between their outer convective zones and their inner radiative zones (Solanki et al. 2006). Since mid-to-late M dwarfs lack radiative zones (and therefore they have no convective-radiative interface), it was thought that M dwarfs would only have weak magnetic fields (Saar 1996). However, observations have indicated that M dwarfs are capable of generating large-scale magnetic fields (Donati et al. 2006). By observing Zeeman splitting with high resolution spectrographs, M dwarfs have been shown to be able to have magnetic fields with strengths of several kiloGauss (Johns-Krull & Valenti 1996). These intense magnetic fields can also produce highly energetic flares. Combined with a close-in habitable zone, any habitable planets around M dwarfs will have to contend with the effects of this intense radiation, including atmospheric stripping (Khodachenko et al. 2007), although these effects may not ultimately render the planet uninhabitable (Tarter et al. 2007).

Regardless of the difficulty M dwarfs present to the planets that may orbit around them, in order to characterize and understand those planets we will need a way to measure or infer both the mass and the radius of the host star. For main sequence stars, stellar models have been able to predict the mass and radius of a star given its measured flux with accuracies of 1 - 2 percent (Andersen 1991). These models are also able to account for effects of age and metallicity (Andersen 1991). In contrast, the mass-luminosity relationship for M dwarfs is not as precisely measured. Delfosse et al. (2000) used a sample of M dwarfs adopted from Henry & McCarthy (1993) and Henry et al. (1999a) that had accurate distance measurements and dynamical mass measurements in order to measure the mass-luminosity relation for low mass stars. They found that an M dwarf's mass is most directly correlated with its absolute (distance corrected) infrared magnitude in the 2 Micron All Sky Survey (2MASS) K_s band. They found that optical magnitudes do not correlate as well with mass, as metallicity also affects the optical magnitude, the low temperatures present in M dwarf stellar atmospheres, molecules begin to form and blanket the optical wavelengths with absorption lines and suppress the flux (Allard et al. 1997; Baraffe et al. 1998).

Once we obtain a mass through a distance measurement and a magnitude measurement, how do we estimate the radius of the star? Directly measuring the radius of a single star is very difficult, as resolving the disk requires the use of an interferometer, although several stars have been measured this way, including GJ 176 with a radius of $0.4525 \pm 0.0221\ R_\odot$ and GJ 876 with a radius of $0.3661 \pm 0.0059\ R_\odot$ (Boyajian et al. 2015). Unfortunately, this technique requires the star to be bright at optical wavelengths, which makes the number of viable M dwarfs to have been measured through this technique much smaller than for solar-type stars.

Typically, radius measurements of stars are done through the use of eclipsing binary systems, where both stars are also detected through spectroscopy (so that a radial velocity orbit can constrain both of their masses). These systems can then be used to calibrate and test models of stellar structure and atmospheres. While the stellar models can accurately reproduce the stellar mass-radius relation for stars that have similar masses to the Sun (Allard et al. 1997), these models become less accurate towards lower masses (Torres 2013). In particular, low mass stars seem to have larger radii and cooler temperatures than stellar models would predict. This becomes important for planets discovered around these systems, as a bigger star means the transiting planet is also bigger than we initially believed and may no longer be rocky or habitable.

The observed differences between models and observations become more pronounced below 0.35 solar masses, where M dwarfs become fully convective (Chabrier & Baraffe 1997; Baraffe et al. 2015). This discrepancy cannot be explained as an observational bias associated with tidal forces between the eclipsing stars due to their proximity (as most eclipsing binary systems have short periods). Recently discovered eclipsing binary systems with periods of 41 days (Kepler-16AB Doyle et al. (2011), LSPM J1112+7626 Irwin et al. (2011b)), well outside the tidal radius, have shown radii that are also inflated relative to stellar models. Further progress into uncovering what physical processes affect the stellar mass-radius relation requires the discovery and detailed characterization of additional systems (at different periods, composition, and activity levels) in order to disentangle various effects that all might be contributing to our underestimation of M dwarf radii.

In order to build a planet around a star, one requires the raw metallic materials necessary to assemble the planet. Stars and gas giant planets are dominated by Hydrogen and Helium, the elements that make up the vast majority of the Universe. Earth and other rocky planets, on the other hand, are dominated by heavier elements. However, it's not currently known how efficient the planet formation process is (Armitage 2003; Muñoz et al. 2016). Fischer & Valenti (2005) investigated this question and found that fewer than 3% of solar-type stars with metallicity lower than that of the Sun have a giant planet with a period of 4 years or less and an RV semi amplitude of 30 m s^{-1} or more, while 25% of solar-type stars with a metallicity of [Fe/H] = 0.3 or higher have such a planet. They concluded that a power law in metallicity can describe the probability that a star hosts a close in giant planet, but did not investigate whether this holds for smaller planets or for long period orbits, due to lack of sufficient observational results. Previous indications that a planet-metallicity correlation extends to smaller planets (Schlaufman & Laughlin 2011) were shown to be due to contamination of their sample with giant stars (Mann et al. 2012). An analysis of 226 stars hosting small transiting planets from *Kepler* suggest that the probability of small planets forming is not sensitive to the bulk composition of the system (Buchhave et al. 2012a). However, an extended study utilizing *Kepler* data has suggested that terrestrial planet formation may be affected by the metallicity of the environment at formation, with slight differences between rocky planets, gaseous dwarf planets, and true ice giants (Buchhave et al. 2014a). Recent work by Wang & Fischer (2015) has suggested that there is a universal planet-metallicity correlation across all planet sizes and all metallicity values, but this result has been questioned by Buchhave & Latham (2015) who find that the stellar metallicity does not impact the radius distribution of the planets that form in a system. An additional study by Schlaufman (2015) found that a continuum of planet size between 1 $R_\oplus$ and 4 $R_\oplus$ can form, independent of the availability of solids in the bulk material. The relationship between stellar metallicity and planet occurrence is still an open question today.

While M dwarfs are currently our best prospects for detecting rocky, habitable planets whose atmospheres can be studied, in order to make the most of this opportunity we must turn our attention to the stars themselves. In particular, we must characterize the sample of nearby M dwarfs, estimate their masses, radii, and metallicities, and select the stars that are best suited for follow-up observations to hunt for planets. Unfortunately, prior to this thesis, much of this information was lacking, even though these M dwarfs represent the closest stars to the Sun. Through my thesis I have aimed to fill in the gaps in our understanding of these stars and prepare them to be prime hunting grounds for the next generation of planet hunting missions, and ultimately to aid in the search for life in the Universe.

1.2 The MEarth Project as Planet Hunter and Stellar Observer

My thesis has made extensive use of the MEarth dataset. The MEarth project (Nutzman & Charbonneau 2008) is designed to search the nearby mid-to-late M dwarfs for transiting planets. The MEarth project consists of two arrays of telescopes: 8 in the Northern hemisphere at the Fred Lawrence Whipple Observatory (FLWO) at Mt. Hopkins, AZ which has been operating since 2008, and 8 telescopes in the Southern hemisphere at Cerro Tololo International Observatory (CTIO) which have been operating since late 2014. Each telescope is 40 cm in diameter and is controlled robotically. Both installations use a Schott RG715 glass filter with anti-reflection coating. This filter and the MEarth magnitude system are described in detail in Chapter 3. This filter with its broad red sensitivity enables MEarth to maximize the number of photons received from the target M dwarfs. Both installations collect data every clear night, except the Northern Array closes in August each year for the summer monsoons.

The MEarth-North target list was selected from the sample presented by Lépine (2005), a subset of the LSPM-North catalog (Lépine & Shara 2005). Prior to this thesis, we believed that these stars were within 33 pc of the Sun and had a stellar radius of $R < 0.33R_{\odot}$ based upon their proper motion and color (Nutzman & Charbonneau 2008). The distances to the vast majority of these stars are estimated using their apparent magnitudes and colors. In many cases, the only optical magnitude that was available for these stars was one from a photographic plate, with estimated uncertainties of 20% or more (Lépine 2005). The Southern target list is an incomplete selection of M dwarfs following the same criteria as the Northern hemisphere target list pulled primarily from the RECONS sample.

MEarth's target stars are spread uniformly across the sky, and therefore typically only one target star exists in any one target field. Each MEarth telescope has a set of target stars that it observes each night for planets, iterating between each star before returning back to the first star on the list. Initially, we selected the exposure times for MEarth to allow us to collect enough photons such that we could detect a 2.0 $R_\oplus$ planet transiting in front of the star (Nutzman & Charbonneau 2008). However, after comparing with statistical results from *Kepler*, we altered this observing strategy (Berta et al. 2013). Now, each target M dwarf is observed with two telescopes in order to increase our signal to noise, increase the reliability of detections, and probe to smaller planets. This decreases the rate that MEarth can probe stars for planets but the steep rise in planet occurrence rate towards smaller planets around M dwarfs (Dressing & Charbonneau 2015) means that MEarth's expected yield increases with this observing strategy (Berta et al. 2013). Additionally, we have implemented a MEarth trigger observing mode (Berta et al. 2012a). If MEarth, during routine observations, detects a potential transit-in-progress, the telescope will continue to observe the target instead of moving on to the next M dwarf in its queue. It will continue to gather data on this target until it detects an egress. After detecting an egress, an out of transit baseline is reestablished, then the telescope resumes its normal observation schedule. This allows us to confirm longer period planets by confirming the transit in the discovery observations themselves. This trigger mode led directly to the detection of a 1.2 $R_\oplus$ transiting planet GJ 1132b (Berta-Thompson et al. 2015). The discovery trigger identified the planet and prompted us to obtain follow-up observations and confirm the planetary nature of the object.

Since beginning operations in 2008, MEarth has discovered a short period eclipsing binary (Irwin et al. 2009a), an M dwarf - brown dwarf eclipsing binary (Irwin et al. 2010), as well as a long period (41 day) M dwarf - M dwarf eclipsing binary (Irwin et al. 2011b). Constant monitoring of our target stars has also provided us with measured rotation periods (Irwin et al. 2011a; Newton et al. 2015b; West et al. 2015). These rotation periods span hours to over 100 days, with a paucity of intermediate rotators. Newton et al. (2015b) interprets this gap as an indication that M dwarfs spin rapidly for approximately 2 billion years, but that once they begin the process of spinning down this process is very rapid and the star quickly spins down to a rotation period of 100 days and longer.

At the time of writing, MEarth has discovered two exoplanets, one in the northern hemisphere and one in the southern hemisphere. The first planet discovered by MEarth, the super-Earth GJ 1214b (Charbonneau et al. 2009), has been the subject of an intense series of observations meant to measure its atmosphere from the optical (e.g. de Mooij et al. 2013; Bean et al. 2011; Murgas et al. 2012), to the infrared (e.g. Berta et al. 2012b; Bean et al. 2011; Crossfield et al. 2011; Croll et al. 2011; Désert et al. 2011; Fraine et al. 2013). The characterization of GJ 1214b was aided largely by the amount of information already known about the star prior to the discovery of GJ 1214b, including its trigonometric parallax. This parallax allowed a decent estimate of the true size of the star and hence the planet, but the relatively poor precision and uncertain accuracy of the literature parallax estimate for GJ 1214 was a limiting factor in our ability to characterize the planet. Significant effort has since been made to re-characterize this object, including deriving a revised parallax (Anglada-Escudé et al. 2013a) with modern data. Anglada-Escudé et al. (2013a) increased the measured distance to GJ 1214 from

13 parsec to 14.5 parsec, a 10% increase.

MEarth's second planet, GJ 1132b (Berta-Thompson et al. 2015), was much easier to characterize as we could measure the trigonometric parallax and determine a precise distance measurement to the system with MEarth-South discovery data itself. GJ 1132 is located closer to the Sun than GJ 1214, at only 12 parsec away ($\pi = 83.07 \pm 1.69$ mas Jao et al. 2005), and GJ 1132b is a 1.2 $R_\oplus$ radius planet with a density consistent with an Earth-like bulk composition. At the time of writing, no further characterization studies are available, although ground-based instruments at Magellan as well as the *Hubble* Space Telescopes have or are executing observing programs on this object. I am also currently conducting a 100 hour *Spitzer* Space Telescope program observing GJ 1132 slated to execute at the end of April 2016, and I will return to it at the end of this chapter.

Accurately estimating the stellar parameters of M dwarfs is vital towards our understanding of any transiting planet they may host. Any future planetary discoveries by the MEarth survey will likely be around a star less well-characterized than either GJ 1214 or GJ 1132, making the challenge of conducting detailed exoplanetary studies even more difficult. One way to better characterize these stars is to determine more accurate distances to them, since the distances to most of the MEarth targets were initially estimated using only photometric means with limited precision. I set out to see if the MEarth images could be calibrated astrometrically in order to measure trigonometric parallaxes.

1.3 Trigonometric Parallaxes: The Bottom Rung of the Distance Ladder

Trigonometric parallaxes are the gold standard in distance estimates. A parallax measurement requires measuring the position of a star on the sky at various times in the Earth's orbit. As the Earth changes position, the relative position of stars on the sky will change, as the stars lie at finite distances. While trigonometric parallax was a long-predicted consequence of the Copernican model, the first successful detection of a a stellar parallax took several centuries to achieve. The first trigonometric distance to a star was measured for 61 Cyg by Bessel (1838). After this initial success, parallax measurements became more routine, with hundreds of stars measured over the subsequent decades. However, it became clear that systematic effects between observers and observatories often resulted in wildly different determinations of the distance to the same star. A compilation by Bigourdan (1909) of trigonometric parallaxes known at that time lists 23 individual measurements of the parallax for 61 Cyg (including that of Bessel 1838), ranging from 177 milliarcseconds to 559 milliarcseconds. The modern value (from the *HIPPARCOS* mission) is 286 milliarcseconds (Perryman et al. 1997).

In 1903, the new technology of photographic plates began to be used in astronomy, and Frank Schlesinger began working with the technology at the Yerkes 40-inch refractor in order to attempt to reduce these errors (Schlesinger 1904). The effect of refraction was limited by designing a plate insensitive to blue light, and use the properties of the refractor to spread the blue light over as wide an area as possible, so that it would not be detectable. The technology and techniques that Schlesinger pioneered were adopted among many observatories, and new measurements of trigonometric parallaxes to nearby stars were regularly released. A compilation of 5822 parallax measurements culminated in the first Yale Parallax Catalog in 1952 (Jenkins 1952), which has since seen numerous new editions and updates (van Altena 1984; van Altena & Lee 1988; van Altena & Hoffleit 1996a).

In the modern age, the *HIPPARCOS* satellite revolutionized astrometry. *HIPPARCOS* was a 3.5 year space-based mission that measured the distance to over 100,000 stars with unprecedented precision (Perryman et al. 1997). In addition to astrometric distance measurements, *HIPPARCOS* also provided a direct measurement of the stellar magnitude of its targets (van Leeuwen et al. 1997). The sheer quantity of stars observed enabled directly measuring the color-magnitude diagram for stars of known ages in clusters (Pinsonneault et al. 1998), as well as measurements of local Galactic kinematics (Smart et al. 1998; Reid 1998; Helmi et al. 1999). At the end of its mission, 99% of all stars with a visual magnitude of 11 or brighter were observed by *HIPPARCOS*, and diminishing quantities of more faint stars. Unfortunately, it is this visual magnitude cut-off that prevented the distances to the most numerous type of star - the M dwarfs - from being measured. Effort to plug this gap has been slow, since there is no dedicated facility to conduct this work, although numerous efforts are underway. As these objects are cool and dim in the optical, parallax programs using infrared instruments have proved successful (Dupuy & Liu 2012; Vrba et al. 2004). Additionally, the REsearch Consortium On Nearby Stars (RECONS) survey, a long standing parallax program at CTIO, has provided a wealth of parallaxes for nearby white dwarfs, brown dwarfs, and late M dwarfs, currently with 30 papers (Winters et al. 2015; Hosey et al. 2015) identifying and characterizing new stars in the solar neighborhood, many of which lie within 10 parsecs (see Riedel et al. 2011 and references therein).

In Chapter 2, I present the results of our analysis of 5 years of MEarth-North images. Since MEarth had been monitoring these stars for transiting planets, we had been taking observations at various phases of Earth's orbit. Therefore, we thought that it might be possible to use the MEarth planet-hunting data as a way to measure the distances to our stars and better characterize them. I found that MEarth was capable of producing precise astrometric measurements, and we began observing every star in our target list at a 10 day cadence, whether or not we were hunting for planets around that star. After these additional observations, we published trigonometric parallaxes, and mass and radius estimates for 1507 M dwarfs with a typical precision of 5 mas. We found that many of these stars were further away (and therefore brighter) than we initially believed based on their colors. This means that they are either multiple star systems or actually more massive than we initially believed them to be. In either case, the stars become less attractive targets for planet searches, as a stellar companion might dynamically affect a planet (and at the very least dilute the transit depth), and a more massive star makes the signal from a planet in that system smaller. I find that the northern hemisphere census of M dwarfs is mostly complete to a distance of 25 parsecs for stars of spectral type M5.5V and earlier, and mostly complete for stars earlier than M7.0V to a distance of 20 parsecs. I confirm via trigonometric distances 8 stars that did not previously have a measured parallax that lie within 10 parsecs of the Sun.

At the time of this publication, MEarth had only been observing the vast majority of target stars at astrometric cadence for 2 years. With only 2 years of data, it is only possible to separate out the effects of proper motion (linear motion in the plane of the sky) and trigonometric parallax (apparent motion due to the Earth's orbit). Additional astrometric signals (since as those due to orbital motion of the star about a close companion) are not resolvable on these time scales. Therefore, we did not investigate them in this chapter. However, since the publication of this chapter, MEarth has collected several years of additional astrometric data and it will now be possible to look for astrometric companions to our stars.

Since this publication, the *Gaia* satellite (Lindegren & Perryman 1998) has launched and began taking data. *GAIA*'s mission is to pick up where *HIPPARCOS* left off. It will measure the trigonometric distance to every object in the sky that is brighter than a V magnitude of 20. For these objects, *Gaia* will have an astrometric precision of approximately 20 microarcseconds. This includes every target on the MEarth target list. However, if any of these stars are actually long period multiples, then *Gaia*'s data will be incomplete, because it has a finite baseline. In the future, the MEarth data set (though of lower astrometric precision) can possibly be stitched onto the GAIA data, extending the time baseline and can be used to measure the dynamical mass of astrometric multiples.

1.4 The Brightness and Metal Content of our Sun's Nearest Neighbors

After measuring the distances to each of the MEarth target stars, I sought to utilize MEarth as a legacy dataset to measure more accurate optical magnitudes for the nearby M dwarfs. MEarth is an optical instrument operating with a Schott RG715 glass filter. The effective wavelength of a typical M-dwarf target, accounting for telluric absorption, the filter bandpass, and the detector quantum efficiency is 850 nm. Being in the red-optical regime, a MEarth magnitude could be used to replace the photographic plate magnitudes. During each night of observation, the MEarth telescopes take observations of Landolt standard fields (Landolt 1992). These standards are stars with precisely measured magnitudes, and are meant to be used to calibrate data, since it is easier to measure relative brightnesses of stars rather than to directly measure the energy being received by one particular star.

One problem with calibrating photometric data for M dwarfs is that there are very few red standard stars, and the effect of the atmosphere is color dependent. Because blue light scatters more efficiently in the atmosphere than red light, when comparing our red target M dwarfs brightnesses to a bluer standard star, the atmosphere will have a profound effect. We found that atmospheric parameters that depend linearly on the airmass of the observation and the color of the target star were sufficient to describe this effect and that the MEarth instrument was capable of measuring the apparent magnitude of an object with 1.5% precision.

In Chapter 3 (Dittmann et al. 2016) I present this analysis and also combine these measurements with the results from Chapter 2 in order to measure the distance corrected brightnesses of our target stars at optical wavelengths. When I combine these results with spectroscopic metallicity measurements performed by Newton et al. (2014) and Newton et al. (2015a), I find that an optical - infrared color that includes the MEarth magnitude as the optical magnitude is sensitive to the metallicity of the star. I succeeded in calibrating a relationship between an M dwarf's absolute (distance corrected) K_s band magnitude, its $MEarth - K_s$ color, and its metallicity, with a precision of 0.1 dex in metallicity. This precision is comparable (and possible limited by) the precisions obtained using infrared spectroscopic techniques. However, obtaining a near-infrared spectrum is a time consuming and resource intensive task, and so being able to obtain a metallicity measurement from broadband photometric measurements alone is much more efficient. We released metallicity estimates for every MEarth target that had a measured parallax. Importantly, all of these metallicity measurements were measured uniformly across the sample, which reduces one source of systematic errors.

We found that median metallicity for the solar neighborhood M dwarfs is [Fe/H] = -0.030 ± 0.008, indistinguishable from solar neighborhood G dwarfs. Additionally, we find that 29 / 565 M dwarfs in a 20 parsec volume have a metallicity of [Fe/H] = -0.5 or lower, which is similar to Haywood (2001), who measured that 4% of their 383 solar neighborhood G dwarfs have a metallicity less than [Fe/H] = -0.5.

In the future, MEarth and other future planet hunting surveys will begin to uncover the population of planets around these stars. Armed with these metallicity measurements, it will be possible to settle the question of whether a planet-metallicity correlation exists.

1.5 Fundamental Parameters: Masses and Radii

While hunting for planets, MEarth is also extremely sensitive to eclipsing binary systems, as their eclipses are much deeper than planetary transits. Once the MEarth-South instrument was commissioned, we uncovered the existence of an eclipsing binary system, LP 661-13 on the second night of observations. In Chapter 4 of this thesis, I present the MEarth observations for this system as well as high resolution spectroscopic radial velocity measurements from TRES. LP 661-13 has a 4.7 day orbital period, long enough that tidal effects between the two stars are largely diminished. This makes LP 661-13 an ideal target for detailed study and characterization. We obtained observations of 22 primary and secondary eclipses of this system with MEarth-South, and we obtained 14 epochs of high resolution spectroscopic follow up in order to constrain the masses of these stars. Additionally, a periodic signal is apparent in the MEarth data due to rotational modulation and the presence of starspots on the star. Importantly, over two years of observations the signal changes. This allowed us to measure the potential effect starspots have on determining the fundamental physical parameters of this star system.

LP 661-13 has component masses of 0.3050 ± 0.0056 and 0.1937 ± 0.0027 $M_{\odot}$ and component radii of 0.3192 ± 0.0037 and 0.2159 ± 0.0061 $R_{\odot}$, which places both components at the low mass end of the stellar sequence. This makes LP 661-13 a valuable system, as there are few stars low mass stars who have their physical parameters measured precisely and it is in this mass regime that the stellar models are least able to reproduce observations (Torres 2013). While we find each component is marginally consistent with stellar models, the sum of the radii (a better constrained parameter) is inflated with respect to stellar models. Obtaining such high precision on the masses and radii of M dwarfs is a rare occurrence and LP 661-13 joins a small (but growing) list of stars with such measurements.

In the future, it would be a great benefit to get eclipse observations of LP 661-13 in bandpasses significantly different than the MEarth bandpass. Having these measurement in other colors would allow us to measure the light ratio between the two stars across their spectra, allowing us to place direct constraints on each star's temperature. Of particular interest is the K_s band, since this is the band that is most directly sensitive to stellar mass (Delfosse et al. 2000).

1.6 The Nearby M dwarfs as a Benchmark Stellar Sample

Throughout this thesis, I present the trigonometric distances to many of the nearby M dwarfs, measures of their optical magnitudes, and a luminosity-color-metallicity relation that combines these results together. However, it should be noted that the *MEarth* bandpass is not a standard bandpass. It would be beneficial to have a way to measure the metallicity of an M dwarf using more commonly used filters. Furthermore, the results I present in Chapter 3 require a distance measurement to the M dwarf. While this works for the nearby M dwarfs, many other M dwarfs do not have trigonometric parallaxes and will be too dim even for *Gaia* to measure. At *Gaia*'s limiting magnitude of $G = 20$, *Gaia* will only detect M5V stars at a distance of 500 parsecs, and the distance to these stars will be measured with 10% accuracy.

The Large Synoptic Survey Telescope (LSST) (Gressler et al. 2014) is set to survey the entire Southern sky every few nights in the *griz* filter system. While the main goal of the survey is independent of low-mass stellar science, a secondary goal is that the LSST will discover millions of M dwarfs in the Milky Way, and measure their optical magnitudes. A complementary survey, VISTA is currently surveying the Southern sky in the near infrared JHK_s bands (McMahon 2012). With these two data sets, M dwarfs are poised to become a useful stellar tool to trace the structure of the Galaxy.

However, in order to realize this promise, we need a method to be able to accurately measure the metallicities of these stars without a distance. Realizing this, and building on the experience and results from Chapter 3, I set out to obtain calibrated *griz* photometry of a subset of the MEarth target stars that had a spectroscopic metallicity measurement from Newton et al. (2015a). What we found was surprising: subtle differences between the *griz* filters that define the $g'r'i'z'$ system, the *griz* filters on the Sloan Digital Sky Survey (SDSS) telescope, and *griz* filter set available at FLWO make measurements in the r band incompatible. The ζ parameter, a metallicity-sensitive measure of the relative strength of TiO and CaH, CaH_2, and CaH_3 spectral features in an M dwarf spectrum (Lépine et al. 2007) lies at the red edge of the r filter. We discovered that slight changes in the filter can shift these features into and out of the bandpass and affect the final metallicity determination.

Despite this, we were able to calibrate the FLWO *griz* photometric system onto the USNO observations that define the *griz* photometric system. Of the 158 stars in the Smith et al. (2002) standard star network, only 12 have a $g' - i'$ color greater than 2, and only 5 of those have a $g' - i'$ color greater than 2.5. In contrast, only 3 of 150 of our target M dwarfs have a $g - i$ color less than 2.5. We found that the $g - i$ and $i - K_s$ colors of an M dwarf can be used to estimate an M dwarf's metallicity with 0.1 dex precision. We further found that there is no accurate metallicity relation that can be discerned from Sloan optical magnitudes alone: an infrared magnitude is needed in order to disentangle the effects of stellar mass and stellar metallicity on color.

In the future LSST and VISTA will complete their surveys, and in the process study millions of M dwarfs in the Galaxy that have never been examined before. Few of these objects will have a trigonometric distance measurement any time soon, and only a handful (if any) will have an infrared spectrum from which a metallicity can be deduced. A metallicity to each may be estimated, however, with the results in this chapter. With those metallicity estimates, M dwarfs can be used as tools to map the metallicity distribution in the Galaxy and potentially uncover new trends and information in how the Milky Way was assembled. At the heart of those measurements will lie the nearby solar neighborhood M dwarfs.

1.7 Upcoming Work and Opportunities

When I started this thesis, we did not have accurate distance measurements to the majority of the M dwarfs within 25 parsecs of the Sun. Now, 6 years later, we have measured the distances to 1507 M dwarfs directly. We did not have a photometric metallicity relationship for these stars. The MEarth M dwarfs have an optical magnitude measured with 1.5% precision, to replace measurements that could have error bars in excess of 20%. We have photometrically measured the metallicity distribution of the nearby M dwarfs by grounding our measurements with spectroscopic determinations, and have expanded this technique to the Sloan photometric system. It is my hope that our color-color-metallicity relation is of use to the teams working on LSST and VISTA and that M dwarfs become useful tools for studies of Galactic structure.

From an exoplanetary standpoint, MEarth has continued hunting for the closest rocky planets that will be the most amenable to study with future instrumentation. The discovery of GJ 1132b (Berta-Thompson et al. 2015) occurred during the course of this thesis. The characterization of this system is just beginning, and I am currently leading a follow-up effort with the *Spitzer* space telescope to characterize GJ 1132b and attempt to discover additional planets in the system. At 12pc, GJ1132b is the closest M dwarf known to host a transiting rocky planet. Coplanar multiplanet systems are common around M dwarfs (Ballard & Johnson 2016; Muirhead et al. 2015), so it is possible GJ

1132 hosts additional rocky planets that have not yet been detected. In Figure 1.1, I show the photometric sensitivity of *Spitzer* to additional transiting planets, along with other known transiting planet systems around M dwarf primary stars. There remains a vast discovery space where additional planets may exist in the GJ 1132 system, and the 100 hour *Spitzer* program that I am leading has the potential to discovery them, should they exist and show transits. This program will also collect precise observations of transits of GJ 1132b as well. The sensitivity of Spitzer will also allow us to potentially detect exomoons orbiting GJ 1132b down to the size of the Galilean satellites.

Throughout my thesis I have also endeavored to hunt for additional planets in the MEarth data and to push the data to its limits. I have been particularly interested in the MEarth Trigger data (Berta et al. 2012a), and have utilized machine learning techniques (Haykin 1998) to compare MEarth triggers to each other in an effort to find outliers. These outliers, in turn, could prove to be interesting astrophysical phenomena or (hopefully) long period exoplanets that have evaded detection through phase folding techniques due to their long orbital periods. Using this technique, I selected one event and one star (LHS 1140) to send for detailed RV monitoring with the HARPS instrument. I show this trigger in Figure 1.2.

1.7.1 Future Planet Surveys

New RV and transit surveys slated to focus on the mid-to-late M dwarfs are beginning to come online. These include the near infrared radial velocity surveys CARMENES (Quirrenbach et al. 2012), the Habitable Planet Finder Spectrograph (Mahadevan et al. 2012), and SPIROU (Reshetov et al. 2012), and the currently operating photometric

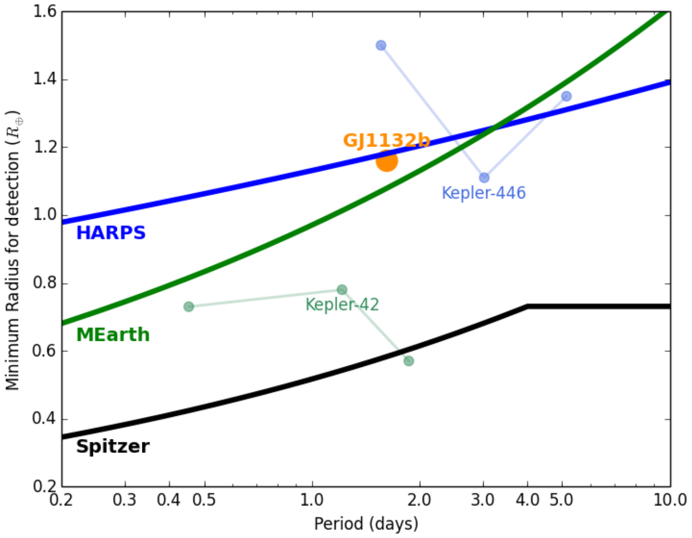

Figure 1.1: *Spitzer*'s sensitivity (black lower line) to additional transiting objects in the GJ 1132 system, compared to their detectability using ground based photometric (MEarth, green middle line) and RV (HARPS, blue upper line) measurements. The location of GJ 1132b is marked as the solid orange point, and the *Kepler* compact M dwarf systems Kepler-446b,c,d and Kepler-42b,c,d as the blue and green data points, respectively. The MEarth sensitivity curve assumes an intensive monitoring campaign by MEarth until the launch of JWST, while the HARPS sensitivity curve is based upon blind recovery assuming an ambitious 130 data point program. *Spitzer*'s 4-day monitoring sensitivity far surpasses extensive campaigns by both MEarth and HARPS. The kink in the Spitzer sensitivity is due to the rapid loss of sensitivity for planets at periods greater than the duration of the observations scheduled to be executed. *Spitzer* is capable of finding planets the size of Mars (0.53 $R_\oplus$) out to periods of 1 day, while even the most ambitious and high-quality ground based measurements struggle to find planets the size of the Earth.

transit survey APACHE (Sozzetti et al. 2013). Additionally SPECULOOS (Gillon et al. 2013) and ExTrA (PI: X. Bonfils) are planning to survey nearby mid-to-late M dwarfs in the Southern hemisphere for transiting planets. In space, the NASA *TESS* mission is currently being built and is planned to launch in 2017 (Ricker et al. 2015). *TESS* will be an all-sky, brightness limited survey that will begin by observing the entire Southern sky in sequential 30 day pointings and then repeat these observations in the Northern hemisphere.

The nearby M dwarfs that I have characterized in this thesis will be the most profitable targets for these planet surveys and the planets that these surveys find will be the planets that the *James Webb Space Telescope* (JWST) devotes substantial observing time to. The only rocky planet that has an atmospheric signal accessible to JWST will be one that orbits one of these stars. It is my hope that the distances, masses, radii, and metallicities that I present here prove useful in selecting the best targets for finding planets and that one day we will find a habitable, rocky exoplanet transiting in front of one of these stars.

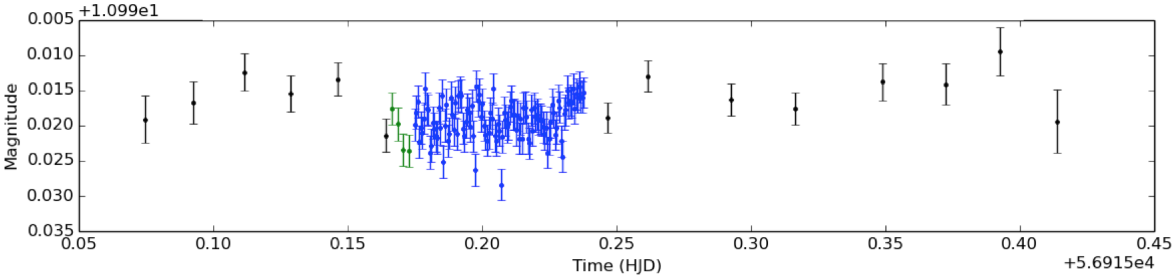

Figure 1.2: MEarth-South trigger for LHS 1140b flagged for potential followup. Here, MEarth-South measured one low data point, and began confirmation follow-up (green data points). When those confirmation data points were also low, high cadence follow-up (blue data points) began until the egress, at which point MEarth-South resumed normal operations. We deemed this trigger high quality enough to begin RV monitoring.

Chapter 2

Trigonometric Parallaxes for 1507 Nearby Mid-to-late M dwarfs

This thesis chapter originally appeared in the literature as

J. A. Dittmann, J. M. Irwin, D. Charbonneau, Z. K. Berta-Thompson *The Astrophysical Journal*, 784, 156, 2014

Abstract

The MEarth survey is a search for small rocky planets around the smallest, nearest stars to the Sun as identified by high proper motion with red colors. We augmented our planetary search time series with lower cadence astrometric imaging and obtained two million images of approximately 1800 stars suspected to be mid-to-late M dwarfs. We fit an astrometric model to MEarth's images for 1507 stars and obtained trigonometric distance measurements to each star with an average precision of 5 milliarcseconds. Our

measurements, combined with the Two Micron All Sky Survey photometry, allowed us to obtain an absolute K_s magnitude for each star. In turn, this allows us to better estimate the stellar parameters than those obtained with photometric estimates alone and to better prioritize the targets chosen to monitor at high cadence for planetary transits. The MEarth sample is mostly complete out to a distance of 25 parsecs for stars of type M5.5V and earlier, and mostly complete for later type stars out to 20 parsecs. We find eight stars that are within 10 parsecs of the Sun for which there did not exist a published trigonometric parallax distance estimate. We release with this work a catalog of the trigonometric parallax measurements for 1507 mid-to-late M-dwarfs, as well as new estimates of their masses and radii.

2.1 Introduction

One of the goals of stellar research is to obtain the complete census of stars within the solar neighborhood out to a specified distance. A complete volume-limited sample will inform us about the stellar mass function, stellar formation, and the kinematics of the Galaxy as well as the nearby stellar clusters for which we can identify members. Low mass stars vastly outnumber higher mass stars like the Sun, and so the main difficulty in constructing a volume limited sample is in identifying nearby, low mass, low luminosity objects and obtaining accurate distances to them. Apparent magnitude is a poor indicator of proximity; only a couple dozen of the several thousand stars visible by the naked eye are within 10 parsecs of the Sun (Upgren 1996). Currently, the most straightforward method to identify potentially nearby stars is from proper motion surveys, as a star with a high angular velocity is more likely to be nearby to the Sun.

Proper motion surveys have been conducted for many decades, as the measurements are relatively simple to make, requiring only images of the same field separated by a length of time. Proper motion surveys continually improve, as longer time base lines increase the accuracy of the measurements. A uniform census of nearby stars allows for characterizing the relative occurrence rates of different types of stars, and to plot the relationship between intrinsic properties of those stars, including absolute magnitude and color.

Early attempts at conducting a large survey for high proper motion stars began in the early 20th century with work by van Maanen (1915), who compiled a list of stars known at that time whose proper motion exceeded 0.50 arcsec yr^{-1}. This list was subsequently expanded by Wolf (1919) and Ross (1939), pushing the limit to 0.20 arcsec yr^{-1}. As these surveys progressed, it became apparent that there existed a large population of high proper motion, low luminosity objects that were previously undetected due to their faintness. Due to the relatively large numbers of these objects, obtaining a volume-limited sample of high proper motion stars required deep exposures of the entire sky, combined with long time baselines. Such a survey was completed over several years by various groups, most notably from Lowell Observatory (Giclas et al. 1971, 1978), which consists of 11,749 stars, and the New Luyten Catalogue of Stars with Proper Motions Larger than Two Tenths of an Arcsecond (the NLTT catalog; Luyten 1979), which contains 58,845 objects. More recently, Lépine & Shara (2005) compiled a list of 61,977 stars in the northern hemisphere with proper motions larger than 0.15 arcsec yr^{-1}, identifying over 90% of those stars down to a limiting magnitude of $V \approx 19.0$, excepting the Galactic plane. A subset of this catalog identified in Lépine (2005) identifies those stars that are likely within 33 pc of the Sun, in order to provide the basis for a volume-limited sample for further study and characterization, including spectral typing and obtaining direct distance estimates to these stars.

Of the several different methods that can be used to obtain distances to stars, trigonometric parallax is the most accurate. Photometric and spectroscopic parallax methods, in contrast, assume that the star is single and that the main sequence is single valued with luminosity as a function of effective temperature. When estimating the distances to stars through these methods, one might introduce systematic errors depending on the quality of the data and the models that are assumed.

The first detection of a stellar parallax was for 61 Cyg by Bessel (1838). A catalog of 248 stars with parallaxes determined from plates taken by Prof. Donner at Helsingsfors from 1891-1892 was released by Kapteyn (1900). Such long delays in parallax studies became common, as systematic effects between observers and observatories often resulted in widely different claimed values for the parallax of individual stars. A compilation by Bigourdan (1909) of trigonometric parallaxes known at that time lists 23 individual measurements of the parallax for 61 Cyg, ranging from 177 mas to 559 mas. The currently accepted value is 285.4 milliarcseconds with an uncertainty of 0.8 milliarcseconds (Perryman et al. 1997).

Great effort was made to reduce the systematic error in parallax work by Schlesinger, beginning in 1903 with the Yerkes 40 inch refractor (Schlesinger 1904). He utilized newly designed green-sensitive plates that were insensitive to the out-of-focus blue light from the refractor, in order to avoid systematic errors in the derived positions (Schlesinger 1910a,b). These efforts began yielding fruit (see Schlesinger (1910c, 1911), and companion papers), ultimately producing a catalog of 1870 parallaxes (Schlesinger

1924). These techniques were widely adopted among many observatories, with new measurements being published in batches of dozens to hundreds. The total number of stars with parallaxes grew to 5822 with the compilation of the first Yale Parallax Catalog (Jenkins 1952).

Astrometry programs have since conducted larger surveys for dimmer objects. Today, the two major databases of stellar parallaxes come from the General Catalog of Trigonometric Stellar Parallaxes, Fourth Edition (the Yale Parallax Catalog, van Altena & Hoffleit 1996b) and the *Hipparcos* mission (Perryman et al. 1997; van Leeuwen 2007a,b), which combined have distance determinations to approximately $120,000$ stars. Precisions in the Yale Parallax catalog range from a few mas to 20 mas, while the *Hipparcos* catalog routinely obtains precisions of several tenths of milliarcseconds for stars brighter than $V = 8$. This brightness cutoff of parallax programs means that low mass objects such as most M dwarfs and brown dwarfs are systematically underrepresented in these surveys and almost completely absent from the *Hipparcos* sample.

Numerous trigonometric parallax programs are currently underway to identify and determine distances to the nearby missing objects, consisting mainly of low mass stars and brown dwarfs. As these objects are cool and dim in the optical, parallax programs using infrared instruments have proved successful (Dupuy & Liu 2012; Vrba et al. 2004). Additionally, the Research Consortium on Nearby Stars (RECONS) survey[1], a long standing parallax program at CTIO, has provided a wealth of parallaxes from nearby white dwarfs, brown dwarfs, and late M dwarfs, currently with 30 papers identifying

---

[1] RECONS (http://www.chara.gsu.edu/RECONS/) has graciously made their results easily accessible, and we have used their recent parallax work extensively when comparing to our own.

and characterizing new stars in the solar neighborhood, many of which lie within 10 parsecs (see Riedel et al. 2011 and references therein). RECONS has utilized astrometric, photometric, and spectroscopic observing techniques in order to discover and characterize these systems. Limited compilations of large numbers of measurements of these objects are also given by Lépine & Gaidos (2011), whose aim is to provide a candidate list of nearby M-dwarfs with high proper motion for further studies by other groups. Understanding these stars and their companions requires reliable distance estimates, in order to estimate their intrinsic luminosities, radii, and other physical parameters.

The small sizes of M dwarfs make them excellent targets for ground-based searches for transiting small planets. This contributed to a renewed interest in these objects, and obtaining a volume-limited sample, and accurate distances, are important scientific goals. MEarth is an ongoing photometric survey of nearby ($D \lesssim 33$ pc) mid-to-late M dwarfs, designed to be sensitive to planets around these stars as small as $2R_{\oplus}$ and with periods extending into the habitable zone (Nutzman & Charbonneau 2008). The advantages of conducting a transiting planet search around these stars include being sensitive to rock and ice planets from the ground, the shorter period of a habitable-zone planet, and the accessibility of the atmospheres of these planets with current or next-generation instrumentation (e.g., *James Webb Space Telescope* and the next generation of large ground-based telescopes). The first planet discovered by MEarth, the super-Earth GJ 1214b (Charbonneau et al. 2009), has been the subject of an intense series of observations meant to measure its atmosphere from the optical (e.g. de Mooij et al. 2013; Bean et al. 2011; Murgas et al. 2012), to the infrared (e.g. Berta et al. 2012b; Bean et al. 2011; Crossfield et al. 2011; Croll et al. 2011; Désert et al. 2011; Fraine et al. 2013).

The characterization of GJ 1214b was aided largely by the amount of information already known about the star prior to the discovery of GJ 1214b, including its trigonometric parallax. This parallax allowed a decent estimate of the true size of the star and hence the planet. The relatively poor precision and uncertain accuracy of the literature parallax estimate for GJ 1214 was a limiting factor in our ability to characterize the planet. Significant effort has been made to re-characterize this object, including deriving a different parallax (Anglada-Escudé et al. 2013a) with modern data. For example, if GJ 1214 were located at 15 pc away instead of 13 pc, this would increase the intrinsic luminosity of the star by 0.3 magnitudes, and increase the inferred radius of the star by 10%. Clearly, accurately estimating the stellar parameters of M dwarfs is vital towards our understanding of any transiting planet they may host. Any subsequent planetary discoveries by the MEarth survey will likely be around a star less well-characterized than GJ 1214, making the challenge of conducting detailed exoplanetary studies even more difficult.

As MEarth has taken a large number of images of its target stars over the course of entire observing seasons, we investigated whether the MEarth images themselves could be used to measure the trigonometric parallax distances to our targets. We found that the MEarth images are well-suited for astrometric analysis and modified our survey to provide astrometric measurements of all of our stars every 10 days. This paper presents the results of that effort. In section 2.2, we present a description of our instruments and our observing strategy. In section 2.3, we describe our astrometric model, and validate our method with the subset of our sample that have previously measured trigonometric distances. Finally, in section 2.4 we compare our results to photometric distance estimates, we refine the estimates of the mass and radius of the stars in our survey, and we identify additional stars within 10 parsecs to the Sun.

A few years from now several additional surveys for planets orbiting M dwarfs will be operational in the northern hemisphere: These include the planned near infrared radial velocity surveys CARMENES (Quirrenbach et al. 2012), the Habitable Planet Finder Spectrograph (Mahadevan et al. 2012), and SPIROU (Reshetov et al. 2012), and the currently operating photometric transit survey APACHE (Sozzetti et al. 2013). We hope that the results presented in this paper will be of direct benefit to these projects. At least three additional M-dwarf transit surveys are planned for the southern hemisphere: SPECULOOS (Gillon et al. 2013), ExTrA (PI: X. Bonfils), and MEarth-South, a copy of the MEarth-North observatory located at the Cerro Tololo Interamerican Observatory in Chile. We may use MEarth-South to undertake a similar effort to provide trigonometric parallaxes for southern targets.

2.2 Observations

The MEarth Observatory is an array consisting of eight identical f/9 40 cm Ritchey-Chrétien telescopes on German equatorial mounts at the Fred Lawrence Whipple Observatory on Mount Hopkins, Arizona. The telescopes are controlled robotically and collect data every clear night from September through July. The facility is closed every August for the summer monsoons. Each telescope contains a 2048 x 2048 pixel CCD with a pixel scale of ≈ 0.76" pixel^{-1} and a Schott RG715 glass filter with anti-reflection coating. The cutoff is defined by the CCD response, and the effective bandpass is similar to the union of the SDSS i and z filters.

Initially we cooled the detectors to -15°C and did not use a pre-flash. From 2011 onwards, the MEarth cameras operated at $-30°$ C, and before each exposure we adopted a pre-flash of the detector. This increases the dark current (which we subsequently subtract off), but has the benefit of suppressing persistence from the previous exposure. (If the persistent image contained a source that overlaps with the target or reference stars, this could skew our astrometric measurements.) There is no discernible effect of any residual persistence on the MEarth photometry, and we do not believe it to be relevant astrometrically. Prior to 2011, we carefully ordered the observing sequence of our target fields to avoid source overlap when switching between them.

We gathered flat-field frames each observing night at dawn and dusk. The MEarth telescopes use German equatorial mounts, which require the telescope tube to be rotated by 180 degrees relative to the sky upon crossing the meridian. We take advantage of this for flat fielding by obtaining adjacent pairs of flat field images on opposite sides of the meridian to average out large-scale illumination gradients from the Sun and the Moon. Our flat-field correction is further complicated by scattered light concentrating in the center of the field-of-view, where our target is located (the amplitude of this effect is approximately 5% of the average value across the CCD). Consequently, we filter out all large scale structure from the combined twilight flat field, and use it only to track changes in small scale (high spatial frequency) features such as interpixel sensitivity and dust shadows. The large scale flat field response was derived from dithered photometry of dense star fields. We also correct for varying exposure time across the field of view due to shutter travel time, as well as fringing. We have found these corrections to be stable, and we update them annually.

We measured stellar positions through a method similar to Irwin (1985): Local sky background is estimated by binning each image into 64 pixel × 64 pixel blocks, and then we estimate the peak of the histogram of the intensity of the pixels within each area. We then interpolate to estimate the background level anywhere in the image from this lower resolution background map (Irwin 1985). We measure the stellar location using intensity weighted first moments (also called a centroid), computed over a circular aperture (radius 5 pixels prior to 2010 August, and 4 pixels thereafter due to a change in our focus strategy). Pixels partially inside the aperture are weighted according to the fraction of the pixel area inside the aperture. The initial aperture locations are estimated from the expected target location, based on a master MEarth image taken during good weather conditions, and accounting for proper motion. The solution is then iterated using the measured pixel coordinates to update the location of the aperture. For more details of the MEarth photometric data products and processing pipeline, see Berta et al. (2012a).

The MEarth target list consists of ≈ 1800 nearby M dwarfs selected from Lépine (2005), a subset of the LSPM-North catalog (Lépine & Shara 2005) believed to be within 33 pc of the Sun (Nutzman & Charbonneau 2008). These targets are uniformly distributed across the Northern sky ($\delta > 0°$), such that typically only one target exists in the MEarth 26' x 26' field of view, with the exception of multiple systems and occasional unrelated asterisms. Therefore, each field must be observed in a pointed manner, distinguishing MEarth from other photometric transit surveys. Each field of view is, by design, large enough to contain sufficient comparison stars to obtain high precision relative photometry and astrometry. Due to the nature of our targets, the comparison stars are, on average, much bluer (typical $r - J = 1.3$) than the M dwarf target (typical $r - J = 3.8$).

During the summer monsoon, which occurs each year in August, data acquisition was halted and the telescopes were shut down. This time has been used to perform maintenance activities, and also major upgrades in 2010 and 2011, which may result in significant disturbances to the data, such as changing how the instrument flexes when pointing in different directions. We will describe our procedure for combining pre-2011 and post-2011 data in section 2.3. Additional hardware failures have occasionally necessitated removal of the detectors from the telescopes during the observing season, which resulted in rotational offsets (the mechanism for this alignment is repeatable to approximately $0^\circ.5$). These changes are likely to result in further disturbances to photometry and astrometry. We describe how we correct for this later. Table 2.1 lists the dates where the detectors were removed for each telescope.

Table 2.1:: Dates cameras were removed from the MEarth telescopes

Telescope	UT Date
1	2009 Nov 16
1	2010 Oct 29
1	2011 Oct 12
1	2012 Jan 02
1	2012 Feb 01
2	2009 Nov 20
2	2010 Oct 29
2	2011 Oct 12
2	2011 Dec 24
2	2012 Sep 04
3	2009 Nov 16
3	2010 Oct 29
3	2011 Oct 12
3	2012 Feb 07
3	2012 Jun 22
3	2012 Sep 09
3	2012 Dec 28
4	2010 Oct 29
4	2011 Oct 12
4	2012 Apr 26
4	2012 Aug 02
5	2009 Nov 16
5	2010 Feb 09

Table 2.1 (Continued):

5	2010 May 26
5	2010 Oct 29
5	2011 Oct 12
5	2012 Jan 08
6	2010 Oct 29
6	2011 Oct 12
6	2012 Jan 09
7	2009 Nov 16
7	2010 Oct 29
7	2011 Oct 12
7	2012 Apr 18
7	2012 Oct 25
7	2013 Mar 09
8	2010 Oct 29
8	2011 Oct 12
8	2012 Jan 02

From each observing season (September through July), the MEarth project gathered data at a roughly $20 - 30$ minute cadence for the subset of the targets for which we were actively searching for planets at that time. Beginning in October 2011, we began collecting additional data at a roughly 10 day cadence for all other targets for the purposes of astrometric measurement. In each pointing, we gathered enough exposures such that we have collected sufficient photons to detect a 2 $\mathrm{R}_\oplus$planet passing in front of the target star. As a result, different stars will have a different number of exposures per pointing. For the purposes of the astrometry presented here, each individual exposure is treated as a separate data point. The data presented here covers the time period from 2008 September through 2013 July.

2.3 Analysis

2.3.1 Astrometric Model

We selected images for inclusion in the astrometry fitting if they met the following criteria: The FWHM for the image is less than 5 pixels (3.5 arcsec), the average ellipticity of the target stars is less than 0.5, the target star is not more than 15 pixels away from its assigned location on the CCD, and the airmass at which the image was taken is not greater than 2.0. These selection criteria typically eliminate 50% of the MEarth images for each target, but can sometimes eliminate up to 80% of images. Most eliminated frames are eliminated due to a large FWHM, either due to naturally poor seeing or wind-shake of the telescope. For each target star, we selected a master image through an automated routine that selects an image that is of good image quality (low FWHM, ellipticity, sky noise), and good photometric quality (brightness of the stars is not significantly different from a typical exposure). The sky-coordinate system for this image is determined through star matching with the Two Micron All Sky Survey (2MASS) catalog. When many images meet the criteria to be a suitable "master" image, we select one image manually. We investigated the effect of our master frame choice on our final astrometric parameters and find that the choice of master frame does not significantly affect our astrometric measurements.

Reference stars are selected to be between magnitude 8 and magnitude 13 in the MEarth passband, are not blends or close binaries, and are unambiguously identified in the 2MASS catalog. Additionally, in order to avoid effects due to higher order plate corrections, we attempt to avoid using stars near the edges of the CCD. This is done by initially selecting only stars within 600 pixels of the target star (or in the few cases where there are multiple target stars, the average position of the target stars). If the total number of reference stars within 600 pixels is less than 12, then the radius of the circle is increased by 50 pixels at a time until at least 12 reference stars are selected. We always have at least 12 references stars in each field, and each star is weighted equally in our astrometric analysis.

Our astrometric time series are fit in an iterative manner, first fitting the plate constants for each frame, and then stellar motion parameters for each reference star. This is repeated three times so that the plate constants can converge towards a final solution. These plate constants are then used to fit for the motion parameters of the target star.

Each plate is fit through a least squares method with a six constant linear model based on the positions of the reference stars (the target star is excluded):

$$\begin{aligned} x_i' &= A_i x_i + B_i y_i + C_i \\ y_i' &= D_i x_i + E_i y_i + F_i \end{aligned} \tag{2.1}$$

where x and y are the original flux-weighted centroid coordinates of the reference star in pixels, and A, B, C, D, E, and F are the plate constants. x' and y' are the reference star coordinates after the transformation, and are also in pixels. The linear plate constants allow for a different scale in the x and y directions, allow for translation of the frame in both directions, and corrects for any instrument rotation, as well as shearing motion in each frame. When removing the cameras on the MEarth telescopes for repairs or maintenance, disturbances to the data are likely. Our plate constants $[A, B, C, D, E, F]$ remain very close to the identity matrix plus a shift, $[1, 0, \Delta x, 0, 1, \Delta y]$ or a 180 degree rotation plus a shift, $[-1, 0, \Delta x, 0, -1, \Delta y]$ over all images. The effect of higher order plate constants is mitigated by our selection method for reference stars, and including higher order terms doesn't increase the quality of our fit for stars with previously determined trigonometric parallaxes (see section 2.3.5).

Once we have shifted and stretched the frame to align with the master frame, the coordinate system of the master frame (generated through star matching between the master frame and the 2MASS catalog) is applied to convert the x' and y' to α (R.A.) and δ (decl.). Then, we fit for both the proper motion for each reference star and the parallax for each reference star through the following method.

First, we remove the proper motion of each reference star since the time of the master frame:

$$\begin{aligned} \alpha'_{i,s} &= \alpha_{i,s} - \mu_{RA,s}\Delta t_i \\ \delta'_{i,s} &= \delta_{i,s} - \mu_{Decl.,s}\Delta t_i \end{aligned} \tag{2.2}$$

The subscript i denotes each image, s denotes the reference star, and the primed coordinate represents the transformation removing the proper motion since the master image. We then convert the stellar coordinates from R.A. and Decl. to ecliptic longitude (λ) and ecliptic latitude (β) through a rotation of the coordinate system. Then, we remove the parallax motion at the image epoch and add the parallax motion from the master image:

$$\begin{aligned} \lambda_{0,i,s} &= \lambda_{i,s} + \pi_s(P_{\lambda,0,i,s} - P_{\lambda,i,s}) \\ \beta_{0,i,s} &= \beta_{i,s} + \pi_s(P_{\beta,0,i,s} - P_{\beta,i,s}) \end{aligned} \tag{2.3}$$

where π is the parallax amplitude, and P_λ and P_β are the parallax factors in each coordinate for each star, s, and each image, i:

$$\begin{aligned} P_{\lambda,i,s} &= a_i \left(\frac{\sin(\lambda_\odot - \lambda_{0,s})}{\cos(\beta_0)} \right) \\ P_{\beta,i,s} &= -1.0 \times a_i \left(\frac{\cos(\lambda_\odot - \lambda_{0,s})}{\sin(\beta_0)} \right) \end{aligned} \tag{2.4}$$

where a_i is the Earth-Sun distance in AU at the time of the image, i, or the master frame, 0, and $\lambda_\odot$ is the solar longitude at the time of the image or the master frame.

Finally, one of eight constants is added to each individual star, for all images, depending on the side of the meridian the image was taken.

$$\begin{aligned} \lambda_{f,s} &= \lambda_{0,s} + G_{s,1,2,3,4} \\ \beta_{f,s} &= \beta_{0,s} + H_{s,1,2,3,4} \end{aligned} \tag{2.5}$$

where the subscripts 1 and 2 represent different sides of the meridian for the years 2008-2010 (before we changed the camera housing), while 3 and 4 represent the different sides of the meridian from September 2011 onward. Typical values for G and H are 0.1 arcsec. All data points are weighted equally, and our model is fit using the Levenberg-Marquardt χ^2 method. We note that in order to avoid degeneracies between the parallax and the meridian constants, G and H, it is necessary to obtain data on both sides of the meridian during the same phase of the Earth's orbit, and our data collection strategy was adjusted in the middle of the 2011-2012 observing season in order to resolve this degeneracy. If this degeneracy was present in pre-2011 data for a field of view, then those data are discarded. However, as all observations prior to 2011 were taken at planet-hunting cadence only, this occurrence is very rare, as we observed each field during the entirety of each observing night. Finally, as the meridian constants are unique to each individual star, we note that the effects of any differential color refraction can be partially corrected for through this method as well.

The plate constants, A_i, B_i, C_i, D_i, E_i, and F_i (one per image), and the stellar motion parameters, $\mu_{s,RA,DEC}$, π_s, $G_{s,1,2,3,4}$, and $H_{s,1,2,3,4}$ (one per star) are fit iteratively, while holding the other set fixed, until the solution has converged for the plate constants. If there are more than 12 reference stars available, reference stars whose motions are fit to be > 1.0 arcsec yr^{-1} or whose parallax place them closer than 100 pc are culled from the sample and the plate constants are refit with the remaining stars. We find only 23 reference stars in 17 fields fit these criteria. After these cuts, the median number of reference stars per field is 19 and the maximum number of reference stars is 90.

After the plate constants have converged, we fit the astrometric time series for the target star in the same manner as for the reference stars, fitting for the relative proper motion between the target star and the reference stars, the relative parallax between the target and reference stars, and the meridian constants ($G_{1,2,3,4}$, and $H_{1,2,3,4}$). To avoid the effect of singular outliers, we refit our model after excluding points that lie outside of three standard deviations of the residuals for our initial fit. We perform an additional test on our data by refitting the parallax signal while holding the proper motion constant to the value reported in Lépine (2005). If the fit parallax amplitude changes by more than 2σ (using the RMS of the residuals to estimate σ), then we discard this star from the sample. This test eliminated 41 stars from our sample, and we believe that this is principally due to a degeneracy between the parallax motion and the proper motion, which can be resolved in the future by gathering additional data at the proper phase of the year.

We estimate the internal errors in our trigonometric parallax measurement using a residual permutation algorithm, where we take the residuals from our best fit model, shift them one time stamp in the residual array, add them back to our best fit model, and then refit the permuted data set for the parallax amplitude, proper motions, and meridian offset constants. We apply this method only to our astrometric time series for the target star and not to the reference stars. This implicitly assumes that the errors in the frame constants (derived from the astrometric precision of the reference stars) are negligible compared to the errors in the astrometric precision of the single target star, which is valid due to the number of reference stars we have contributing to each plate solution. This method, while not allowing the flexibility of generating thousands of fake data sets (except for the minority of our stars that have over a thousand data points), has the benefit of preserving long time-scale correlated noise in our time series, and we find that our derived errors tend to be larger for stars that have fewer total measurements.

One concern with estimating our errors through this residual permutation algorithm is that for the systems which have fewer than 50 data points (for which we have 238 out of 1507 objects), there may not exist enough permutations to reliably estimate our error bars. In order to test this, we also estimate our error by refitting 1000 synthetic datasets generated by adding white noise to our observed data with a standard deviation equal to the standard deviation of our initial residuals. We find that the the error bar derived from this method is comparable in magnitude to the residual permutation method, and therefore we elect to quote the error bar derived from the residual permutation method for our results.

2.3.2 Correction to Absolute Parallax

Because our reference stars are all relatively bright stars, the reference frame itself exhibits a small parallax motion, as each reference star is also subject to the observational effects of trigonometric parallax. This effect causes us to systematically measure a smaller parallax angle and therefore a larger distance than if our reference image was static. We used the Besançon model of the galaxy (Robin et al. 2003)[2] to estimate the parallax of synthetic populations of stars along the same sight-lines as our targets. For each target, we generate a synthetic star catalog oversampled by a factor of 1000, and select only stars whose apparent magnitudes are between 8.0 and 13.0 in the I-band (an adequate approximation of our non-standard filter for this purpose). We select random subsets of these stars that match our observed reference star magnitude distribution in order to estimate the average distance to a typical reference star and the associated uncertainty. Typical corrections for these stars are between 1 and 2 mas, but can be as high as 4 mas in certain directions. We note that the uncertainty in the absolute parallax correction is negligible compared to the uncertainty in the relative parallax

---

[2] An online tool for generating synthetic star catalogs is graciously provided by the authors at http://model.obs-besancon.fr/

measurement, and therefore only quote the error in the relative parallax measurement as our total error.

2.3.3 Catalog

We release here a catalog of our results for each target star. If you want the best estimate for the distance to an individual star, use column 17 and the error in column 18. In order, the columns in this table are:

1. Lépine & Shara (2005) catalog designation number
2. Gliese Catalog number
3. LHS Catalog number
4. NLTT Catalog number
5. Right Ascension of object (J2000, hours)
6. Right Ascension of object (J2000, minutes)
7. Right Ascension of object (J2000, seconds)
8. Declination of object (J2000, degrees)
9. Declination of object (J2000, minutes)
10. Declination of object (J2000, seconds)
11. $\mu_{RA}\times$ cos(Dec) from our best fit model
12. μ_{Dec} from our best fit model
13. Julian epoch of the first data point in our fit
14. Julian epoch of the last data point in our fit
15. Relative parallax (milliarcseconds)
16. Absolute parallax correction (milliarcseconds)

17. Absolute parallax (milliarcseconds)
18. Absolute parallax error (milliarcseconds)
19. 2MASS J magnitude
20. 2MASS K magnitude
21. MEarth estimated mass of the object (using the Delfosse et al. (2000) relation; see section 4.3)
22. MEarth estimated radius of the object (using the Mass-Radius relation presented in equation 10 of Boyajian et al. 2012)
23. Error in the estimated radius equal to 5% the radius, derived from the scatter in the mass radius relation presented by Boyajian et al. (2012)
24. Number of data points in our fit
25. Number of reference stars used in our fit
26. MEarth Telescope with which the data were taken

This table is available in its entirety in a machine-readable form in the online journal.

2.3.4 Validation using stars with previously determined parallaxes

The subset of the MEarth sample presented here includes 1507 stars for which we can obtain reliable results. This includes 240 stars for which we were able to locate a trigonometric parallax determination in the literature, many of which are from the compilation available in the Yale Parallax Catalog (167 stars, van Altena & Hoffleit 1996b), Hipparcos (41 stars, Perryman et al. 1997) or Lépine (2005). A representative example of an astrometric time series with MEarth data (for LHS 64) is shown in Figure

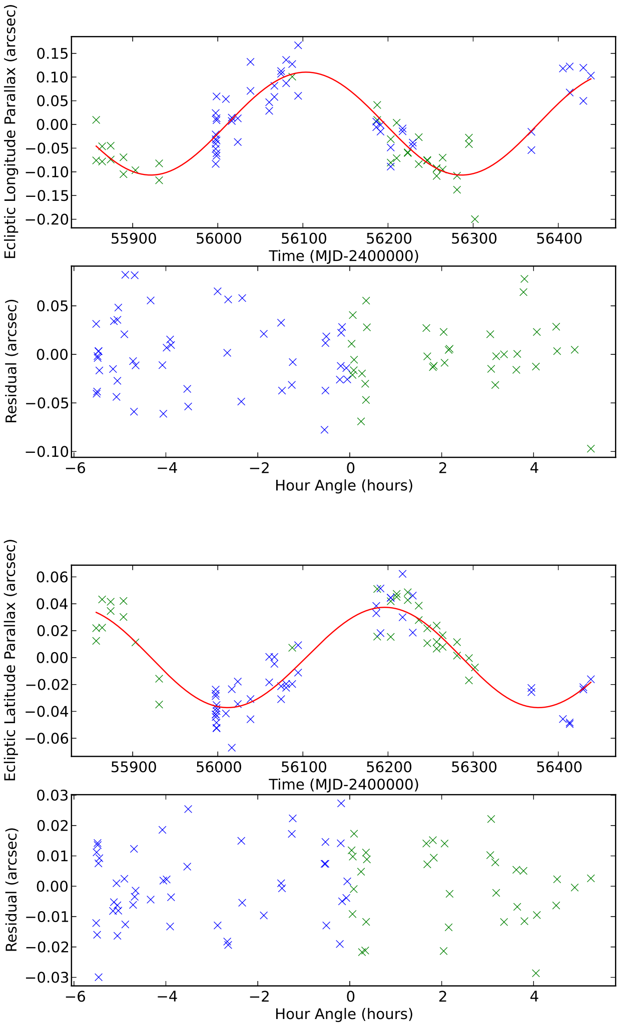

Figure 2.1: Top: Astrometric time series for LSPM J2107+5943 / LHS 64 in ecliptic longitude. Green data points and blue data points represent data taken on opposite sides of the meridian, where MEarth's telescopes have to rotate 180° due to our German Equatorial mounts. The red line corresponds to the best fit to the MEarth data using our model. Underneath we show the residuals from our best fit model for the ecliptic longitude of LHS 64 versus the hour angle the image was taken. Our derived parallax, corrected to absolute parallax of $\pi_{abs} = 41.2 \pm 1.7$ mas is not significantly different from the previous measured 41.8 ± 2.7 mas (Harrington & Dahn 1980). Bottom: Same as above but in ecliptic latitude instead of ecliptic longitude.

2.1. For this star, we find a parallax amplitude of $\pi_{abs} = 0.0412 \pm 0.0017$ arcsec, not significantly different from the previous determination in Harrington & Dahn (1980) of $\pi = 0.0418 \pm 0.0027$ arcsec, as reported by van Altena & Hoffleit (1996b). This data set is taken completely at astrometric cadence, demonstrating that our data collection strategy is sufficient to measure trigonometric parallaxes of our targets. We further note that we measure a parallax for GJ 1214 of 72.8 ± 2.4 mas, consistent with the recent determination of 69.1 ± 0.9 mas by Anglada-Escudé et al. (2013a) and the historical determination of 77.2 ± 5.4 mas provided by van Altena & Hoffleit (1996b). Therefore, we are able to accurately measure apparent stellar motion associated with trigonometric parallax, although in some cases with larger uncertainties than dedicated astrometric programs such as RECONS (Henry et al. 2006; Jao et al. 2011, and references therein) and the Brown Dwarf Kinematic Project (BDKP, Faherty et al. 2012). In Figure 2.2 we show the MEarth derived parallax motion compared to the values reported in the literature for all stars that had a previous trigonometric parallax measurement available. Literature trigonometric parallax measurements come from Monet et al. (1992), Harrington et al. (1993), Gatewood et al. (1993), van Altena et al. (1995), van Altena & Hoffleit (1996b), Tinney (1996), Ducourant et al. (1998), Benedict et al. (1999), Benedict et al. (2000), Benedict et al. (2001), Dahn et al. (2002), Reid et al. (2003a), Pravdo et al. (2004), Henry et al. (2006), Pravdo et al. (2006), Smart et al. (2007), van Leeuwen (2007c), Makarov et al. (2007), Gatewood (2008), Gatewood & Coban (2009), Lépine et al. (2009), Smart et al. (2010), Riedel et al. (2010), Khrutskaya et al. (2010), Shkolnik et al. (2012), and Anglada-Escudé et al. (2013a). The scatter of the residuals when compared to the reported literature value is approximately Gaussian. Fitting this distribution as a Gaussian, we find a best fit width ≈ 15% larger than the sum of our

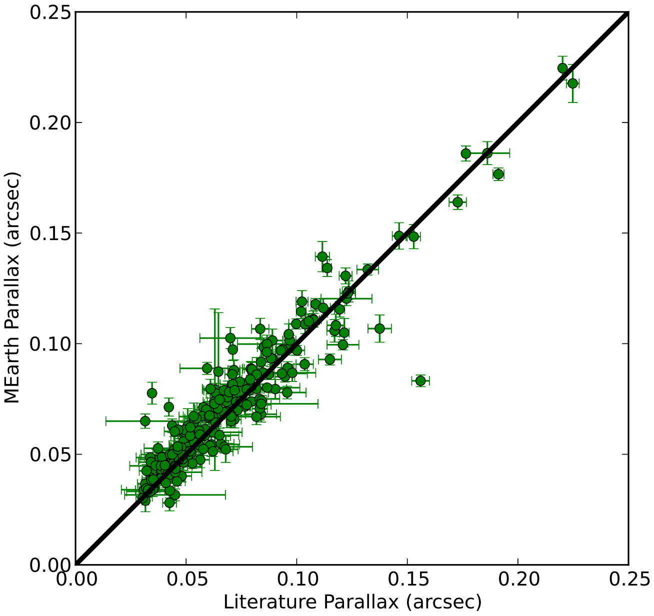

Figure 2.2: Comparison of our trigonometric parallaxes derived from the MEarth data with previous studies. We find good agreement between the two measurements, with a typical error of 4 mas, indicating that MEarth is able to reliably estimate trigonometric parallaxes to our targets. The star in the lower right is LSPM J1631+4051, and we find a trigonometric parallax of 83.2 ± 2.6 mas, significantly smaller than the measurement by Ducourant et al. (1998) of 156 ± 4 mas, but much closer to the measurement by Gliese et al. (1986) of 100 ± 29 mas.

errors and the errors reported in the literature added in quadrature (see Figure 2.3). We report our measured parallaxes and uncertainties for each target in our catalog.

2.3.5 Additional Plate Constants, Differential Refraction, and Secular Acceleration

To determine whether the plates are modeled adequately by terms that are strictly linear in the coordinates, we refit the subsample of target stars with previously determined trigonometric parallaxes with a second order plate model. We found that the additional parameters ended up improving our derived value of the parallax relative to the previously determined value for only approximately half of the stars, and the remainder of the stars showed a marginal decrease in agreement with previous values. Furthermore, on average, the fit became worse, as the standard deviation of the residuals to the literature values increased by 2 mas. Therefore, we do not believe the lack of higher order terms in our plate model to be a significant source of error in our results, and that including these higher order terms causes us to fit astrometric noise rather than real trends associated with our detectors.

Another possible source of error is differential color refraction (DCR) in the atmosphere through which our measurements are taken. Because the reference stars (from which the plate constants are derived) are, on average, bluer than the target star, the relative effects of DCR between the reference stars and the target star could become important. Stone (2002) measured the effect of differential color refraction in different optical bands as a function of color and found that the maximum DCR effect in the I-band for stars with a B-V of 2.0 is 12 mas, suggesting that the effect in our bandpass

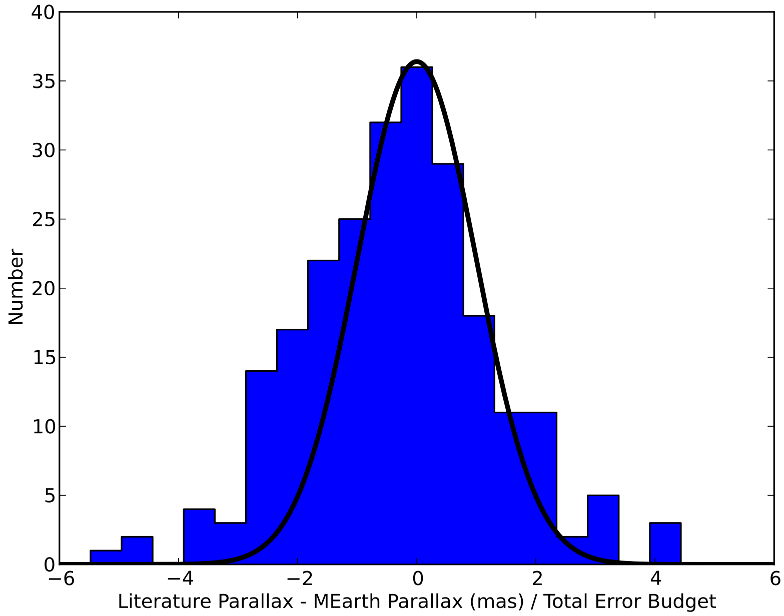

Figure 2.3: Ratio of the deviation of our measured parallaxes from previously determined parallaxes compared to the total error budget in the two measurements. The black line is a standard Gaussian with unit variance. We find that our residual permutation algorithm is able to reliably estimate the errors in our measurement, with the distribution being approximately Gaussian, with a width only 15% wider than expected. While our error distribution is asymmetric, we note that very few of our measurements are discrepant by more 3σ in total error budget.

is probably small, as the B-V color of a typical late M-dwarf is approximately 1.8. Nonetheless, we we proceed to estimate the effect that DCR should have on our data.

The effective wavelength of a typical M-dwarf target, accounting for telluric absorption, the filter bandpass, and the detector quantum efficiency is 850 nm, and is 840 nm for a typical reference star. We assume a typical target is a M5V star (Pickles 1998), and that a typical reference star is a G2V star. The index of refraction for air at 15°C, and standard atmospheric pressure (760 mm Hg) at these wavelengths is $n_{840\mathrm{nm}} = 1.00027482$ and $n_{850\mathrm{nm}} = 1.00027477$ (Ciddor 1996). However, typical conditions at the MEarth observatory on Mt. Hopkins are significantly different than standard atmospheric conditions. The seasonal average temperature is 10°C and the typical pressure is 575 mm Hg. Additionally, the amount of water vapor in the air also affects index of refraction of the atmosphere. For a typical relative humidity of 30%, at these conditions the partial pressure of water is 2.8 mm Hg (Ahrens 1994). Correcting the index of refraction for these effects using the methods in Filippenko (1982) and Barrell (1951), we find that the expected differential color refraction between our reference stars and the target M-dwarfs is typically 6 milliarcseconds at airmass = 1.41, and 10 milliarcseconds at airmass = 2.

Our model is capable of accounting for some of the DCR signal with the meridian constant parameters G and H. These constants are fit on a star by star basis, and therefore the "mean" DCR correction term for each star in each dataset becomes merged into the meridian correction for each star. Any residual differential color effect will only be a second order effect and much smaller than 10 mas, below our threshold for detection.

To investigate whether any significant effects due to airmass or color remain in our data, we show the residuals in each coordinate direction (ecliptic longitude and ecliptic latitude) as a function of the hour angle at which the image was taken, in Figure 2.1. We find no significant directional offset between the residuals and the airmass the image was taken (for the representative star in Figure 2.1 as well as for the sample presented here in general), and conclude that the effect of differential color refraction in the MEarth bandpass on our astrometry is negligible.

For nearby stars with large radial velocity, the effect of secular acceleration (a changing of a star's angular proper motion as a result of its changing solar distance) may become important, as our model assumes a constant angular velocity for each star. Barnard's star, the fastest moving star in the sky, has a secular acceleration of approximately 1.2 mas / yr (van de Kamp 1935). Because our astrometric model is fitting for the average proper motion over a maximum of a 4 year time period, this can only result in a maximum systematic of ≈ 2.5 mas, below our detection threshold. Therefore, we ignore any effects of secular acceleration for all of our targets.

We further investigated whether the residuals in our derived parallaxes compared to previous results was correlated with other external parameters. We find no correlation with the brightness of our target star, the average brightness of our reference stars, the color of the target star, the average color of the reference stars, or with intrapixel variation (evaluated by looking at our residuals as a function of sub-pixel position).

2.4 Results and Discussion

2.4.1 Comparison to Photometric Distance Estimates

All of the stars in our sample have estimated distances from the Lépine (2005) piece-wise linear relationship in $V_{est} - J$ color. The V_{est}-magnitudes for our targets all come from this catalog. This relation was calibrated from the 3104 M dwarfs from the LSPM North catalog (Lépine & Shara 2005) that had trigonometric parallax measurements, and has a mean error of 35% on the distance estimate. We note that most of the estimated V magnitudes in Lépine (2005) come from photographic plate measurements, and some have uncertainties as large as 0.5 mag. We note that high quality V photometry is available for some of the stars where photographic estimates were used by Lépine (2005), however for the purposes of this work, we use the estimated V magnitudes compiled by Lépine (2005). In Figure 2.4, we show the distance modulus as expected from the photometric distance, using the calibration from Lépine (2005), compared to the value derived from the MEarth astrometry, as well as stars that have previous trigonometric parallax determinations available. In this plot, an equal mass binary would have an offset of 0.75 in distance modulus from the photometric distance modulus estimate. However, we find that that photometric distance estimates have a significantly higher scatter than trigonometric measurements, and that the typical scatter in the photometric measurement is large enough that identifying equal mass binaries through comparison of photometric estimates with our trigonometric parallaxes is not trivial.

We note that previous estimates of the binary fraction among M0-M5V stars place the multiplicity fraction at $42\% \pm 9\%$ (Fischer & Marcy 1992), $27\% \pm 16\%$ (Gizis & Reid

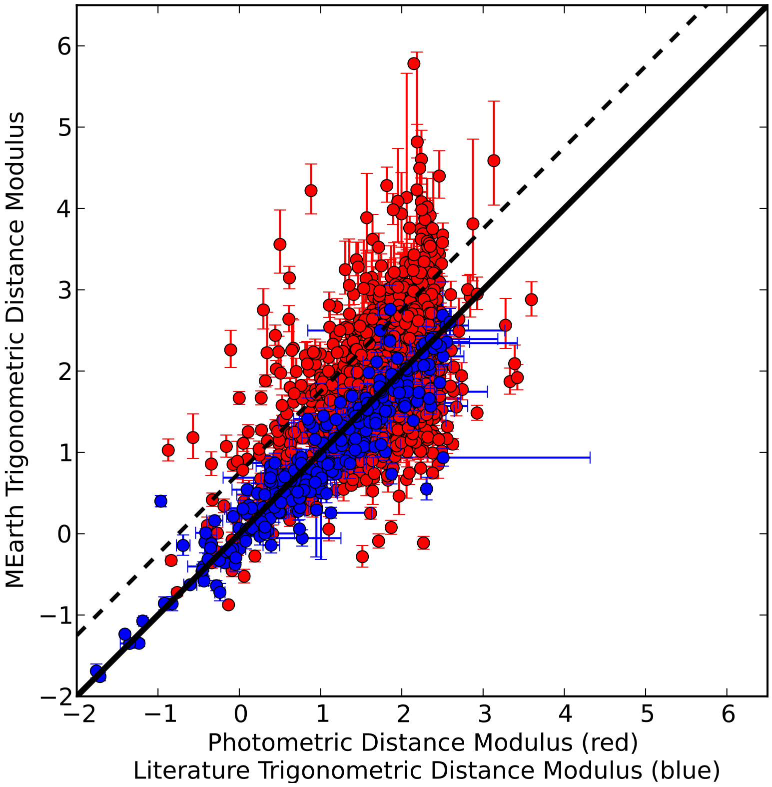

Figure 2.4: Plot of the MEarth distance modulus versus the expected distance modulus from either previous literature measurements (blue) or the piece-wise linear V-J fit from Lépine (2005) (red). Unresolved equal mass binaries should fall on the dashed line. We note that the MEarth astrometric result is consistent with previous parallax studies and has a much lower dispersion than photometric estimates.

1995), or 27% ± 3% (Janson et al. 2012a), with a trend towards smaller multiplicity fraction for lower mass primaries (which the MEarth survey preferentially targets). Fischer & Marcy (1992) find that the binary distribution for M-dwarfs peaks with companion objects having an orbital period between 9 and 220 years, and they used a range of detection techniques, including spectroscopy, speckle interferometry, and direct imaging. Gizis & Reid (1995) and Janson et al. (2012a) relied on imaging, and lucky-imaging techniques respectively, and therefore are not as sensitive to tighter multiple systems. Regardless, there is likely to be a significant amount of contamination with target stars that are actually unresolved binaries. As the MEarth survey target list was designed with a distance cut-off, and it is harder to resolve close binaries at larger distances, it is likely that the contamination is due primarily to unresolved binary systems further than 33 pc masquerading as single stars estimated to be within 33pc. Using only a photometric distance measurement means that the volume in which an equal mass binary can masquerade as a single star is $2^{3/2}$ larger than the volume in which we aim to obtain our sample. Removing these stars from our sample before investing a significant amount of observing time to discover whether these stars have transiting planets will make the MEarth survey more effective at finding planets. With significantly improved stellar distances, the limiting factor in distinguishing unresolved multiples from single stars is the quality of the available photometry that can be either compiled or gathered for these objects. We are currently working on calibrating the MEarth data to obtain accurate absolute optical magnitudes, and hope in the near future to use these data to determine which of our targets are likely binaries. However, for the rest of this paper we assume that all stars in our sample are single stars.

2.4.2 Survey Completeness and Mapping the Solar Neighborhood

The MEarth survey is designed to look at nearby mid-to-late M dwarfs within 33 pc of the Sun, primarily drawn from the catalog compiled by Lépine (2005). However, we note that in designing this sample, we have introduced spectral type dependent metallicity biases, as the V_{est} magnitude has a dependence on metallicity as well as spectral type. The Lépine (2005) catalog was designed to be approximately 50% complete out to 33 pc with the goal of being mostly complete out to a distance of 25 pc. With our estimates of the trigonometric parallaxes for each star, we are now in a position to determine how complete the census of the solar neighborhood is out to these distances for the types of stars in the MEarth sample. Assuming that on these small scales the effects of Galactic structure are negligible, we can assume that the cumulative number of MEarth targets should increase linearly with the volume, with radius R as R^3. In Figure 2.5, we show the cumulative number of MEarth targets out to 50 pc, with a best fit R^3 line, fit to the cumulative number of stars from 5pc to 15 pc. We omit the cumulative number of stars on scales smaller than 5 pc because there are not a sufficient number of stars to make a reliable estimate.

In Figure 2.6, we plot the ratio of the number of stars to the number we expect to find for stars with a $V_{est} - K < 5.5$ (M4.5 and earlier), $5.5 < V_{est} - K < 6.5$ (between M4.5 and M5.5V), and for stars with a $V_{est} - K > 6.5$ (spectral types later than M5.5V). We plot both the sample of stars for which we measure parallaxes (presented here), and all stars that originally made the initial MEarth target selection from Nutzman & Charbonneau (2008), for which the majority MEarth has taken data. For stars that do

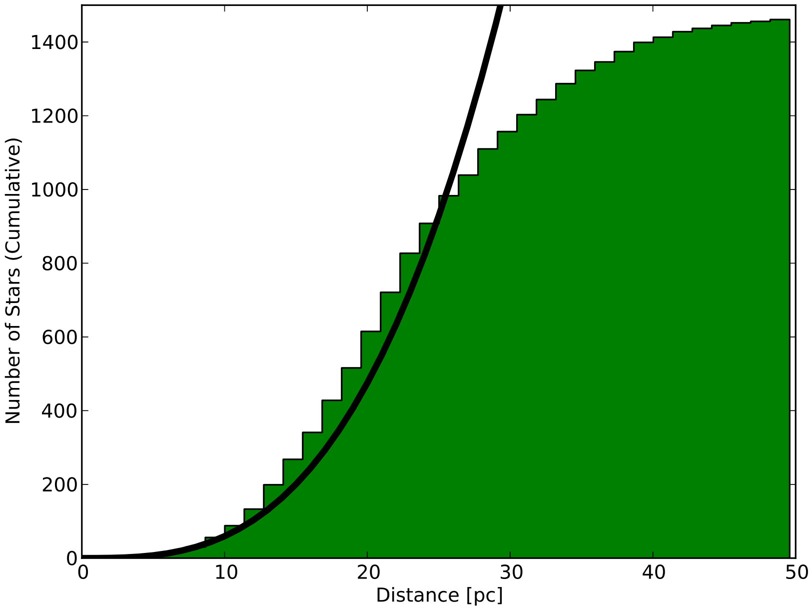

Figure 2.5: Top: Cumulative histogram of the number of MEarth targets as a function of distance from the Sun. Overplotted is a black R^3 line, normalized to the best fit cubic for the number counts between 5 and 15 parsecs.

not have a measured parallax from the MEarth data, we use an estimated distance from a spectroscopic measurement (if available) or its $V-K$ color. Each color bin is fit to an R^3 power law using the cumulative number counts between 5 and 15 parsecs, and the ratio of the number of stars we find within that distance to that expected from our fit is what we define as the completeness ratio. The sample of new MEarth parallaxes used to construct this plot has one known incompleteness: it is missing some stars earlier than M4.5 in spectral type at distances less than 15 pc, because these stars were too bright for MEarth to observe efficiently. However, because we base our completeness estimates on the number of stars between 5 and 15 pc, we therefore underpredict the local density of M4.5 dwarfs and earlier and appear overcomplete at distances above 15 pc for these stars in the top panel of Figure 2.6. As expected, this artifact largely disappears in the bottom panel of Figure 2.6, when we include all stars regardless of whether or not MEarth measured a new parallax for them. For the full sample, we find that for stars with a $V_{est}-K$ color less than 6.5, we are nearly complete out to a distance of 25 parsecs, but for redder stars, our completeness begins dropping off at the smaller distance of 20 parsecs. New searches for these smaller, redder objects, utilizing WISE data for example, may identify these missing objects in the near future. We do not find a clear correlation between completeness and Galactic latitude, which indicates crowding and confusion in the Galactic plane may not be the limiting factor in identifying the missing systems (see Figure 2.7).

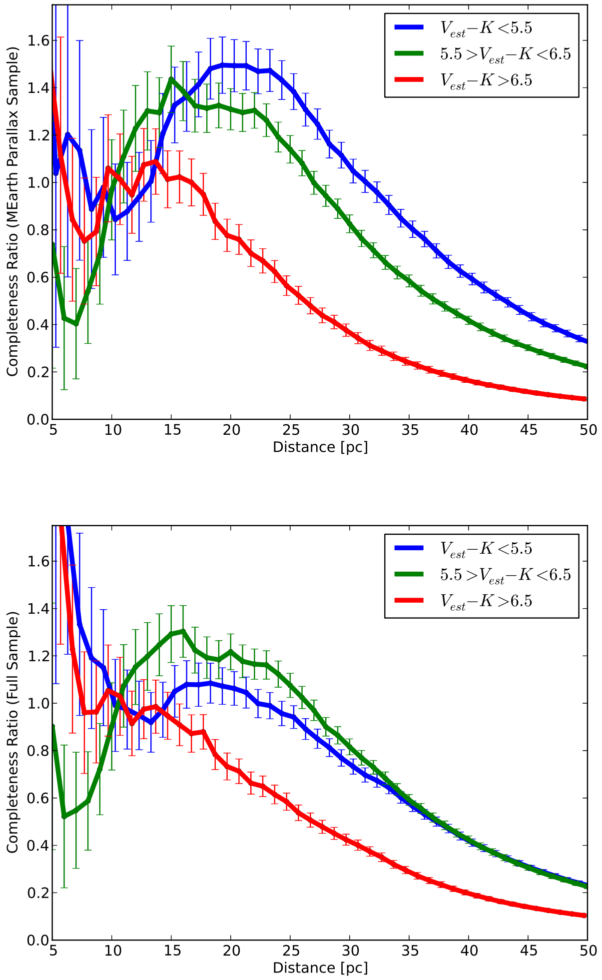

Figure 2.6: Top: Completeness ratio for stars with $V_{est} - K < 5.5$ (approximately M4.5 and earlier, blue), $6.5 > V_{est} - K > 5.5$ (between M4.5 and M5.5V, green), and $V_{est} - K > 6.5$ (later than M5.5V, red), where the completeness ratio is defined as the cumulative number of stars within a distance limit, over what would be expected from a cubic function fit to the cumulative number between 5 and 15 parsecs. Bottom: Same as above, but for the full sample of stars from Nutzman & Charbonneau (2008), where we use the trigonometric distances presented here when applicable, and photometric or spectroscopic distances from Lépine (2005) for the remainder of the stars.

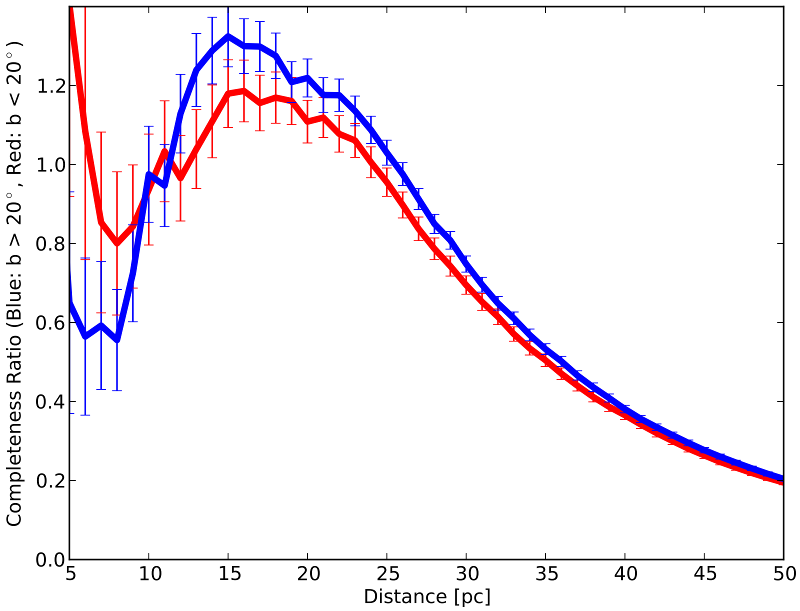

Figure 2.7: Completeness ratio for stars with Galactic lattitude $b > 20$ degrees (blue) and $b < 20$ degrees (red), where the completeness ratio is defined as the number of stars detected, over what would be expected from a cubic function fit to the cumulative number between 5 and 15 parsecs. We find weak correlation with Galactic coordinate and completeness, indicating that confusion and source crowding is not the limiting factor in identifying nearby M-dwarfs. Error bars are strictly Poisson.

2.4.3 Changes to Stellar Physical Parameters and Application to the MEarth Planet Survey

We can now estimate the masses and radii of our stars more reliably, aiding our understanding of the physical characteristics of individual M-dwarfs in the solar neighborhood. Specifically, we can more reliably estimate the intrinsic brightness of our targets, and through previously published relationships, estimate the mass and radius of each star.

Delfosse et al. (2000) obtained an empirical relation between the masses of low mass stars and their luminosities in the near infrared, with the smallest scatter obtained in the K band. As each of the MEarth targets have precise K band magnitudes as measured by 2MASS (Skrutskie et al. 2000), we can use these measurements with our trigonometric parallax measurements to obtain more reliable masses for each star. Similarly, by using the mass-radius relation for low mass stars obtained by Bayless & Orosz (2006), we can obtain more reliable radii for each star. Both of these are important for characterizing MEarth's sensitivity to planetary transits in these systems.

In Figure 2.8, we show histograms of our newly derived stellar masses and radii compared to the values derived by Nutzman & Charbonneau (2008), which used the photometric distance measurement and the same mass-radius relationship. For stars where the newly estimated mass is $M < 0.5$ $M_{\odot}$, we find a median of the absolute value of the offset of $\Delta M \approx 0.08$ $M_{\odot}$, whereas if we take the global sample, we find a median of $\Delta M \approx 0.12$ $M_{\odot}$, as the initial MEarth sample was constructed to be limited to only the mid-to-late M dwarfs. We note that the stars to which we assign higher mass values are located further away than photometrically indicated and may instead be unresolved binary or multiple systems. Additionally, a systematic trend of the $V_{est} - J$ colors being too red would also systematically shift our stars to higher estimated mass once we have obtained trigonometric parallax distances to them. Similarly, the typical change in the stellar radius is also $\Delta R \approx 0.08$ $\mathrm{R}_{\odot}$ for stars whose mass from MEarth astrometry was $M < 0.5$ $\mathrm{M}_{\odot}$ and $\Delta R \approx 0.12$ $\mathrm{R}_{\odot}$ for stars whose final mass was $M < 0.8$ $\mathrm{M}_{\odot}$.

Importantly, the stellar radii of our targets determine our sensitivity towards transiting exoplanets in the systems, as the transit depth is approximately proportional to the ratio of the areas of the stellar disk and planetary disk. Because MEarth's observing strategy is to obtain a per-pointing signal to noise ratio sufficient to detect a 2 $\mathrm{R}_{\oplus}$planet transiting in front of the star at a significance of 3σ, an accurate estimation of the radius is essential to our ability to detect a transiting planet of a given size. Because large planets tend to be rare around small stars (Gaidos et al. 2012; Morton & Swift 2013; Dressing & Charbonneau 2013), obtaining the appropriate exposure time is essential for MEarth to accomplish its science goals. Additionally, the mass of the host star directly determines the planet's orbital period at a given separation, and directly affects the temperature of the planet as well. Therefore, characterization of a planet directly depends on the host star's physical parameters. As of the 2012-2013 observing season, MEarth is using these new radius determinations to determine which targets are observed in a given season and to set the integration times for these targets.

Aside from the transit depth of a detected companion being dependent on the stellar radius, we also note that obtaining accurate stellar parameters will also affect our understanding of any discovered planet's habitability. The boundaries of habitable zones is currently a topic of debate (see, for example, Gaidos 2013; Danchi & Lopez 2013; Kopparapu et al. 2013), but even in the most simple definition (distance at which

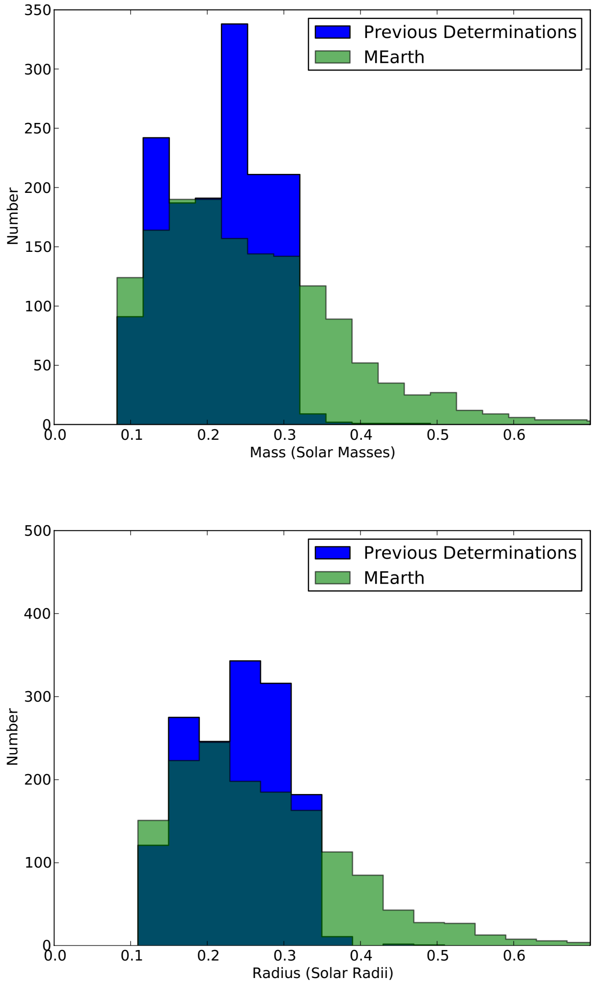

Figure 2.8: Top: Histogram of the distribution of stellar masses of the MEarth target stars based on our previous photometric determinations (blue, Nutzman & Charbonneau 2008) and based on the absolute K magnitude derived from the MEarth astrometric data and the 2MASS survey (green). We find the peak of our distribution shifts towards smaller mass stars but there is a significant long tail of stars with higher masses (due to being further away) than previously estimated. We note that at the extremely high mass end ($M >\sim 0.75 M_{\odot}$), the Delfosse et al. (2000) relation is no longer accurate, and that stars in this region are likely to be unresolved binaries, as color information makes them unlikely to be earlier type stars. Bottom: Identical, but transforming mass to radius with the relation published by Bayless & Orosz (2006).

the equilibrium temperature of a blackbody supports the existence of liquid water), the period of a planet in the habitable zone of the more massive M-dwarfs in our sample have longer orbital periods than what can be easily detected with the MEarth observatory. Therefore, by shifting our priority to smaller M-dwarfs, we are sensitive to smaller planets at all orbital distances, and increase our rate of recovery for planets in the habitable zones of the target stars.

2.4.4 New Stars Within 10 pc of the Sun

While the census of the solar neighborhood out to 10 parsecs is largely complete down to the mid-M dwarfs, there are several stars for which photometric distances place them within or near to the 10 parsec boundary, but for which there is no published trigonometric parallax. In the sample presented here, we find 37 stars whose trigonometric parallaxes place them within the 10 parsec radius boundary. Of those 37 stars, 29 of them have previously measured parallaxes that confirm this distance. The rest of the stars have photometric $V - K$ distance estimates that place them within 10 parsecs of the Sun, and we therefore confirm their proximity to the Sun.

2.5 Conclusions

With trigonometric parallaxes for 1507 stars, we have greatly enhanced our map of the solar neighborhood. When the MEarth survey concludes, we will have also probed this sample with nightly cadence over a multi-month baseline, to measure rotation periods, activity levels, flare occurrences, and the presence of small planetary bodies approximately 2.0 $R_\oplus$ in orbits extending into the classical habitable zone of these stars (P $\approx$ 14 days for an M5V star). The scientific yield from the MEarth survey extends far beyond the goal of finding planets, and in particular, new trigonometric parallaxes can already begin to yield additional insights into stellar astrophysics - particularly the unclear relationship between luminosity, metallicity, age, and activity.

We have presented here a catalog of trigonometric parallaxes for 1507 mid-to-late M-dwarfs, 1267 of which had no previous trigonometric parallax measurement. The revised distances indicate 8 stars without previous trigonometric parallax measurements lie within 10pc of the Sun. We have increased the number of stars in the MEarth sample with trigonometric distance estimates by a factor of 6, and increased the total number of stars within 25 pc of the Sun with trigonometric parallax measurements by 682 stars, $\approx$ 30% of the currently identified 25 parsec sample.

Furthermore, our study has better informed us of the stellar parameters of our targets, most importantly mass and radius. This knowledge has changed the way we have conducted our survey by changing the priority with which we survey our stars. Accurate stellar characterization is an essential step in any transiting planet survey, and these measurements will greatly enhance the MEarth survey, and reduce our uncertainty in the planet occurrence rate around mid to late M-dwarfs. In addition, MEarth-South, a copy of the current MEarth-North array, will be operational in Chile in the near future, surveying an additional $\approx$ 2000 stars in the southern hemisphere. We will begin operating this array with astrometric and planet-hunting cadence as well, and expect to obtain accurate trigonometric parallaxes for these stars as early as 1 year after first light, with fits improving in subsequent years.

Our efforts to characterize the nearby stars in the solar neighborhood complement the GAIA mission, which is set to launch at the end of 2013. Over the course of its mission, GAIA will systematically survey the entire sky, obtaining astrometric precision of several microarcseconds for the brightest stars in the sky and collecting data down to a limiting magnitude of $V = 20$. However, it will take several years for GAIA to collect enough data to disentangle the effects of proper motion and parallax motion, while current ongoing photometric and RV surveys for planets around small stars need accurate data to characterize their systems in the short term. Until more precise data is obtained by the GAIA spacecraft, the catalog presented in this paper can characterize these stellar systems.

Acknowledgments

We would like to thank the input of our referee, Dr. John Subasavage, whose comments have improved the quality of this manuscript. The authors would like to acknowledge W. Olson for his extensive assistance in code optimization, without which our results would have taken far longer to compile. We acknowledge the work of M. Irwin, which we used in this research. We gratefully acknowledge funding for the MEarth Project from the David and Lucile Packard Fellowship for Science and Engineering and from the National Science Foundation (NSF) under grant numbers AST-0807690 and AST-1109468. The MEarth team is grateful to the staff at the Fred Lawrence Whipple Observatory for their efforts in construction and maintenance of the facility and would like to thank W. Peters, T. Groner, K. Erdman-Myres, G. Alegria, R. Harris, B. Hutchins, D. Martina, D. Jankovsky, T. Welsh, R. Hyne, M. Calkins, P. Berlind, and G. Esquerdo for their support. This research has made use of NASA's Astrophysics Data System.

Chapter 3

Calibration of the MEarth Photometric System: Optical Magnitudes and Photometric Metallicity Estimates for 1802 Nearby M Dwarfs

This thesis chapter originally appeared in the literature as

J. A. Dittmann, J. M. Irwin, D. Charbonneau, E. R. Newton

The Astrophysical Journal, 818, 153, 2016

Abstract

The MEarth Project is a photometric survey systematically searching the smallest stars nearest to the Sun for transiting rocky planets. Since 2008, MEarth has taken approximately two million images of 1844 stars suspected to be mid-to-late M dwarfs. We have augmented this survey by taking nightly exposures of photometric standard stars and have utilized these data to photometrically calibrate the *MEarth* system, identify photometric nights, and obtain an optical magnitude with 1.5% precision for each M dwarf system. Each optical magnitude is an average over many years of data, and therefore should be largely immune to stellar variability and flaring. We combine this with trigonometric distance measurements, spectroscopic metallicity measurements, and 2MASS infrared magnitude measurements in order to derive a color-magnitude-metallicity relation across the mid-to-late M dwarf spectral sequence that can reproduce spectroscopic metallicity determinations to a precision of 0.1 dex. We release optical magnitudes and metallicity estimates for 1567 M dwarfs, many of which did not have an accurate determination of either prior to this work. For an additional 235 stars without a trigonometric parallax, we provide an estimate of the distance assuming solar neighborhood metallicity. We find that the median metallicity for a volume limited sample of stars within 20 parsecs of the Sun is $[\mathrm{Fe/H}] = -0.03 \pm 0.008$, and that 29 / 565 of these stars have a metallicity of $[\mathrm{Fe/H}] = -0.5$ or lower, similar to the low-metallicity distribution of nearby G-dwarfs. When combined with the results of ongoing and future planet surveys targeting these objects, the metallicity estimates presented here will be important in assessing the significance of any putative planet-metallicity correlation.

3.1 Introduction

M dwarfs are the most common type of star in the universe, making up approximately 75% of all stars. Despite their ubiquity, they remain poorly understood. M dwarfs span a large range in mass, from 0.6 $M_\odot$ to the hydrogen burning mass limit at approximately 0.08 $M_\odot$. This factor of 7.5 in mass ratio from the early to late M dwarfs is comparable to the mass ratio between the entirety of the AFGK spectral sequence. Over this mass range, the photospheric effective temperature of these stars cools such that molecular species (TiO, VO, CO, FeH, among others) begin to dominate the optical spectrum, significantly depressing the optical flux as well as cluttering the spectrum with many overlapping lines and bands. This effect makes line-by-line spectral analysis in these stars challenging. Modeling these features in bulk is also extremely difficult because accurate and complete line lists for many identified species are unavailable and some lines have yet to be identified.

In order to get around this inherent difficulty, progress has been made in calibrating empirical relations using M dwarf stars in wide visual binaries with better understood F, G, or K primary stars. Because they are physically associated, they likely formed out of material with the same bulk composition. Therefore the metallicity measured for the FGK primary star can reasonably be assumed to be the metallicity of the M dwarf, and an empirical relation can be calibrated. Bonfils et al. (2005) conducted a study of 20 M dwarfs binaries with a solar type primary and were able to calibrate a photometric metallicity relation using the M dwarf's M_K magnitude and $(V - K)$ color with a precision of 0.2 dex. A further study by Johnson & Apps (2009) found that this calibration systematically underestimated M dwarf metallicities by nearly 0.3 dex for M dwarfs with high metallicities, which was outside the range in the Bonfils et al. (2005) calibration sample. However, they confirmed a key finding of Bonfils et al. (2005): the optical − infrared color of an M dwarf is significantly affected by the metallicity of the star. Schlaufman & Laughlin (2010) expanded this work and attempted to correct systematic issues with both the Bonfils et al. (2005) and the Johnson & Apps (2009) calibrations. They altered the calibration on the edges of the metallicity range investigated, as well as expanded the calibration to a wider range of spectral types and increased the size of the calibration sample. The standard deviation of their fit was also reduced to 0.15 dex. All three of these calibrations were tested by Neves et al. (2012) on an independent sample of FGK - M common proper motion binaries, who found that the relation in Schlaufman & Laughlin (2010) performed the best, with an RMS residual of 0.19 dex.

Considering spectroscopy, recent progress has been made by moving to near infrared spectra, where the density of lines is much sparser and it is easier to measure a reliable continuum value. Rojas-Ayala et al. (2010) found that the combination of the Na I doublet and the Ca I triplet in the infrared K-band are reliable metallicity indicators, provided one accounts for the temperature of the star with a temperature indicator, such as the H_2O-K2 index. Rojas-Ayala et al. (2010) calibrated this correlation using common proper motion pairs of M dwarfs paired with main sequence FGK stars. This calibration was then updated by Rojas-Ayala et al. (2012) and applied to 133 solar neighborhood M dwarfs. A similar calibration in the H-band utilizing 22 common proper motion pairs was created by Terrien et al. (2012) with a precision of 0.14 dex. Newton et al. (2014) pushed these techniques into the mid-to-late M dwarf regime with spectra of 447 nearby M dwarfs and found that the metallicity of these stars is correlated solely with the equivalent width of the Na line in the near infrared K band to an accuracy of 0.12 dex. Further studies have found that Magnesium and Aluminum features in the near-infrared H-band are good indicators of temperature, radius, and the luminosity of the star (Newton et al. 2015a). Attempts to extend this calibration method to the optical regime, where spectral instrumentation is more efficient and more prevalent, have also begun to meet with success. Mann et al. (2013a) combined optical and infrared spectra spanning 0.35 - 2.45 microns and found metallicity sensitive features throughout the spectrum. While the infrared features produced a tighter calibration with a precision of 0.1 dex, an optical-only calibration delivered a precision of 0.16 dex. Mann et al. (2014) expanded on this optical-only approach (with comparable precision) by bootstrapping the calibration down to later spectral types through early M dwarf - later M dwarf binary pairs.

Interest in M dwarfs has recently grown due to their attractiveness as targets for planet searches. Their small masses and radii increase the signal amplitudes from both radial velocity (RV) and transit measurements, making detection and detailed characterization of any discovered planetary system easier and accessible from the ground. A number of current and future planet hunting surveys are exclusively focused on M dwarfs or spend a significant amount of observing time on low mass stars. MEarth is an ongoing photometric survey of mid-to-late M dwarfs in the solar neighborhood (distance, $D \lesssim 33$ pc), looking for low mass rocky planets whose periods may extend into the habitable zones of their stars (Nutzman & Charbonneau 2008; Berta et al. 2013; Irwin et al. 2015). The MEarth-North array in Arizona has been in operation since 2008, while a copy of the array in the southern hemisphere, MEarth-South, began operations in early 2014. MEarth is, by necessity, a targeted survey because the nearby M dwarfs are distributed uniformly over the sky. There is typically one target per observing field, in sharp contrast to wide field transit surveys, which observe every star in the field of view. By the nature of this design, properly characterizing targets for prioritization is essential for the survey.

When preferentially selecting low mass stars as targets for planet surveys, other astrophysical factors may become important in assessing the probability that any individual star hosts a planetary system. The metallicity of the star may have important effects on the planet formation process. Fischer & Valenti (2005) found that a simple power law in metallicity is sufficient to describe the probability that a star hosts a close and massive planetary companion, and that there is no indication of the migration process of extrasolar planets polluting their host star's atmosphere with metals. It is unclear whether this planet-metallicity correlation extends down to smaller mass planets. Schlaufman & Laughlin (2011) suggested that a planet-metallicity correlation may be present for small planets around K dwarf stars, but this was later explained by Mann et al. (2012) as contamination in their sample by giant stars. Studies of *Kepler* stars hosting short period transiting planets have indicated that the existence of large planets in close-in orbits is correlated with stellar metallicity but the existence of small planets is not correlated with metallicity (Buchhave et al. 2012b; Everett et al. 2013; Buchhave et al. 2014b). However, recent work from Wang & Fischer (2015) has again questioned this conclusion, suggesting that there is a universal planet-metallicity correlation across all sizes and all metallicities. Schlaufman (2015) also investigates this question and finds that stellar metallicity does not affect the radius distribution of small planets that form in a system.

Investigating any putative planet-metallicity correlation down into the M dwarf regime requires a reliable metallicity measurement for a statistically significant number of

M dwarfs obtained in a uniform manner, whether that be spectroscopic or photometric. A well-calibrated metallicity measurement of different elemental species assessed directly from spectral measurements is ideal but would require substantive amounts of observing time. Photometric methods lend themselves to larger sample sizes but are hindered by the need for an accurate distance measurement through trigonometric parallax combined with a well determined optical - infrared color. Unfortunately, the nearby M-dwarfs typically lack one or more of these data products. Very few of these stars had accurate distance measurements, as these stars are too dim to have been measured by *Hipparcos* (Perryman et al. 1997). Recently, we have published trigonometric distances to approximately 1500 northern hemisphere M dwarfs from the MEarth survey (Dittmann et al. 2014a). Accurate distance determinations to nearby small stars are still incomplete, particularly in the southern hemisphere, but will soon be much improved by the *GAIA* mission, now operating. Generally, these studies have broadly eliminated the bottleneck of accurate distance measurements preventing further development of photometric calibration techniques. However, many of the solar neighborhood M dwarfs have only optical magnitudes from photographic plates, with uncertainties of 20% or more (Lépine 2005).

In this paper we will describe a photometric calibration of the $MEarth$ bandpass, allowing us to have a large sample of M dwarfs with optical magnitudes measured in a uniform manner. We combine these magnitudes with a compilation of direct distance determinations and spectroscopic measurements to calibrate a color-magnitude-metallicity relation. This relation is valid for stars between $M = 0.10M_{\odot}$ and $M = 0.36M_{\odot}$ and has a precision comparable to that of spectroscopic techniques. We release a photometric metallicity estimate for 1567 M dwarf stars in the Northern hemisphere observed with the MEarth survey, and compare the metallicities of the population of nearby M dwarfs with that of nearby G dwarfs. In section 2, we describe the MEarth observatory, target list, and data collection strategy. Section 3 details our data analysis method, photometric model, and our calibration of a photometric metallicity relation. In section 4, we interpret out results for a volume limited sample of the solar neighborhood. We conclude with brief remarks about future work.

3.2 Observations

While the MEarth-South observatory has been in operation since early 2014, we are considering the data only from the northern array for this work. The MEarth-North Observatory is an array consisting of 8 identical f/9 40 cm Ritchey-Chrétien telescopes on German equatorial mounts at the Fred Lawrence Whipple Observatory on Mount Hopkins, Arizona. The telescopes are controlled robotically and collect data every clear night from September through July. The facility is closed every August for the summer monsoons. Each telescope contains a 2048 × 2048 pixel CCD with a pixel scale of $\approx 0.76''$ pix^{-1} and a Schott RG715 glass filter with anti-reflection coating. The CCD is an e2v CCD42-40 back-illuminated, midband coated AIMO device. The Schott RG715 glass filter consists of two 1.5 mm thick pieces of glass. We provide a quantum efficiency tabulation for our CCD and the transmission for our filter in Table 3.1. We note that this tabulation is for a CCD temperature of $-20°$C, and that there should be a small difference from the operating temperature of $-30°$C, which we have not measured. The effect of the telescopes' mirrors on the overall quantum efficiency is also negligible. While an aluminum coating would vary in reflectivity by approximately

20% over our bandpass, we are using a customized enhanced aluminum coating from Spectrum Coatings (Deltona, FL), with variations expected to be less than 1%.

While MEarth-North has been in operation since 2008, in the 2010-2011 season we replaced our Schott RG715 glass filter with a custom filter similar to a Cousins I filter, in the hope that it would reduce noise from changes in the precipitable water vapor. However, this filter setup did not decrease the noise in our observations, so we switched back to the Schott RG715 filter for the following years. Because of this instrumental change, we will be using data from only the 2011-2014 seasons for the purposes of the absolute photometry presented here.

The MEarth cameras are operated at $-30°$C, and before each exposure we adopt a pre-flash of the detector. While this increases the dark current (which we subsequently subtract off), it suppresses persistence from the previous exposure. We do not detect any discernible effects of residual persistence on the MEarth photometry (at the millimag level used for the planet survey), and we do not believe it to be significant. Each night we gather flat field frames at dawn and at dusk. Because the MEarth telescopes use German equatorial mounts, we must rotate the telescope by 180° relative to the sky when crossing the meridian. We take advantage of this for flat fielding by obtaining adjacent pairs of flat field images on opposite sides of the meridian to average out large-scale illumination gradients from the Sun and the Moon. Scattered light concentrates in the center of our field of view where our target is typically located. The amplitude of this effect is approximately 5% of the average value of the sky across the CCD. In order to correct for this, we filter out all large scale structure from our combined twilight flat field and use it only to track small scale features such as inter pixel sensitivity and dust shadows. We derive the large scale flat field response from dithered photometry of dense

Table 3.1:: Quantum Efficiency (QE) of the MEarth CCD, and Filter Throughput (Stub)

Wavelength (nm)	QE (CCD)	Transmission (MEarth Filter)	Product
650	0.907	0.000	0.000
660	0.901	0.000	0.000
670	0.895	0.000	0.000
680	0.887	0.000	0.000
690	0.879	0.005	0.005
700	0.869	0.059	0.051
710	0.857	0.311	0.267
720	0.845	0.666	0.563
730	0.831	0.866	0.720
740	0.816	0.941	0.768
...	...	...	...

This table is available in its entirety in machine-readable form in the online version of the paper.

star fields. Due to the longer wavelength to which our bandpass extends, we must also correct for fringing on the CCD. We find that this effect has an amplitude of 3% across the field of view of the CCD. Fringe frames are gathered by taking long exposures of sparsely populated fields and co-adding them together.

We measure the non-linearity of our detectors using a dedicated sequence of dome flats. At all count levels, the MEarth CCDs have a slightly nonlinear conversion of photoelectrons to data number, increasing from 1% to 2% at half the detector full well to 3% to 4% near saturation. In order to perform accurate photometry, this effect needs to be minimized and corrected. The MEarth target stars are generally a different magnitude than the comparison field stars. The MEarth pipeline has been developed to minimize non-linear CCD effects as part of our planet search program. Our exposure times are set to avoid surpassing 50% of our detector's full well in order to minimize the nonlinearity effect, and our nonlinearity measurements are used to correct for the remainder of this effect. After these corrections we see no evidence that nonlinearity plays a significant role in our photometric performance at the level required for transit searching. We also correct for varying exposure time across our field of view due to shutter travel time. Due to the low exposure times needed to measure this effect, we measure the exposure time correction at low exposure times with a series of short dome flats and then measure the shutter pattern with a series of twilight flats. Using twilight flats reduces additional error from linearity correction when deriving the shutter pattern. We find the linearity correction and fringing pattern to be stable. During the summer monsoon, which occurs each year in August, data acquisition is halted and the telescopes are shut down. This time is used to perform maintenance activities on the telescopes.

We measure stellar positions using a method similar to that of Irwin (1985). We estimate local sky background by binning each image into 64×64 pixel blocks, and measure the peak of the histogram of the intensity of these pixels. We then interpolate this lower-resolution map to measure the background level anywhere in the image. Stellar locations are measured using intensity weighted first moments (the centroid of the star), and the total flux is measured using an 8 pixel ($\approx$ 6.2 arcsec) aperture radius in an effort to closely match the measurements done by the ongoing Landolt standard stars project (see: Landolt 2013 and references therein). Pixels that lie partially within this circular aperture are weighted according to the fraction of that pixel that lies within the ideal circular aperture. Sky background is estimated with a sky annulus between 24 and 32 pixels (18.6 - 24.8 arcsec) away from the stellar photocenter. We also adopt an aperture correction (Stetson 1990) in order to correct for the flux that falls outside of our aperture. The typical size of this correction is 0.04 mag.

The MEarth-North target list consists of 1844 nearby M dwarfs selected from Lépine (2005), a subset of the LSPM-North catalog (Lépine & Shara 2005) believed to be within 33 pc of the Sun and with stellar radius $R < 0.33R_\odot$ (Nutzman & Charbonneau 2008). These targets are uniformly distributed across the northern sky ($\delta > 0^\circ$) such that typically only one target exists in the MEarth $26'$x $26'$ field of view, with the exception of multiple systems and occasional unrelated asterisms. Each field is targeted individually, and is selected to contain sufficient comparison stars to obtain high precision relative photometry and astrometry.

For each observing season (September through July), MEarth gathers data at two different cadences. All targets are observed at approximately 10 day intervals (when they are visible) as part of the MEarth astrometric program, for which we recently published trigonometric parallaxes to a majority of our targets (Dittmann et al. 2014a). These observations take place at a variety of air masses, depending on when the scheduler can fit an observation between planet search target observations. For nights where the object is visible on both sides of the meridian, we sometimes schedule two astrometric data points in one night in order to resolve degeneracies in our parallax model (see Dittmann et al. 2014a for details regarding our astrometric reduction pipeline).

A subset of these targets is selected for our planet search campaign, and is observed each night. Within that night, our planet search targets are observed at a 20-30 minute cadence, ensuring that we obtain at least two in-transit data points for a typical one hour duration transit. Because we are monitoring these stars for planets, observations are taken at many different airmasses throughout the night. We discuss how we take advantage of this for our photometric analysis in section 3.3. For the results presented here, we have utilized all of the MEarth data taken at both astrometric and planet search cadence.

In addition to our target observations, each night we observe Landolt standard star fields (Landolt 1992, 2009, 2013; Clem & Landolt 2013). We typically observe 3-4 standard star fields per telescope in a given night and each field is observed only once in any given night in order to minimize its impact on the main survey (we explain how we mitigate the effects of color in our calibrated photometry despite these observational constraints later in this chapter). Standard fields tend to be taken at the beginning of the night, and at higher airmass than target observations. We show a histogram of the airmass for all standard field observations across all telescopes in Figure 3.1. The absence of observations at low airmass is due to the difference in latitude and declination between our observatory and the equatorial standard star fields. The secondary peak at an airmass of 1.3 is a feature of our scheduling system. To avoid exclusively taking

Landolt standard observations at high airmass, we use a zenith distance threshold for fields that are up for significant portions of the night to prefer lower air masses. Aside from this, it is readily apparent that while we obtain observations of standard star fields at all air masses, the distribution of observed air masses does not reflect the relative amount of time that any given standard field is visible at that airmass. However, we do not believe that this has any significant effects on our derived photometry.

3.3 Analysis

All data (long cadence, calibration fields, and short cadence) were reduced using the MEarth data reduction pipeline (see Berta et al. 2012a for an in-depth description of the MEarth data reduction procedure). In order to calibrate MEarth's measured photometry onto an absolute scale, we must make corrections for the effects of the atmosphere and light loss in the telescope. These effects are both color dependent and airmass dependent. We adopt the following model:

$$m_{*,MEarth} = z_i - 2.5\log_{10}(f_{obs}/t_{exp}) - \mathrm{AC} - \Big(k_{1,i} + k_{2,i}(m_{*,MEarth} - m_{*,K})\Big) \times (X-1) \quad (3.1)$$

where $m_{*,MEarth}$ is the magnitude of the star in the $MEarth$ band, $m_{*,K}$ is the magnitude of the star in the 2MASS K_s band, z_i is the zero point of the telescope, f_{obs} is the observed flux (in counts) for the star, t_{exp} is the exposure time of the image, AC is the aperture correction for the image, k_1 and k_2 are fitted coefficients to correct for airmass and color effects, respectively, and X is the airmass of the object. i denotes the night that the observation was taken.

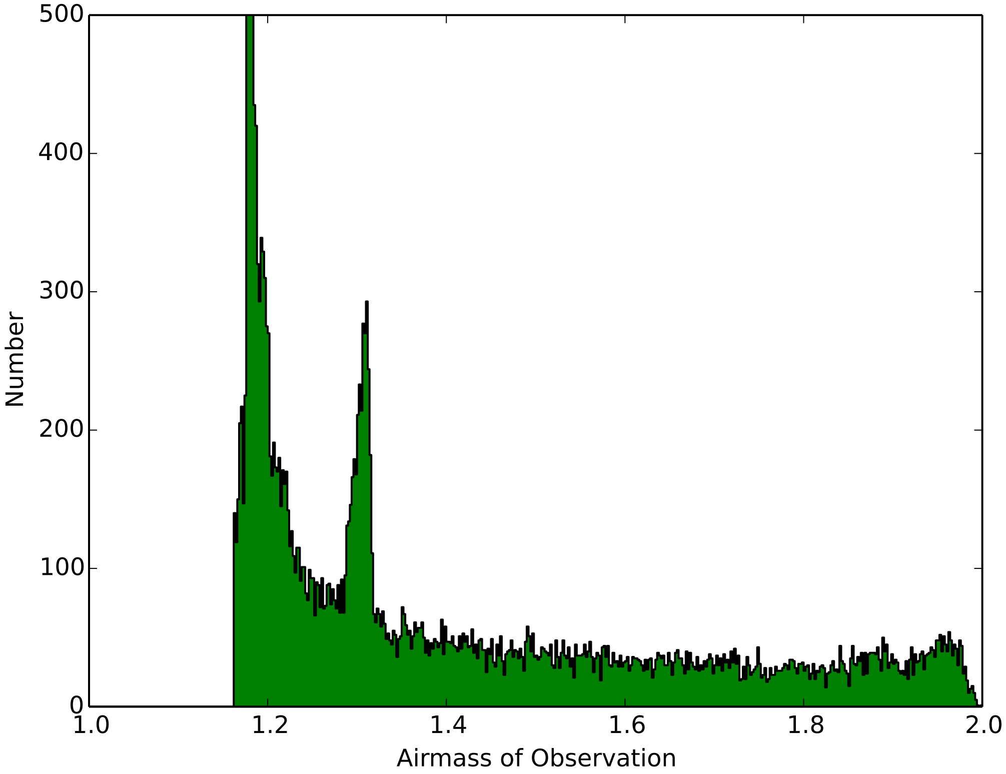

Figure 3.1: Histogram of the observed air masses for all of the Landolt standard fields observed across all telescopes during the course of the survey. The distribution is very non-uniform and does not reflect the time each standard field spends at any given airmass. The dearth of observations at low airmass is due to the latitude difference between Mt. Hopkins, Arizona and the Landolt equatorial standard fields observed in our program. Our scheduling program utilizes a zenith distance threshold to avoid exclusively observing Landolt fields at high airmass as soon as they rise, which creates the secondary peak in the histogram at 1.3 air masses.

While the standard field observations alone are too few in number on any given night to provide simultaneous constraints in k_1 and k_2, we utilize all the stars of sufficient brightness in every target field to also inform our fits. Traditionally, standard star fields are tracked across the sky and periodically revisited during the night, allowing multiple measurements of the same standard stars across a range of airmasses. However, because we are calibrating the *MEarth* photometric system itself, and utilizing *MEarth*-K_s color in our nightly fits, we can utilize *every* observed star with a unique 2MASS identifier to constrain the airmass and color coefficients of our fits. Due to the sheer number of these stars compared to the number of Landolt standards, these stars dominate the fit for these parameters in any given night. This method allows us to benefit from sampling a wide range of airmasses continually throughout the night rather than a handful of discrete pointings from the Landolt standard field observations. The zero point of each telescope, however, is uniquely constrained by the standard field observations. We use reference stars that are between *MEarth* magnitudes 9.0 and 13.0, which have sufficient signal to noise (S/N) ratios without being saturated in the image.

We fit our observations iteratively, first determining k_1 and k_2 for each individual night using all the data that were taken on that night, and then fitting for the zero point (z_i) of the telescope using solely the standard field observations. While our filter is different from the filters used by Landolt (1992, 2009, 2013) and Clem & Landolt (2013), we base our zero point correction to most closely match the Landolt I measurements for these stars at *MEarth*-K_s color = 0. We reduce the data from each telescope independently from the data from other telescopes, in order to avoid systematic color effects that may be present between the different telescopes. However, we have recently changed MEarth's observing strategy such that we observe target stars on two telescopes to increase our signal to noise per star and mitigate systematic effects in our search for small transiting extra-solar planets (Berta et al. 2013). For stars that have been observed in this mode, we are able to compare independent measurements of the broadband *MEarth* magnitude and assess possible systematic effects with our data (see section 3.3.1).

We remove non-photometric data by discarding a night if the standard deviation of the residuals across all images taken that night is greater than 0.02 magnitudes. After this cut, each telescope has between 100 and 200 photometric nights of data, depending on whether each telescope was operating or being repaired on any given night deemed to be photometric. On any photometric night, each telescope obtains approximately 10,000 individual measurements of stellar fluxes, across the M-dwarf target stars, comparison stars in the field, and the Landolt fields. In Table 3.2, we list the color and airmass coefficients as well as the zero points for each telescope on each night that was deemed photometric, while in Table 3.3 we list the *MEarth* magnitude determined for each Landolt standard star observed.

3.3.1 The *MEarth* optical magnitudes for 1802 M dwarfs

We apply our derived coefficients to all of our available data points for each MEarth target, estimating a *MEarth* band magnitude using equation 5.1. We report the *MEarth* magnitude as the median of all of our measurements across all photometric nights and all observing seasons. We estimate our error as the median absolute deviation (MAD) from this median value, and adjust it to 1 Gaussian σ by multiplying by 1.48 (Hoaglin et al. 1983). This method ensures that single erroneous data points, which

Table 3.2:: Nightly Photometric Coefficients (Equation 5.1) (Table Stub)

Date	Color Coefficient	Airmass Coefficient	Zero Point	Telescope
2011-10-13	0.0006	0.062	20.695	tel03
2011-10-13	0.0033	0.058	20.448	tel01
2011-10-14	-0.0040	0.066	20.512	tel04
2011-10-14	0.0002	0.068	20.699	tel07
2011-10-14	0.0050	0.048	20.515	tel05
2011-10-15	-0.0062	0.086	20.700	tel03
2011-10-15	-0.0049	0.081	20.744	tel08
2011-10-15	-0.0028	0.078	20.760	tel06
2011-10-15	-0.0013	0.075	20.430	tel01
2011-10-15	-0.0007	0.086	20.699	tel02
...	...	...	...	..

This table is available in its entirety in machine-readable form online.

Table 3.3:: *MEarth* Magnitudes of Landolt Standards (Table Stub)

Landolt Star	m_{MEarth}	err
SA92 263	10.703	0.033
SA92 348	11.443	0.032
SA92 409	9.264	0.036
SA92 342	11.096	0.031
SA92 335	11.809	0.032
SA92 253	12.762	0.035
SA92 250	12.363	0.035
SA92 245	11.982	0.037
SA95 43	10.179	0.034
SA95 41	12.866	0.036
...	...	...

This table is available in its entirety in machine-readable form online.

could be contaminated from cosmic rays in the image, flares from the M-dwarf itself, or other reasons from significant skewing our measurement. We note that for some of our stars the reported uncertainty in the *MEarth* magnitude is greater than the standard deviation required for any individual night to be considered photometric in our analysis. This is likely an astrophysical effect, as many M-dwarfs stars are variable in time due to stellar activity and rotation (starspots rotating in and out of view Irwin et al. 2011a), and we do not consider this to be an indication of significant systematic errors associated with our measurements.

The median uncertainty in our *MEarth* magnitudes is 0.015 mag, or 1.5%. We show a histogram of these errors in Figure 3.2. A small number of our targets have errors bars significantly larger than this typical value. 143 of 1802 stars have a error bar greater than 0.03 magnitudes, and 9 stars have an error greater than 0.05 magnitudes. Extremely large uncertainties are typically due to contamination of our target flux with that of a brighter companion. We indicate whether a star may be potentially contaminated in Table 3.4 (see below). We remove blended stars which we believe to be so significantly blended from a particularly close and bright companion that we do not believe our measurements accurately reflect either the combined magnitude or the magnitude of one of the components.

MEarth has begun observing our target stars with two telescopes in order to increase our signal to noise and sensitivity to small planets (Berta et al. 2013). This change in survey strategy allows us to independently measure the *MEarth* magnitude of these stars and assess possible sources of systematic error in our absolute photometric calibration. 322 of our stars have measurements with multiple MEarth telescopes, and we show a histogram of the difference between these measurements in Figure 3.2. The

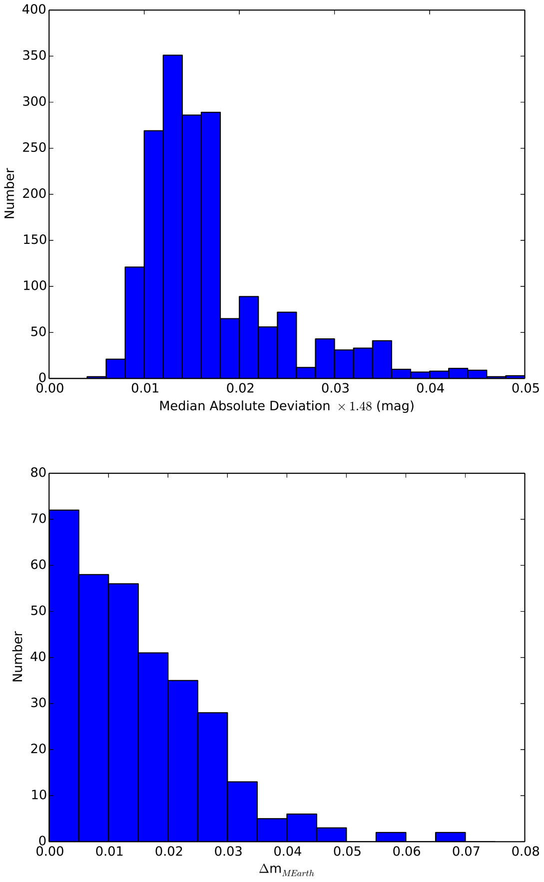

Figure 3.2: Top: Histogram of the internal errors of the *MEarth* magnitude for each target star. Typical errors are 0.015 magnitudes, and are derived from the absolute deviation from the median of all data points for the target star, adjusted to 1σ. Bottom: Histogram of the difference between the *MEarth* magnitude measured for 322 of our target stars that have measurements taken with multiple MEarth telescopes. The 68th percentile of the absolute difference between the magnitude measurements between telescopes for the same star is 0.018 magnitudes, approximately the typical error for stars with only single telescope measurements. Therefore, we do not believe that there are any significant systematic effects between telescopes and that they all are calibrated to the same magnitude system. The median number of data points a star has is 123, and less than 5% of our sample have fewer than 30 photometric observations.

68th percentile of the absolute difference between the magnitude measurement of the same star measured from different telescopes is 0.018 magnitudes, approximately the same as the internal error determined from individual telescopes. Therefore, we conclude that each MEarth telescope is calibrated to the same photometric system and that there are no additional uncertainties accrued by combining the magnitude measurements from multiple telescopes. We proceed with this assumption for the rest of this paper.

We list the optical magnitude of each star in Table 3.4. We also provide three blend flags to indicate whether the magnitude measured for this star may have significant contribution from either a binary companion, nearby bright star, or a star lying underneath the aperture for the target star. Our first blend flag indicates whether the aperture contains any additional stars other than the target star. This includes background objects as well as close common proper motion pairs. In many cases, this contamination is negligible, but we recommend assessing the importance of the contaminating flux using the MEarth finder charts available on the MEarth website[1]. Our second blend flag is for objects that have two individual entries in the LSPM-North catalog but are unresolved in the MEarth telescopes. Additionally, some of these objects are also unresolved in 2MASS. Our third blend flag indicates a known blended object that also has only a single entry in the LSPM-North catalog. For these sources, we also provide a reference. These sources include visual binaries split in guider-camera observations at IRTF as well as spectroscopic binaries and those identified via imaging. Finder charts include plate scans from the Digitized Sky Survey, which when combined with the high proper motion nature of our stars, allow us to see whether there is

---

[1] https://www.cfa.harvard.edu/MEarth/Welcome.html

significant contaminating stellar flux at the current position of the M dwarf.

3.3.2 A color-magnitude-metallicity relation anchored by spectroscopic measurements

Past studies have indicated that the locations of M-dwarfs on the (V-K_s) —M_K color magnitude diagram is significantly affected by the star's metallicity (Bonfils et al. 2005; Johnson & Apps 2009; Neves et al. 2012; Schlaufman & Laughlin 2010). Because an M-dwarf's absolute K_s band magnitude seems to be almost entirely determined by the star's mass (Delfosse et al. 2000), the metallicity dependence originates primarily in the optical magnitude of the star. The cooler temperature in these stars' atmospheres allow the formation of many molecules with broad (and overlapping) absorption bands that act to suppress the optical flux, creating this effect. By combining existing distance measurements and spectroscopic metallicity measurements with our $MEarth$ magnitude measurements, we can create a classical color-magnitude diagram using $MEarth$ as the optical component of the color.

In Figure 3.3, we plot the color-magnitude diagram for the 307 stars for which we have a trigonometric distance measurement and a near-infrared spectrum from Newton et al. (2014). For stars with multiple trigonometric distance determinations we utilize the observation with the lowest formal reported error bar instead of averaging all observations, in order to minimize combining systematic effects between individual surveys in the averaging process. Metallicity measurements based on the NIR spectra are taken from Newton et al. (2015a), who combined the metallicity calibrations of Mann et al. (2013a) for early type M-dwarfs and Mann et al. (2014) for later type M-dwarfs.

Table 3.4:: Observed Properties of the MEarth Targets (Table Stub)

2MASS ID	LSPM-N ID	m_{MEarth}	err	m_J	err	m_H	err	m_K	err
00011579+0659355	J0001+0659	13.038	0.013	11.286	0.022	10.741	0.028	10.418	0.021
00020623+0115360	J0002+0115	14.516	0.029	12.168	0.022	11.543	0.023	11.129	0.023
00074264+6022543	J0007+6022	10.335	0.012	8.911	0.021	8.332	0.024	8.046	0.02
00085391+2050252	J0008+2050	10.391	0.012	8.87	0.027	8.264	0.031	8.01	0.024
00085512+4918561	J0008+4918	12.636	0.017	10.864	0.022	10.32	0.021	9.98	0.018
00113182+5908400	J0011+5908	11.727	0.015	9.945	0.023	9.393	0.026	9.093	0.021
00115302+2259047	J0011+2259	10.267	0.011	8.862	0.021	8.308	0.036	7.987	0.021
00125716+5059173	J0012+5059	13.177	0.021	11.406	0.022	10.818	0.027	10.517	0.022
00131578+6919372	J0013+6919	9.858	0.013	8.556	0.024	7.984	0.02	7.746	0.02
00133880+8039569	J0013+8039W	8.971	0.031	7.756	0.034	7.131	0.047	6.904	0.02
...	...	...	...	...	...	...	...	...	...

Trigonometric Parallaxes are taken from Benedict et al. (2000); Makarov et al. (2007); Monet et al. (1992); Lépine et al. (2009); Anglada-Escudé et al. (2013b); van Leeuwen (2007d); Dittmann et al. (2014a); Dahn et al. (2002); Gatewood (2008); Harrington et al. (1993); Benedict et al. (1999); Riedel et al. (2014); Gatewood & Coban (2009); Riedel et al. (2010); Shkolnik et al. (2012); van Altena et al. (1995); Reid et al. (2003a); Khrutskaya et al. (2010); Henry et al. (2006); Smart et al. (2010, 2007)

Table 3.4 stub (Continued)

π ($''$)	err	Source	Spectral Type	Source	[Fe/H] (spec)	err	
0.057	0.0026	Dittmann et al. (2014a)	–	–	-0.083	0.12	
0.059	0.0047	Dittmann et al. (2014a)	M9	West et al. (2011a)	–	–	
0.069	0.002	Dittmann et al. (2014a)	M3.8	Shkolnik et al. (2009)	–	–	
0.054	0.00135	Riedel et al. (2014)	M5	Gaidos et al. (2014)	0.12	0.12	
–	–	–	M5.5	Reid et al. (2003b)	–	–	
0.108	0.00052	Gatewood & Coban (2009)	M5.5	Alonso-Floriano et al. (2015)	–	–	
0.060	0.0018	Dittmann et al. (2014a)	M3.5	Shkolnik et al. (2009)	–	–	
0.038	0.0031	Dittmann et al. (2014a)	M6.4	Shkolnik et al. (2009)	–	–	
0.053	0.0029	Dittmann et al. (2014a)	M 3	Reid et al. (1995)	–	–	
0.051	0.00175	van Leeuwen (2007d)	M1.5	Alonso-Floriano et al. (2015)	–	–	
...	...	...	...	...	...	...	...

Spectral types are taken from Lépine et al. (2003); Gizis et al. (2000a); Kirkpatrick et al. (2000); Reid et al. (2004a); Cruz & Reid (2002); Kirkpatrick et al. (1991); Gizis (1997); West et al. (2011a); Riaz et al. (2006); Landolt (2009); Lépine et al. (2002b); Cruz et al. (2007); Gizis et al. (2000b); Reid et al. (2007); Bessell (1991); Reid et al. (2008); Riedel et al. (2010); Gizis & Reid (1997); Henry et al. (2002); Bochanski et al. (2005); Gaidos et al. (2014); Henry et al. (1994); Reid et al. (2003b); Mann et al. (2013b); Zickgraf et al. (2005); Cruz et al. (2003); Shkolnik et al. (2010); Reid et al. (1995); Kirkpatrick et al. (1995); Henry et al. (2004, 2006); Lépine et al. (2002a, 2013a); Kirkpatrick et al. (1997); Reid et al. (2002); Martin & Kun (1996); Shkolnik et al. (2009); Reid & Gizis (2005); Scholz et al. (2005); Alonso-Floriano et al. (2015)

Table 3.4 stub (Continued)

[Fe/H] (photo)	Distance Modulus (m-M)	Blend Flag 1	Blend Flag 2	Blend Flag 3	Source
-0.209	–	0	0	0	–
0.012	–	0	0	0	–
0.053	–	1	0	1	Janson et al. (2014)
0.300	–	0	0	1	Beuzit et al. (2004a)
–	0.921	0	0	0	–
-0.232	–	1	0	0	–
0.140	–	0	0	0	–
0.112	–	0	0	0	–
-0.046	–	0	0	1	Mason et al. (2001)
-0.032	–	0	0	0	–
...	...	...	...	...	

Blend Flag 3 are taken from Benedict et al. (2000); Deshpande et al. (2013); Daemgen et al. (2007); Worley (1960); Janson et al. (2014); Gizis (1998); Bowler et al. (2015); Harrington & Dahn (1984); Close et al. (2003); McCarthy et al. (2001); Irwin et al. (2011b); Henry et al. (1997); Stauffer et al. (1997); Forveille et al. (2005); Kuiper (1936); Reid et al. (2001); Beuzit et al. (2004b); Bonfils et al. (2013); Dahn et al. (1976); Perryman et al. (1997); Shkolnik et al. (2010); Montagnier et al. (2006); Hartman et al. (2011a); Pravdo et al. (2004); Ireland et al. (2008); Law et al. (2006); Henry et al. (1999b); Gizis & Reid (1996); Delfosse et al. (1999); Law et al. (2008); Janson et al. (2012b); Mason et al. (2001); Irwin et al. (2009b); Pravdo et al. (2005); Jenkins et al. (2009); Pravdo et al. (2006) as well as IRTF, MEarth, and SDSS images.

Table 3.4 stub (Continued)

First datapoint (JD)	Last datapoint (JD)	N data points	Over-luminous?
2455858.794	2456838.905	24	0
2455867.658	2456822.961	23	0
2455848.728	2456702.623	517	0
2455850.702	2456836.954	91	0
2455857.730	2456830.888	27	0
2455874.621	2456834.960	105	0
2455850.741	2456836.886	417	0
2455851.675	2456836.958	76	0
2455855.821	2456834.922	278	0
2455857.770	2456839.899	36	0
...	...	...	...

This table is available in its entirety in machine-readable form online.

The more metal rich stars at a given M_K are redder than those that are more metal poor, as has been noted in previous studies (Bonfils et al. 2005; Neves et al. 2012; Schlaufman & Laughlin 2010). We have fit a smoothed two-dimensional (2D) spline to these data using the method described by Dierckx (1981) and show the [Fe/H] = 0 main sequence in Figures 3.3 and 3.4. Color-magnitude main sequences at the mean solar neighborhood metallicity of [Fe/H] = -0.1 and at solar metallicity ([Fe/H] = 0.0) are available in Table 3.5.

The dispersion in metallicity from this interpolation is 0.11 dex, equal to the precision derived from the spectroscopic measures themselves. We note that as this method is calibrated to existing infrared spectroscopic metallicity determinations, it inherits any systematic errors associated with those measurements. We find no significant systematic trend with the absolute K-band magnitude of the star or with the $MEarth$-K_s color of the star. We note that the majority of our sample lies between $M_K = 6.5$ and $M_K = 9.0$ (between $0.36M_\odot$ and $0.11M_\odot$ using Delfosse et al. 2000). Therefore, this is the domain over which our results are the most robust and well-constrained. The higher mass M dwarfs included in the calibration are mostly stars that had inaccurate optical colors and parameters that were inaccurately estimated, before we obtained trigonometric parallaxes for most of these targets. Our attempt to exclude these higher mass stars using the color-based estimates is likely to introduce a bias that systematically excludes bluer (more metal poor) stars for masses (as estimated using the more reliable M_K-based calibration) above $0.31M_\odot$. The MEarth sample also has few targets with $M_K > 9.0$. Therefore, the interpolation is not as strongly constrained in this regime. While we report metallicity estimates for stars in these magnitude ranges, they should be treated with more caution than the results reported for stars with $6.5 \leq M_K \leq 9.0$. We present

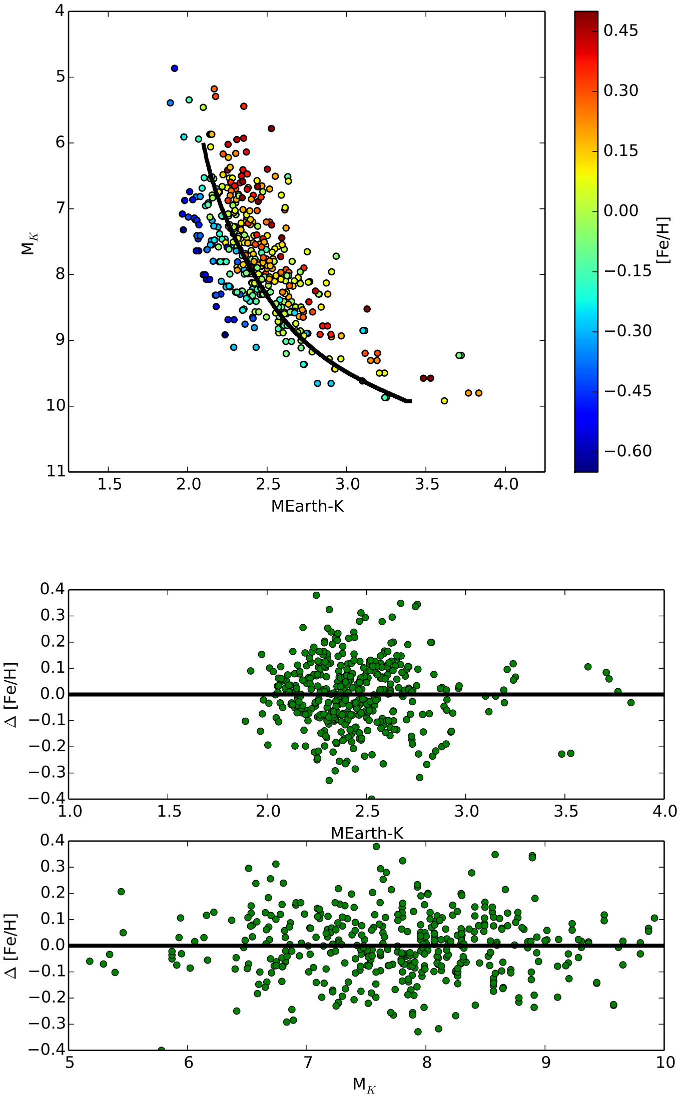

Figure 3.3: Top: Absolute K band magnitude vs $MEarth$-K_s color for 307 stars that have a trigonometric parallax and an infrared spectroscopic measurement. The color scale is the infrared spectroscopic measurement. While M_K is an excellent mass indicator (Delfosse et al. 2000), we find that the $MEarth$-K_s color of an M dwarf is correlated with the metallicity of the object. Increased metallicity results in a redder color due to line blanketing at optical wavelengths. The black line is our interpolated main sequence at [Fe/H] = 0.0.
Bottom: Residuals in our 2 dimensional metallicity interpolation as a function of $MEarth$-K_s color and M_K. We find no significant systematic trends. The standard deviation of our 2D interpolation is 0.11 dex, comparable in precision to the infrared spectroscopic metallicity indicators.

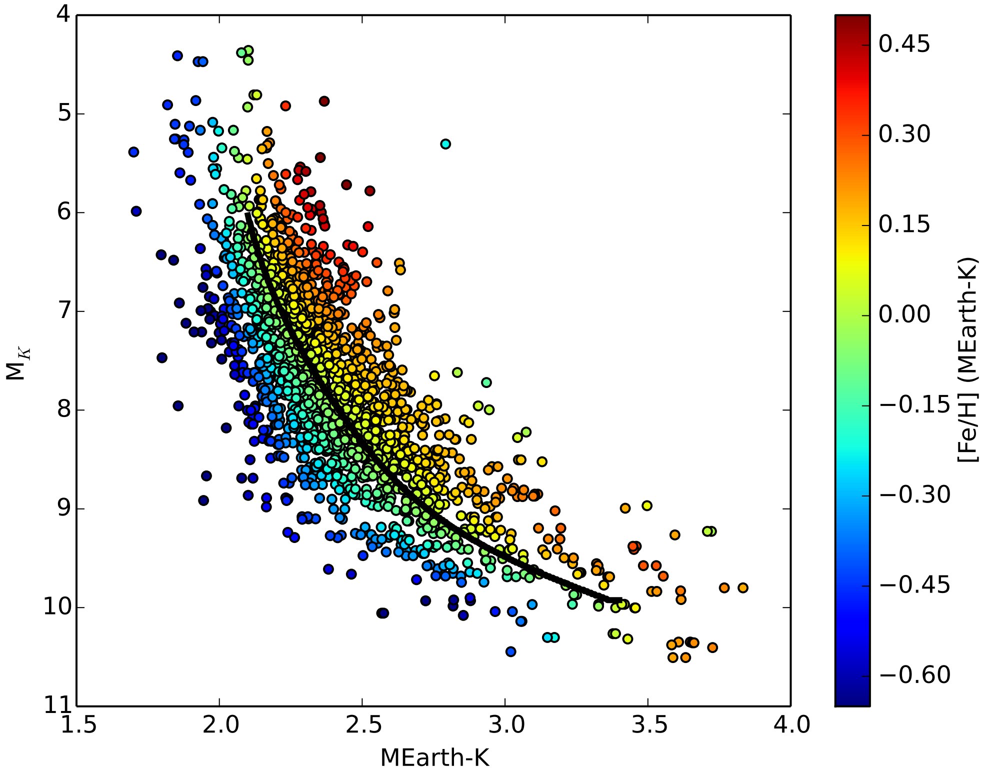

Figure 3.4: Same as for the top panel Figure 3.3 but for the entire MEarth sample and utilizing our 2-dimensional photometric metallicity interpolation instead of independent spectroscopic metallicity results. The black line is a solar metallicity main sequence. Our work increases the number of nearby M dwarfs with metallicity estimates, and provides a statistically significant sample measured in a uniform manner.

Table 3.5:: Color-Magnitude Sequence at [Fe/H] = -0.1 and [Fe/H] = 0.0 (Table Stub)

$m_{MEarth} - m_K$	$M_K([Fe/H] = -0.1)$	$M_K([Fe/H] = 0.0)$
2.100	6.452	5.992
2.103	6.487	6.028
2.105	6.487	6.063
2.108	6.523	6.098
2.110	6.558	6.134
2.113	6.558	6.169
2.116	6.593	6.205
2.118	6.629	6.240
2.123	6.664	6.275
2.126	6.664	6.311
...	...	...

This table is available in its entirety in machine-readable form online.

our metallicity estimates, along with our optical magnitude measurements, for our full sample in Table 3.4. There are 277 stars in our sample that do not have a trigonometric distance estimate. For these stars, we fix the star's metallicity at [Fe/H] = -0.1 and provide an estimate of the distance modulus $(m - M)$ of the star.

We show the color-magnitude diagram for all MEarth targets with a determined magnitude and trigonometric parallax, using the metallicities inferred from our relation, in Figure 3.4. We note that 29 stars are much redder than what is expected from their absolute K-band magnitude and lie significantly outside the calibration range for our spline. This far from our calibrated sequence our calibration turns-over and our method assigns them unrealistically low metallicities. An unresolved equal-mass binary would be shifted upwards by 0.75 magnitudes in Figure 3.4. An unresolved binary of unequal mass will be shifted upwards (due to the extra luminosity) but also to redder colors (as the the average color of pair is shifted). Undoubtedly our sample must contain a significant number of unknown, unresolved binaries. We suggest that these redder or over luminous stars that lie outside of our interpolation regime may be unresolved multiples. For each star, if our metallicity interpolation predicts a higher metallicity for a hypothetical star at the same absolute magnitude but 0.25 magnitudes bluer, then we flag this as an over luminous source in Table 3.4.

There are 894 stars in our sample that have spectral types determined from optical spectra by various groups (see Table 3.4 for spectral types and sources). These spectral types are compiled from the literature and, in cases where there are more than one spectral type measurement, we prioritize spectral typing methods involving direct comparison to spectral standards (Lépine et al. 2013b). In some cases, the spectral type is derived from measurements of molecular band indices. We do not average spectral types from multiple sources, but use the spectral type from the highest priority source. We have investigated the evolution of the $MEarth$-K_s color of a star as a function of spectral types (see Figure 3.5). We find that a 4th order polynomial is sufficient to capture the evolution of the $MEarth$-K_s color through this spectral range. This polynomial is:

$$MEarth\text{-K}_s = (-4.5\times10^{-4})\times N^4+(6.5\times10^{-3})\times N^3-(3.2\times10^{-3})\times N^2+(3.6\times10^{-2})\times N+1.9 \tag{3.2}$$

where N is the numerical spectral type of the star, 0 being an M0 type star, 5 being equivalent to an M5.0, and 10 being an L0 dwarf.

While the $MEarth$-K_s color of a star is a good indicator of spectral type through mid-M spectral sequence, we find that for the earliest M dwarfs the $MEarth$-K_s color does not change substantially. Furthermore, the MEarth sample selection criteria are designed to eliminate early M stars from our sample. Early type M dwarfs that make it into our sample are likely to be systematically redder than typical stars of that spectral type, so that they may masquerade as later type stars when utilizing simple color cuts. Therefore, these stars may not be representative of early M stars in general, and we suggest caution when using this equation for spectral types earlier than M2. At the earliest spectral bins we also have a higher proportion of outliers. These may be systematically affected by contamination if they are close to another star or may be subject to higher systematics than the later spectral types that we are targeting in our observations (greater nonlinearity or saturation). These red outliers are LSPM J1204+7603 and LSPM J2307+1501. LSPM 1204+7603 is flagged as a potential blend

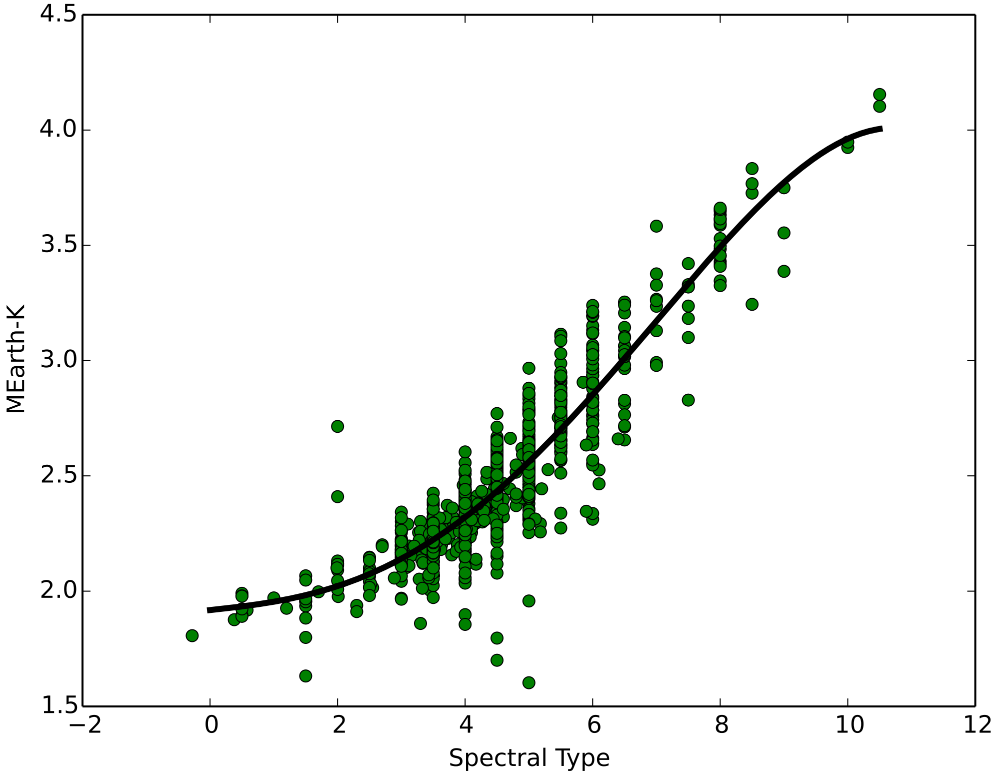

Figure 3.5: The *MEarth*-K_s color as a function of M dwarf spectral type with a third order polynomial fit through the sequence (shown as a black line). The star earlier than M0 is a late K dwarf while M10 and later begins the L dwarf sequence. All spectral types are taken from the literature and are not be determined in a strictly uniform manner. We find that the average *MEarth*-K_s color sequence continuously becomes redder for later spectral types although there is significant amount of variation due to metallicity, which this fit does not take into account.

with other background stars. We believe that this is the cause for this star being an outlier. The magnitude of LSPM 2307+1501 does not appear to be an outlier in our analysis. We suggest the reported spectral type may be incorrect.

3.4 Discussion

3.4.1 The metallicity of the solar neighborhood M dwarfs

We present a large sample of uniformly determined metallicity estimates for northern M dwarfs in the solar neighborhood. While the applicability of this technique is somewhat limited due to the non-standard nature of our bandpass and the requirement of an accurate distance measurement to the star, we can use the measurements for 1567 stars with trigonometric parallax measurements in order to investigate the nature of the nearby M dwarf population.

We restrict ourselves to a volume complete sample in the Northern hemisphere to avoid potential biases. Dittmann et al. (2014a) showed that the MEarth sample is nearly complete out to a distance of 20 parsecs within the color, estimated distance, and $R_{est} < 0.33R_{\odot}$ sample selection criteria of Nutzman & Charbonneau (2008). We will restrict ourselves to this volume for this analysis. While Dittmann et al. (2014a) corrected for the subsample of stars culled from the MEarth sample for being too bright for our survey or too close to a bright star, we do not make such a correction here as these missing stars do not have a *MEarth* magnitude. We do not believe that this will significantly affect our results because there are not many of these stars and they are likely to not be significantly biased in metallicity. Furthermore, the study in Dittmann et al. (2014a) divided the MEarth sample by spectral type, for which completeness can vary as a function of distance. Here we are studying the entire MEarth sample and therefore dilute the effect of a handful of known nearby stars being removed from the analysis.

In Figure 5.2 we show the metallicity distribution of M-dwarfs in the solar neighborhood within 20 parsecs of the Sun. The median value of these metallicities is $[\mathrm{Fe/H}] = -0.03 \pm 0.008$, approximately solar metallicity. The sharp drop beginning at $[\mathrm{Fe/H}] = 0.15$ is due to the saturation of the sodium line used in these metallicity measures (Newton et al. 2015a). Because our photometric metallicity calibration is based upon spectroscopic measurements derived from these lines, we may be subject to systematic errors at high metallicity. Therefore, this sharp drop off and lower proportion of stars at high metallicities may not be real, and the excess of stars between $[\mathrm{Fe/H}] = 0.10$ and $[\mathrm{Fe/H}] = 0.15$ is likely to be distributed across larger metallicities.

We avoid this potential source of systematic error by looking strictly at the relative proportion of stars in our sample that are metal poor (excluding the stars which were excluded for being outside of our calibration range). For this sample, 29 of the 565 of our stars within 20 parsecs have a metallicity of $[\mathrm{Fe/H}] = -0.5$ or less, approximately 5%. This is comparable to the proportion measured by Haywood (2001), who measured that 4% of their 383 solar neighborhood G dwarfs have a metallicity less than $[\mathrm{Fe/H}] = -0.5$. We cannot reject the null hypothesis that the local M-dwarfs are drawn from the same metallicity distribution of the local G-dwarfs based upon the fraction of metal poor stars. Therefore, they are likely derived from the same star formation history.

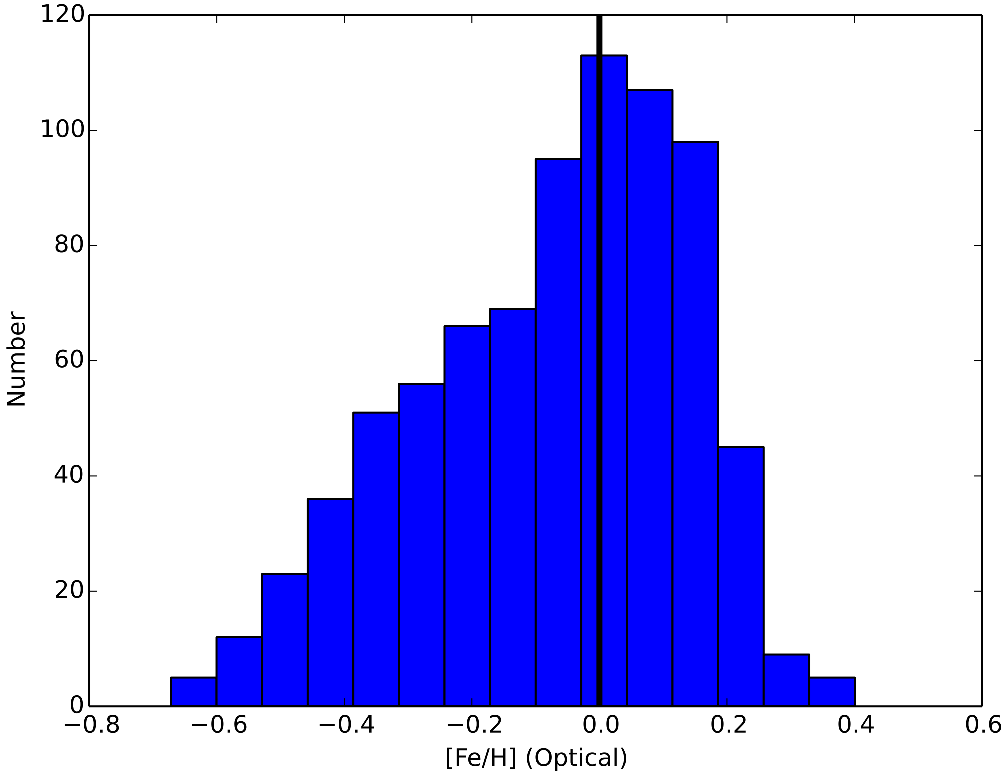

Figure 3.6: Histogram of the metallicities of the M dwarfs within 20 parsecs of the Sun in the MEarth sample. The black line at [Fe/H] = 0.0 is the value for the Sun. The median metallicity for these solar neighborhood M dwarfs is [Fe/H] = -0.03 ± 0.008, coincident with the solar metallicity. The asymmetric distribution of metallicities may be partially due to the saturation of lines at high metallicity in the spectroscopic sample used to calibrate our photometric relation. This saturation occurs around [Fe/H] ≈ 0.2. If so, then the true metallicity of stars shown here with [Fe/H] > 0.1 may be distributed out to higher metallicity. We find that the metallicity distribution of the solar neighborhood M dwarfs is similar to that of the solar neighborhood G dwarfs.

3.5 Conclusions

We have calibrated the *MEarth* photometric system using standard star observations taken routinely as part of general MEarth operations. By combing these results with trigonometric distance measurements and spectroscopically determined metallicity estimates from Newton et al. (2014, 2015a), we have calibrated a new color-magnitude-metallicity relation. The location of an M dwarf in M_K vs $MEarth$-K_s space is a metallicity indicator with comparable precision to infrared spectroscopic measurements, and we provide a photometric metallicity estimate for 1567 northern M dwarfs in the solar neighborhood with precisions of 0.1 dex. We find that the metallicity distribution and its median value are consistent with that of the nearby G dwarfs.

The nearby northern M dwarfs tabulated here are a promising hunting ground for ongoing planet searches like MEarth (Nutzman & Charbonneau 2008) and APACHE (Sozzetti et al. 2013), and also future surveys like CARMENES (Quirrenbach et al. 2012), the Habitable Planet Finder Spectrograph (Mahadevan et al. 2012), SPIROU (Reshetov et al. 2012), and EXTRA (X. Bonfils, personal communication). Planets found by these endeavors will allow us to investigate correlations between planet occurrence rate and stellar metal abundances. However, in order to do so, we need not only an accurate measure of M dwarf metal content, but also the capability to apply this uniformly on a statistically significant number of stars. The metallicities presented here offer a precision comparable to spectroscopic techniques, but the advantage of being applied over a much larger sample without the need of a significant investment in additional telescope time. Future improvements in this method will be made possible by GAIA[2], which is set to

---

[2] http://sci.esa.int/gaia/

provide unparalleled astrometric precision, allowing us to remove unresolved binaries and obtain much more precise absolute magnitudes for these objects.

Building on other studies, we have shown that an optical - infrared color is an excellent metallicity indicator. If a similar relation can be inferred for metallicity and distance in the Sloan (g',r',i',z') standard bandpasses, this would be a resource for future surveys like LSST, which is expected to uncover millions of M dwarfs. Towards this end, we have recently begun an effort to gather the necessary data on a subset of the stars presented here to explore this question. We plan to publish and release those data in a future publication.

Acknowledgments

We thank the anonymous referee for his or her insight and suggestions in reviewing this manuscript. E.R.N. was supported throughout this work by a National Science Foundation Graduate Research Fellowship and A.W.M. by the Harlan J. Smith Fellowship from the University of Texas at Austin. The MEarth Team gratefully acknowledges funding from the David and Lucille Packard Fellowship for Science and Engineering (awarded to D.C.). This material is based upon work supported by the National Science Foundation under grants AST-0807690, AST-1109468, and AST-1004488 (Alan T. Waterman Award). This publication was made possible through the support of a grant from the John Templeton Foundation. The opinions expressed in this publication are those of the authors and do not necessarily reflect the views of the John Templeton Foundation. This research has made use of data products from the Two Micron All Sky Survey, which is a joint project of the University of Massachusetts and the Infrared Processing and Analysis Center/California Institute of Technology, funded by NASA and the NSF. We acknowledge use of NASA's Astrophysics Data System (ADS), and the SIMBAD database, operated at CDS, Strasbourg, France. The MEarth team would also like to acknowledge Eric Mamajek who initially suggested for us to engage in this work. The authors of this paper would also like to thank Zachory Berta-Thompson, whose comments, suggestions, and extensive work with the MEarth observatory and data are invaluable.

Chapter 4

Discovery and Precise Characterization by the MEarth Project of LP 661-13, an Eclipsing Binary Consisting of Two Fully Convective Low-mass Stars

This thesis chapter will be submitted to The Astrophysical Journal

J. A. Dittmann, J. M. Irwin, D. Charbonneau, Z. K. Berta-Thompson, E. R. Newton, D. W. Latham, C. A. Latham, G. A. Esquerdo, P. Berlind, M. L. Calkins

Abstract

We report the detection of stellar eclipses in the LP 661-13 system. We present the discovery and characterization of this system, including high resolution spectroscopic radial velocities and a photometric solution spanning two observing seasons. LP 661-13 is a low mass binary system with an orbital period of $4.704364^{+0.000040}_{-0.000008}$ days at a distance of 24.9 ± 1.3 parsecs. LP 661-13A is a 0.3057 ± 0.0032 $M_\odot$ star while LP 661-13B is a 0.1937 ± 0.0014 $M_\odot$ star. The radius of each component is 0.3130 ± 0.0037 $R_\odot$ and 0.2159 ± 0.0061 $R_\odot$, respectively. We detect out of eclipse modulations at a period slightly shorter than the orbital period, implying that at least one of the components is not rotating synchronously. We find that each component is slightly inflated compared to stellar models, and that this cannot be reconciled through age or metallicity effects. As a nearby eclipsing binary system where both components are near or below the full-convection limit, LP 661-13 will be a valuable test of stellar models.

4.1 Introduction

The fundamental properties of low-mass stars remain a significant challenge for stellar structure models, despite their accuracy in the solar-mass regime (Torres 2013). The discrepancies between models and measurements become more pronounced below 0.35 solar masses (approximately spectral type M3.5 V), where these stars are thought to lose their radiative zones in their interior and become fully convective (Chabrier & Baraffe 1997; Baraffe et al. 2015).

The M dwarf spectral sequence spans a large range of mass, from 0.6 $M_\odot$ at the earliest spectral types down to the main sequence turn off at approximately 0.08 $M_\odot$. This mass range spans important transitions in the physical structure of the interior of these stars. Notably, these stars transition to the fully convective regime midway through the spectral sequence, at $0.35M_\odot$, and degeneracy pressure becomes increasingly important in the core (Chabrier & Baraffe 1997). These transitions must be accurately captured in stellar models and their effect on the equations of stellar structure must ultimately be reflected in the temperatures and radii of these stars.

Testing the mass-radius relation for low-mass stars is routinely done through the study of eclipsing binary (EB) systems. Precise radial velocity measurements taken throughout the orbit are sensitive to the component masses of the system, while measurements of the eclipse depths and shapes are sensitive to the radii of the eclipsing stars. The best-observed, detached, double-lined EBs can provide measurements accurate at the 1% level, allowing these systems to become strong tests of current stellar models (Torres et al. 2010).

One of the closest and most well studied eclipsing binary systems is CM Draconis (CM Dra). CM Dra is an eclipsing M dwarf binary at a distance of 14.5 parsecs from the Sun (Eggen & Sandage 1967; Lacy 1977). CM Dra also contains a white dwarf at a wide separation from the M dwarf pair. As instrumentation and modeling have improved, the masses and radii of the two M dwarfs are now measured at the 0.5% level (Metcalfe et al. 1996; Morales et al. 2009). Both stars in the CM Dra eclipsing binary are spectral type dM4.5 with masses of 0.23 and 0.21 solar masses and radii of 0.25 and 0.24 solar radii and orbit in a 1.7 day orbit (Morales et al. 2009). The radii of these stars are inflated at the $5\% - 7\%$ level (Morales et al. 2009), and this remains a problem even with the latest stellar models (Baraffe et al. 2015).

This problem is not restricted to a handful of systems. Taking only the most well-measured eclipsing binary systems in aggregate, low-mass stars tend to be *inflated* in radius and *cooler* in temperature than stellar models predict (Torres 2013). The number of low mass stars with stellar radii measured through interferometry is low (Boyajian et al. 2015), and often do not have any direct means to measure a precise mass. High precision measurements of stellar masses and radii for individual stars are obtained through measurements of eclipsing binary light curves and radial velocities (RVs). Photodynamical analyses of recently discovered triple systems (such as KOI-126, Carter et al. 2011a and Kepler-16 Doyle et al. 2011) allow even more accurate physical parameters measurements than classical eclipsing binaries due to the presence of eclipses between all three members of the system. However, since the eclipse probability and the probability of detection are strong functions of orbital separation, these systems tend to be dominated by close-in binaries. This makes them more susceptible to the effects of tidal forces between the stars and makes them likely to be tidally locked, preventing the stars from spinning down over their lifetime. This effect makes it more likely for these systems to be magnetically active and to remain significantly magnetically active over their main-sequence lifetimes. If magnetic activity can significantly affect the interior structure of low-mass stars, then this can create an observational bias in the observed radii of these stars, especially if these effects are not accounted for in models.

One way around this problem is to search for low-mass eclipsing binary systems that have sufficiently long periods that both stars essentially evolve as “single” stars, and collect enough high-quality data to constrain their physical parameters to sufficient accuracy to test existing stellar models. While difficult, several such systems have recently been discovered and characterized. The Kepler-16 system consists of a 41 day period eclipsing binary system orbited by a planet in a 229 day orbit, all exhibiting mutual occultations of each other (Doyle et al. 2011). The presence of both stellar occultations and planetary transits in this unique system allowed for extremely precise physical parameters of this system to be measured. The secondary star in the system is a 0.202 $\mathrm{M}_\odot$, 0.226 $\mathrm{R}_\odot$ star with a mass and radius measured with sub-1% precision. Our group has discovered a 41-day eclipsing binary, LSPM J1112+7626, consisting of two M-dwarfs. These stars have masses of $M_1 = 0.395$ $\mathrm{M}_\odot$ and $M_2 = 0.275$ $\mathrm{M}_\odot$ and radii of $R_1 = 0.382$ $\mathrm{R}_\odot$ and $R_2 = 0.300$ $\mathrm{R}_\odot$. In addition to these long period systems, several other eclipsing binary systems with low-mass stellar components have recently been found with periods in the 5-20 day range (Schwamb et al. 2013; Gómez Maqueo Chew et al. 2014; Zhou et al. 2015a). Some of the components in these systems show radii that are consistent with stellar models, while some show significant radius inflation. Assessing the cause of the radius inflation phenomenon in low mass stars requires the discovery of sufficient numbers of these systems with sufficiently different physical characteristics (orbital separation, metallicity, etc) as well as accurate determinations of the mass and radius of each component.

MEarth is an ongoing photometric survey of mid-to-late M dwarfs in the solar neighborhood (Distance, $D \lesssim 33$ pc), looking for low mass rocky planets whose periods may extend into the habitable zone of their star (Nutzman & Charbonneau 2008; Berta et al. 2013; Irwin et al. 2015). The MEarth-North array in Arizona has been in operation since 2008, and a copy located in Cerro Tololo, Chile has been in operation since early 2014. By virtue of being designed to be sensitive to small planets transiting these stars, MEarth is also highly sensitive to eclipsing binary systems.

Here we present the discovery of an eclipsing binary system revealed during the commissioning phase of the MEarth South array. This system shows out of eclipse modulations due to star spots which change between observing seasons. Through long-term out of eclipse monitoring, we are able to assess the impact that transient starspots have on our ability to measure the radii of each component, which in turn allows us to more reliably probe the physical parameters of this system and assess our errors. We utilize multiple eclipse measurements with the MEarth telescopes as well as radial velocity (RV) measurements in order to constrain the masses and radii of both components to high accuracy and test existing stellar models. In section 2, we detail the MEarth-South array, the discovery, and the follow-up observations of this system. In section 3, we present a joint analysis of the RV and photometric data and constrain the physical parameters of the system. In section 4, we discuss the implications of these measurements in regards to existing theoretical stellar models.

4.2 Observations

4.2.1 The MEarth-South Observatory

MEarth-South, like its Northern counterpart, consists of eight f/9 40 cm Ritchey-Chrétien telescopes on German equatorial mounts. The telescopes are located at Cerro-Tololo International Observatory (CTIO) in Chile (Irwin et al. 2015). The telescopes are automated and take data on every clear night. Each telescope contains a 2048 × 2048 pixel CCD with a pixel scale of approximately $0.84''$/ pixel. We utilize a Schott RG715 glass filter with an anti-reflection coating. For information about our filter curve and photometric system, see Dittmann et al. (2016). We expect that the MEarth-South photometric system is slightly different from the North, and that the results in Dittmann et al. (2016) might show minor differences with the Southern array. The MEarth-South CCDs are e2v CCD230-42 devices with a NIR optimized coating with fringe suppression. We operate the MEarth cameras at −30° C, and before each exposure we pre-flash the detector. This increases the dark current (which we subtract off), but it also eliminates persistence from the previous exposure.

We gather sky flat field frames at dawn and at dusk. Since MEarth uses German equatorial mounts, we must rotate the telescopes by 180 degrees relative to the sky when crossing the meridian. Therefore, we take two sets of flat fields, taking adjacent pairs of flat fields on opposite sides of the meridian. This procedure also allows us to average out large-scale illumination gradients from the Sun and the Moon. This scattered light also concentrates in our detectors in the center of the field of view. The amplitude of this scattered light effect is approximately 5% of the average value of the sky across the CCD. In order to correct for this, we filter out the large scale structure from our combined twilight flat field and use the residual flat field to track small scale features such as inter-pixel sensitivity and dust shadows on the detector. We derive the large scale flat field response from dithered photometry of dense star fields.

We measure the nonlinearity of the MEarth detectors using a dedicated sequence of dome flats. At all count levels, the MEarth CCDs have a slightly nonlinear conversion of photoelectrons to data number. This nonlinearity increases from 1%-2% at half the detector full well to 3%-4% near saturation. We correct for this effect as part of the general MEarth data reduction pipeline. Our exposure times are set to avoid surpassing 50% of the detector's full well in order to minimize this effect.

The MEarth-South target list is designed to be similar to the northern array's target list (Nutzman & Charbonneau 2008). MEarth-South observes a selection of nearby M dwarfs believed to be within 33 parsecs (pc) of the Sun and with a stellar radius $R < 0.33R_{\odot}$. The completeness of the target list and the number of targets with measured parallaxes is much lower in the South than in the North because the target list has been assembled from a much wider array of sources. No analogous compilation existed for the Southern hemisphere. For this reason, and also the availability of follow-up resources, the majority of our targets lie above $-30°$ DEC, rather than being distributed uniformly across the Southern sky ($\delta < 0°$). Typically there is only one target in each MEarth-South $26' \times 26'$ field of view, with the exception of wide multiple systems and occasional unrelated asterisms. Each field is targeted individually and is selected to contain sufficient comparison stars to obtain high precision relative photometry.

Each clear night MEarth observes a set of visible target stars at a cadence of approximately 20-30 minutes. This ensures that we obtain at least two in-transit data points for a typical one hour duration transit. If the real-time reduction software detects a potential transit (or eclipse) in-progress, standard cadence observations of other targets on that telescope are interrupted in order to perform high cadence follow-up of the potential event-in-progress (see Berta et al. 2013 for a description of the MEarth trigger). Normal operations are resumed when the event is deemed to be over or spurious and the flux from the star has returned to its normal level.

4.2.2 Initial Detection and Follow-up

A primary eclipse of LP 661-13 ($06^h56^m18^s.95$, $-08°35'46.1''$; alternate names NLTT 17194, 2MASS J06561894-0835461) was first discovered on 28 January 2014, on the second night of commissioning observations of the MEarth-South array (see Figure 4.1 for a finding chart for this system). Due to being in commissioning phase, the MEarth trigger was not yet being used. Therefore, only 6 in-eclipse data points were taken during the event. Subsequent eclipses were observed on the nights of February 16, 2014 (primary eclipse) and February 23, 2014 (secondary eclipse), and utilized the MEarth trigger. These events, combined with out-of-eclipse monitoring in the intervening nights, allowed us to unambiguously identify the orbital period as approximately 4.704 days. Armed with orbital period of the system, we began strategic targeting of radial velocity observations and subsequent eclipse measurements.

We obtained radial velocity measurements with the Tillinghast Reflector Echelle Spectrograph (TRES) on the 1.5 m Tillinghast reflector located at the Fred Lawrence Whipple Observatory (FLWO) on Mt. Hopkins, Arizona. We used the medium ($2.3''$) fiber, which yields a resolving power of $R = \frac{\Delta\lambda}{\lambda} = 44,000$. We obtained 14 observations of LP 661-13 with TRES, with 8 exposures taken in the 2014 observing season (18 February 2014 - 28 March 2014) and 6 taken in the 2015 observing season (27 December 2014 - 06 January 215). Total exposure times were 1 hour per observation, except for one exposure which was was 40 minutes. We obtained Thorium-Argon (ThAr) wavelength calibration exposures both before and after each science exposure. These wavelength calibration exposures were obtained with the same fiber as the one used to take the data on the target itself.

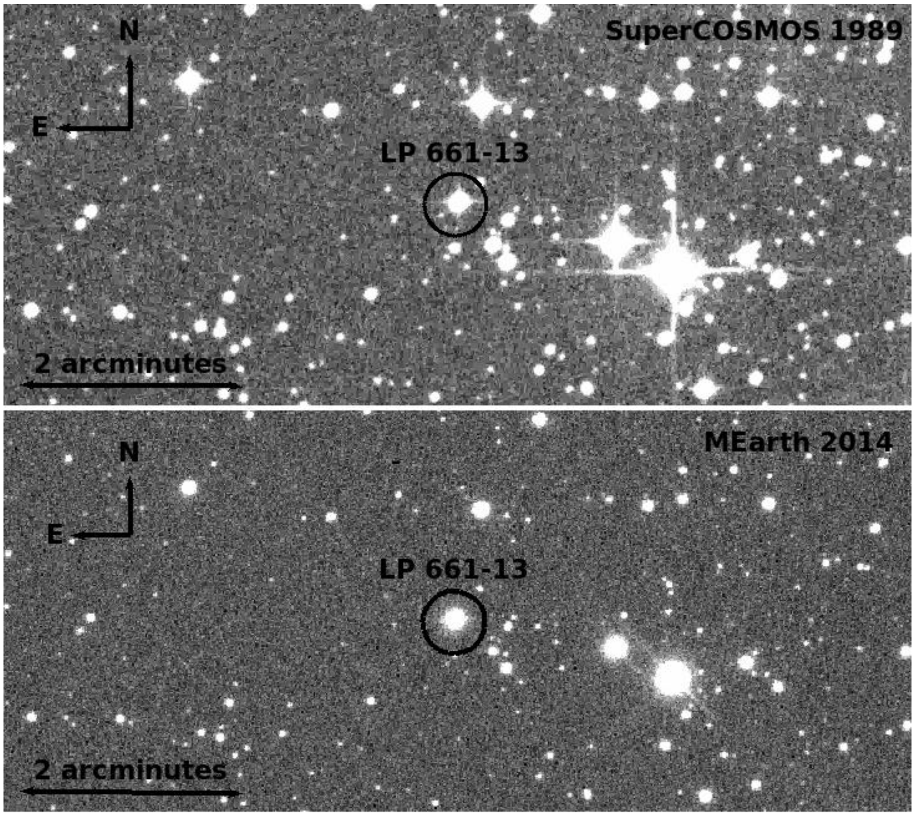

Figure 4.1: Finding chart for LP 661-13. The top image is archival data taken by the SuperCOSMOS survey from 1989. The bottom image is a MEarth image taken in 2014. The SuperCOSMOS image indicates that there is a faint background star that currently sits in the MEarth aperture for LP 661-13. We address this third light contamination later in the text.

Follow-up photometric observations of both primary and secondary eclipses were performed with the MEarth-South telescopes. We observed 11 unique eclipse events with 6 different telescopes. In addition to the observations of individual eclipses, we monitored the brightness of LP 661-13 out of eclipse on each clear night from CTIO in order to assess the variability of the system due to the stellar rotation of each component bringing star spots into and out of view. We have obtained 9173 individual observations of LP 661-13, with 5098 observations being in-eclipse measurements and 4075 out-of-eclipse measurements.

4.3 Analysis

4.3.1 Spectroscopy

We reduced our TRES spectroscopic data with standard IRAF[1] data reduction packages, using the procedure of Buchhave et al. (2010).Once these data are reduced, we use a two-dimensional cross correlation algorithm `TODCOR` (Zucker & Mazeh 1994), which uses user-given templates to match each component in the system, derive their radial velocities, and measure their light ratio in the observed spectral bandpass. For both components we used a single epoch observation of Barnard's star (GL 699) taken on 18 April 2011 as our template. Barnard's star has a spectral type of M4 (Kirkpatrick et al. 1991), and is suitable for both stars in this analysis. We also performed a reduction

---

[1] IRAF is distributed by the National Optical Astronomy Observatory, which is operated by the Association of Universities for Research in Astronomy, Inc., under cooperative agreement with the National Science Foundation

using the later type Wolf 359 as a template but found Barnard's star to yield more precise results. We correlated our spectra using the wavelength ranges of 7380-7500Å and 8500-8625Å (aperture numbers 43 and 49). These regions contain molecular features and the atomic calcium triplet, which produce strong correlations and are able to robustly identify both components in the spectrum.

For three of our observations, the velocities of the two stars are too similar to separate into distinct components with `TODCOR`. For these observations we measure only a single peak, which we assign as the radial velocity of solely the primary component. Once we obtained an initial solution for each epoch, we averaged the fitted light ratio for each epoch for which we could distinctly measure the cross-correlation peaks for each component. We then fixed the light ratio to this value and re-derived the best fit radial velocities for each component. We find a best fitting light ratio of $L_2/L_1 = 0.444 + / - 0.07$.

We report the radial velocities from this analysis in Table 4.1 and show a plot of the heliocentric radial velocities in Figure 4.2. We estimate the uncertainty of our velocities (based on the standard deviation of our residuals) as 0.26 km s^{-1} for the primary and 0.78 km s^{-1} for the secondary, and a heliocentric velocity for the system of 24.24 ± 0.07 km s^{-1} (see modeling section 4.4). In deriving these velocities, we assume a barycentric velocity for Barnard's Star of -110.47 km s^{-1}. Errors in this quantity (both systematic and white noise) would affect the final barycentric velocity of the LP 661-13 system, but are insignificant in deriving the system parameters.

Table 4.1:: TRES Radial Velocities for LP 661-13

Date (HJD)	v_1 (km s^{-1})	v_2 (km s^{-1})
2456706.6860	-14.47	86.76
2456709.6879	51.02	-18.27
2456738.6348	15.54	–
2456740.6439	15.22	–
2456741.6794	59.55	-30.71
2456742.6816	48.07	-13.27
2456743.6887	-0.63	62.44
2456744.6744	-10.73	80.24
2457018.8716	48.60	-13.92
2457019.8231	61.09	-34.30
2457020.8999	15.98	–
2457025.8228	4.94	55.33
2457026.8140	-13.15	83.67
2457028.8371	62.92	-36.23

4.3.2 Photometry

We measure stellar positions using a method similar to Irwin (1985). We estimate the local sky background by binning each image in 64 × 64 pixel blocks and measure the peak of the histogram of the intensity of these pixels. This lower-resolution map is then interpolated to measure the background level anywhere in the image. Sky background is estimated with a sky annulus between 18 and 24 pixels away from the stellar photo center. We measure stellar locations from the intensity weighted first moment (i.e. – the centroid) of the star.

We measure the total flux using an 6 pixel ($\approx 5.04''$) aperture radius. We weight pixels that lie partially within this circular aperture by the fraction of the pixel that lies within the ideal circular aperture. We also adopt an aperture correction to correct for the stellar flux that falls outside of our aperture. The typical size of an aperture correction is 0.04 magnitudes, but can vary from night to night depending on atmospheric conditions (predominantly seeing). In Table 4.2, we provide the corrected photometry for LP 661-13 across all telescopes and both seasons of data.

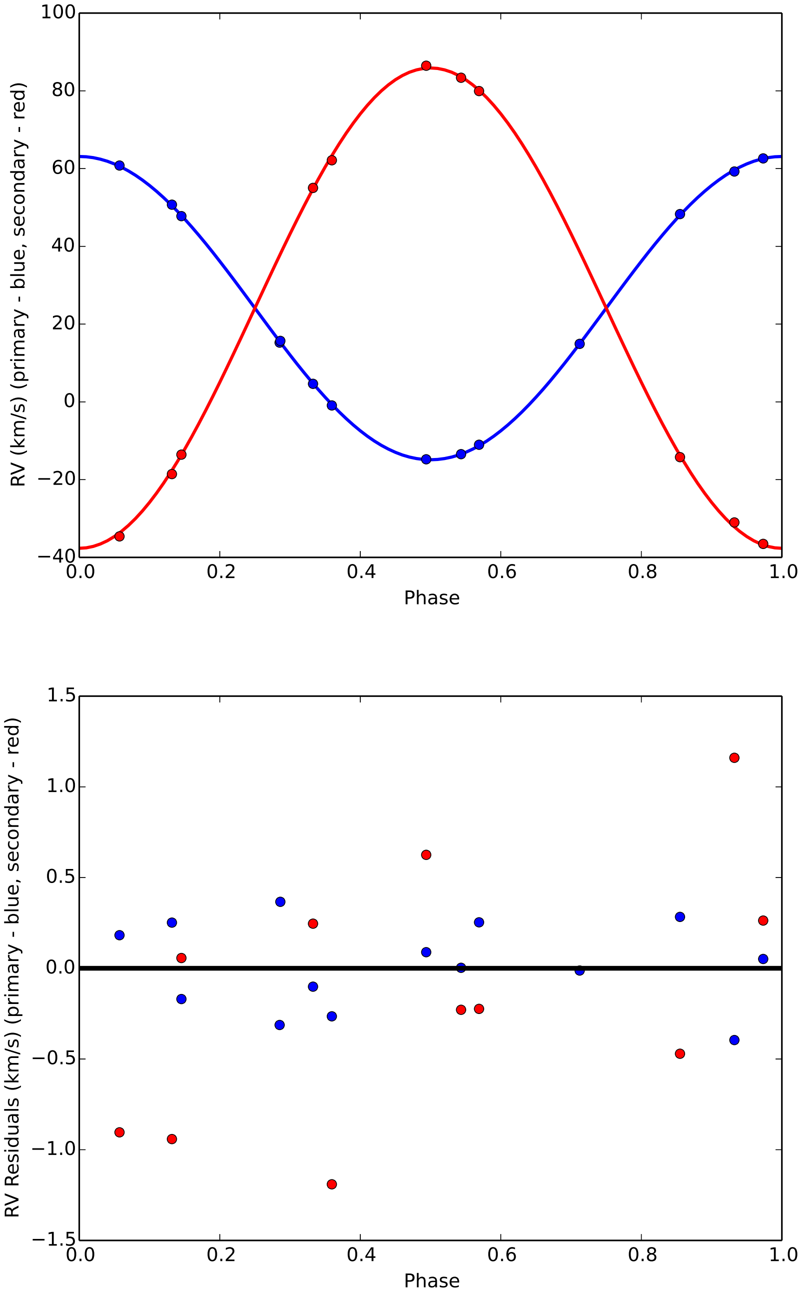

Figure 4.2: Top: Radial velocity signal from each component of LP 661-13. The primary component is in blue and the secondary component is in red. We find a primary mass of $M_1 = 0.3057 \pm 0.0032\ M_\odot$ and $M_2 = 0.1930 \pm 0.0014\ M_\odot$) orbiting with a period of P = $4.7043518^{+0.0000017}_{-0.0000014}$ days. Bottom: Residuals from the fit. We find an RMS precision of 0.26 km s^{-1} for the primary component and 0.78 km s^{-1} for the secondary component.

There is a marginal Roentgan Satellite (ROSAT) detection in the ROSAT faint source catalogue (Voges et al. 2000). The potential source has a count rate of $3 \pm 1 \times 10^{-2}$ counts per second. This corresponds to a flux density of approximately $1.70 \pm 0.56 \times 10^{-13}$ ergs cm^{-2} sec^{-1}. While this may be interesting to assess the significance of the X-ray emission with stellar activity and radius inflation, further X-ray data to confirm this potential detection are needed.

4.3.3 Astrometry

With two seasons of photometric data from the MEarth observatory, we are able to utilize the MEarth astrometric pipeline to measure the trigonometric distance to LP 661-13. The astrometric pipeline is described in detail in Dittmann et al. (2014b), but we summarize it here. We eliminate nights for which the full-width half-max for the image is greater than 5 pixels (approximately 3.5 arcseconds), or the average ellipticity of the target stars is greater than 0.5 (typically due to wind shake). We also eliminate images for which the pointing on the image is more than 15 pixels discrepant from the master MEarth image. We fit each image with a linear model in both the x and y coordinates, which allows for translation, rotation, shearing and pixel scale variations. We also include a separate constant offset between data taken on opposite sides of the meridian, to accommodate the image flip that results from the telescope's german equatorial mount.

We choose reference stars that lie within 600 pixels of the target star to avoid higher order effects at the edges of the CCD. We fit our astrometry iteratively, first fitting the linear plate model to each frame and then fitting for the proper motion and parallax of each star until convergence. Internal errors are estimated through a residual permutation. This provides the advantage that it preserves time-correlated noise in our error assessment but tends to be a weaker way to estimate errors for series with few data points. However, we have over 9000 data points and do not believe our astrometric error bars are underestimated.

We perform our astrometric analysis for only the telescope which has the largest number of data points over the largest time baseline. This time baseline ensures we can resolve any degeneracies between the proper motion and the parallax of the star. Using only one telescope eliminates possible systematics with combining data from multiple telescopes. Additionally, observations from other telescopes were targeted observations of eclipses and are of little use for astrometric analysis, which require data to be taken over the Earth's entire orbit. We show our astrometric time series in Figure 4.3, and measure a trigonometric parallax of $\pi = 40.2$ milliarcseconds (mas) with an internal error of 1.0 mas. However, since MEarth-South astrometry has not been benchmarked to a sample of stars with previously measured parallaxes (unlike MEarth-North), we inflate this error bar by a factor of 2 to be conservative. This corresponds to a distance of $D = 24.87 \pm 1.3$ parsecs (pc). We do not calculate a correction from relative parallax to absolute parallax, as this effect is smaller than our errors. We find proper motions of 75.1 ± 2.0 mas yr^{-1} in the RA direction and -227.3 ± 2.0 mas yr^{-1} in the DEC direction, where we have also inflated our internal error bars in the same manner as for the parallax amplitude. These values are consistent with the proper motion of 76.9 ± 5.5 max yr$^{-}1$ in the RA direction and -219.6 ± 5.5 max yr^{-1} previously reported by Salim & Gould (2003)

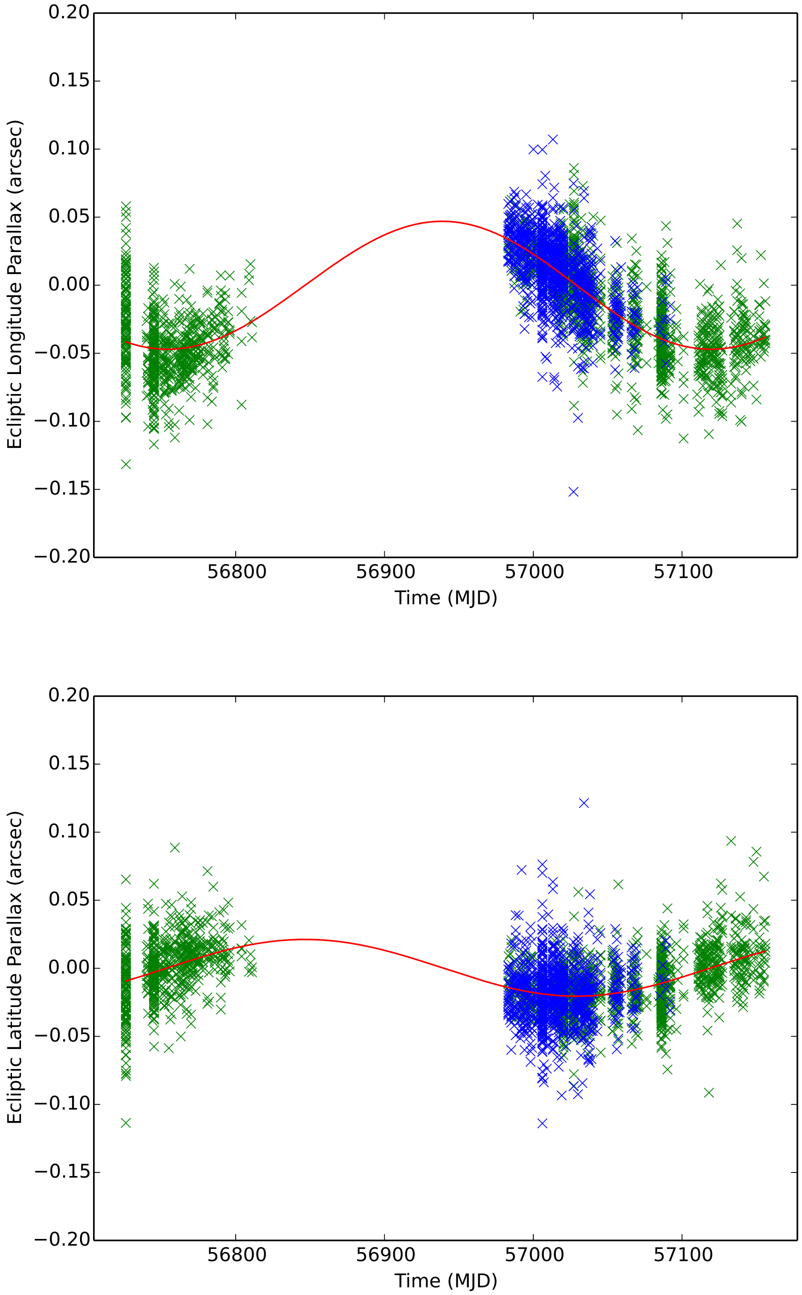

Figure 4.3: Trigonometric parallax signal from MEarth-South images in ecliptic longitude (left) and ecliptic latitude (right) for LP 661-13. We follow the procedure of Dittmann et al. (2014b), as MEarth-South and MEarth-North were built to be nearly-identical arrays. We find a parallax of $\pi = 40.2 \pm 2.0$ mas, which corresponds to a distance of 24.87 ± 1.3 parsecs.

4.4 System Modeling

We model this system following a similar procedure as Irwin et al. (2011b). While for LSPM J1112+7626 Irwin et al. (2011b) notes that the system is eccentric and therefore the photometric and spectroscopic solutions are highly interrelated, for LP 661-13 we find no detectable eccentricity, and so the analysis is made simpler. We model the system using the light curve generator from `JKTEBOP`[2] (Southworth et al. 2004; see Southworth 2013 for the most recent version). `JKTEBOP` is based on the eclipsing binary program `EBOP` (Popper & Etzel 1981). We use a modified version derived from Irwin et al. (2011b) which computes the integrals analytically using the method of Mandel & Agol (2002) and its erratum.

The out of eclipse light curve modulation indicates that there is significant spot activity on the surface of at least one component of the system, possibly both. This complicates the analysis as starspots have the capability of causing systematic errors in the measurement of the stellar radii as well as the surface brightness ratio of the two components, which is derived from the eclipse depths. Spots occulted during the eclipse reduce the observed depth of the eclipse relative to a non-spotted star, since a relatively dimmer portion of the star is being occulted. Conversely, the presence of non-occulted spots systematically increases the eclipse depth as the eclipse is preferentially obscuring brighter portions of the star. In reality, it is likely that both occulted and unocculted spots exist in any given eclipse. It is extremely difficult to infer the true spot distribution of a system, except in cases where eclipse deviations (i.e. spot crossing events) are readily distinguished in the light curve. Out of eclipse modulations can help assess spot

---

[2] See http://www.astro.keele.ac.uk/jkt/codes/jktebop.html for the original `JKTEBOP` code

coverage, but are sensitive to only asymmetric distribution of star spots. A uniformly spotted star would show no variation at all because a starspot rotating out of view would be replaced by an identical spot rotating into view. Identifying, or failing to identify, multiple frequencies in the out of eclipse modulations can also help determine whether the starspots are concentrated on one star or if both components display significant asymmetric spot coverage, although if only one period in the out-of-eclipse modulation is detected it is impossible to determine on which component the signal originates.

We adopt the spot model from Irwin et al. (2011b), which assumes that the out of eclipse modulations are solely due to starspots, and assumes a simple sinusoidal form for the modulations. The functional form for these modulations is:

$$\frac{\Delta L_i}{L_i} = a_i \sin\left(\frac{2\pi F_i t}{P}\right) + b_i \cos\left(\frac{2\pi F_i t}{P}\right) - \sqrt{a_i^2 + b_i^2} \tag{4.1}$$

where t is the time, L is the light from the star, i denotes each component of the system, a_i and b_i are the constants expressing the amplitude and the phase of the out-of-eclipse modulation, and F_i is the ratio of the rotational frequency of the star to the orbital frequency.

In the present case, we find only one significant period for the out of eclipse modulations. However, since the observed modulation has a period close to the orbital period of the system, it is possible that both stars have similar periods and that they are close to a tidal locking scenario. This means that we cannot be sure on which component the starspots originate, and we must account for this systematic uncertainty. Unfortunately, fitting a spot model on both components is degenerate, given the limited information available from a single modulation derived from total integrated light measurements. In order to assess the full range of possible physical parameters that are consistent with the data, we fit a series of models with different spot parameters, which we describe below.

We fit the photometric light curve (both in and out of eclipse) independently from the RV data. Because we do not detect an eccentricity in the system, the RV data and the photometric data are sensitive to independent system parameters. However, when we model the radial velocities of each component, we utilize the photometric solution for the orbital period, phase, and orbital inclination of the system. We assume that there is no third light in the system.

We fit two different models, one where there are starspots on only the primary component of the system, and one where the spots are concentrated on solely the secondary component of the system. We also fit the data from the 2014 season and the 2015 season independently, and allow the starspot modulation to change between seasons. Through this method, we aim to explore the possible effect that starspot contamination can have on our inference of the stellar radii. We explore this parameter space using the `emcee` code (Foreman-Mackey et al. 2013), which is a python implementation of the Affine Invariant Markov Chain Monte Carlo sampler. Each model is initiated with 100 walkers in a Gaussian ball located at an approximate solution. We run the chain for 2 million steps, and discard the first 200,000 steps to allow the solution to "burn-in". We use uninformative (unbound, uniform) priors for all of our model parameters, except for the limb darkening law. Quadratic limb darkening parameters are initiated with the model of Claret (2000) for each component utilizing an approximate temperature (T_{eff} = 3700K, log(g) = 5.0) and the *Cousins I* band filter. Each coefficient is allowed to vary freely, but not exceed a 10% deviation from this theoretical value. This allows the model to adjust for differences in the actual star compared to the theoretical parameters as well as for the slight differences between our bandpass and *Cousins I* without venturing into physically implausible parameter space. Letting the limb darkening parameters float in this way allows us to explore our prior, and we do not contend that our results are a physical measurement of the actual limb darkening parameters for these stars.

In Table 4.3 we list the physical parameters of our model (not including the normalizations for each telescope and each eclipse), and in Tables 4.4 and 4.5 we show the resulting best fit model and the 16th and 84th percentile (approximately 1σ) for each parameter for each season. We are able to fit our measured light curves equally well regardless on which star we place starspots. However, if we place the starspot signal on the secondary component, the out of eclipse model parameters vary significantly between observing seasons, whereas if the starspot signal is originating on the primary component, the parameters are stable between seasons. Particularly, F, the ratio between the orbital and rotational frequency has different values for each season if the secondary component is responsible for the star spot modulation signal. Since the rotation period of the star should not change (and the effect of differential rotation for star spots at different latitudes is small), we conclude that the starspot signal must be originating on the primary component and we will utilize the model for which starspots are located on the primary component for the rest of this paper. We note, however, that this choice does not significantly affect the values of the masses and radii of the components but does change the uncertainty. While the light curves themselves are most directly sensitive to the sum of the component radii and their ratio, with our data we are able to separate these two variables and measure the individual component radii themselves.

The base spottedness and the fraction of eclipsed spots model parameters are unconstrained by the data, and allowed to float to allow us to explore parameter space and assess our total uncertainty in our derived physical parameters. In order to assess possible systematic uncertainties associated with these model parameters, we also run MCMC chains holding these parameters fixed at 0.0, 0.25, 0.50, 0.75, and 1.0. We find that these parameters typically induce a 1.5% variation in the uncertainty of the radii of the component stars, and a negligible effect on the mass of the stars (which is primarily constrained with the RV data). While this systematic error is partially explored by letting these model parameters float in the chain, there will likely be some residual systematic error not captured in our MCMC runs.

For our final solution, we fit both seasons jointly, requiring the same physical parameters across seasons but allowing the starspot model to change (but not change components). We have also fixed the fraction of eclipsed spots (f_1) to 1.0 and the base spottedness of the star (f_2) to 0.0, as it would take unlikely spot distribution on the surface of the star to significantly change these parameters. See Irwin et al. (2011b) for a detailed investigation into the role that these parameters play in affecting measured masses, radii, and brightness temperatures. We also fix the orbital eccentricity at 0, as we see no evidence for orbital eccentricity in this system from our eclipse timings (e $< 4 \times 10^{-4}$, 95% confidence). In Table 4.6, we list the final model parameters for our joint fit of both seasons of data assuming starspots distributed on the primary component and in Table 4.7 we list the physical parameters, including component masses and radii, for the LP 661-13 system. In Figures 4.4 and 4.5 we show each individual primary and secondary eclipse as well as their residuals with this model.

Table 4.2:: MEarth Photometry for LP 661-13

Date (HJD)	Δ magnitude	error (mag)	telescope
2456705.52764	0.007709	0.001958	tel15
2456705.52824	0.011443	0.001956	tel15
2456705.53032	0.006192	0.001937	tel15
2456705.53092	0.004161	0.001935	tel15
2456705.53152	0.004771	0.001931	tel15
...	...	...	...

Table 4.3:: Model Parameters

Parameter	Value	Prior
J_{MEarth}	Varied	Uniform
$(R_1 + R_2)/a$	Varied	Uniform
R_2/R_1	Varied	Uniform
$\cos i$	Varied	Uniform (isotropic in i)
M_2/M_1	Varied	Uniform
$K_1 + K_2$	Varied	Uniform
$u_{1,1}$	Varied	Uniform $(0.2232 - 0.2728)$
$u_{1,2}$	Varied	Uniform $(0.5364 - 0.6556)$
$u_{2,1}$	Varied	Uniform $(0.4581 - 0.5599)$
$u_{2,2}$	Varied	Uniform $(0.3717 - 0.4543)$
β_1	0.32	...
β_2	0.32	...
L_3	0	...
F	Varied	Uniform
f_1	Varied (Fixed for final solution)	Uniform
f_2	Varied (Fixed for final solution)	Uniform
a	Varied	Uniform
b	Varied	Uniform
$e\mathrm{cos}\omega$	Varied (Fixed for final solution)	Uniform
$e\mathrm{sin}\omega$	Varied (Fixed for final solution)	Uniform
P	Varied	Uniform
T_0	Varied	Unfirom
γ	Varied	Uniform

Table 4.3 (Continued):

Description
Central surface brightness ratio (secondary/primary) in $MEarth$
Sum of the radius of each component divided by the semi major axis
Radius ratio
Cosine of the orbital inclination
Mass ratio
Sum of RV semi-amplitudes (km/s)
Linear limb-darkening coefficient for primary
Quadratic limb-darkening coefficient for primary
Linear limb-darkening coefficient for secondary
Quadratic limb-darkening coefficient for secondary
Gravity darkening exponent for primary
Gravity darkening exponent for secondary
Third light component divided by total system light
Ratio of rotational to orbital frequency
Fraction of spots eclipsed
Base spottedness of star
Out-of-eclipse sine coefficient
Out-of-eclipse cosine coefficient
Eccentricity times cosine of argument of periastron
Eccentricity times sine of argument of periastron
Orbital period of system (heliocentric) (days)
Epoch of primary eclipse (HJD - 2456600.0)
Systemic radial velocity of system (km/s)

Table 4.4:: Parameters for Model With Starspots on Primary Component

Parameter	2014 Season	2015 Season
J_{MEarth}	$0.8705^{+0.0298}_{-0.0268}$	$0.8698^{+0.0261}_{-0.0177}$
$(R_1+R_2)/a$	$0.0574^{+0.0007}_{-0.0008}$	$0.0574^{+0.0005}_{-0.0004}$
R_2/R_1	$0.6836^{+0.1065}_{-0.1539}$	$0.7500^{+0.0674}_{-0.0717}$
$\cos i$	$0.0425^{+0.0008}_{-0.0013}$	$0.0426^{+0.0005}_{-0.0006}$
M_2/M_1	$0.6314^{+0.0033}_{-0.0033}$	$0.6316^{+0.0033}_{-0.0035}$
K_1+K_2	$100.77^{+0.42}_{-0.42}$	$100.77^{+0.44}_{-0.41}$
$u_{1,1}$	$0.2474^{+0.0188}_{-0.0189}$	$0.2579^{+0.0105}_{-0.0269}$
$u_{1,2}$	$0.6102^{+0.0376}_{-0.0608}$	$0.6413^{+0.0105}_{-0.0218}$
$u_{2,1}$	$0.4901^{+0.0530}_{-0.0272}$	$0.4723^{+0.0305}_{-0.0116}$
$u_{2,2}$	$0.4123^{+0.0324}_{-0.0299}$	$0.4157^{+0.0292}_{-0.0306}$
F	$1.2288^{+0.0030}_{-0.0145}$	$1.2284^{+0.0039}_{-0.0160}$
f_1	$0.0684^{+0.2328}_{-0.0473}$	$0.0561^{+0.1512}_{-0.0353}$
f_2	$0.0157^{+0.0838}_{-0.0110}$	$0.0104^{+0.0212}_{-0.0070}$
a	$0.0009^{+0.0005}_{-0.0007}$	$0.00035^{+0.00026}_{-0.00035}$
b	$-0.0003^{+0.0003}_{-0.0002}$	$-0.00016^{+0.00027}_{-0.00023}$
$e\cos\omega$	$-0.00003^{+0.00003}_{-0.00006}$	$0.000000^{+0.000017}_{-0.000038}$
$e\sin\omega$	$-0.000003^{+0.000450}_{-0.000090}$	$-0.000003^{+0.000038}_{-0.000054}$
P	$4.704364^{+0.000040}_{-0.000008}$	$4.704360^{+0.000005}_{-0.000005}$
T_0	$105.5602^{+0.0001}_{-0.0006}$	$105.5598^{+0.0003}_{-0.0003}$
γ	$23.9313^{+0.0929}_{-0.0922}$	$23.9349^{+0.0897}_{-0.0949}$

Table 4.5:: Model Parameters for Starspots on Secondary Component

Parameter	2014 Season	2015 Season
J_{MEarth}	$0.9114^{+0.0453}_{-0.0294}$	$0.8729^{+0.0254}_{-0.0252}$
$(R_1 + R_2)/a$	$0.0580^{+0.0012}_{-0.0010}$	$0.0573^{+0.0006}_{-0.0006}$
R_2/R_1	$0.6894^{+0.1558}_{-0.0929}$	$0.7493^{+0.1297}_{-0.0722}$
$\cos i$	$0.0430^{+0.0015}_{-0.0014}$	$0.0424^{+0.0008}_{-0.0007}$
M_2/M_1	$0.6314^{+0.0046}_{-0.0053}$	$0.6319^{+0.0047}_{-0.0049}$
$K_1 + K_2$	$100.6848^{+0.4666}_{-0.3399}$	$100.8730^{+0.4660}_{-0.5094}$
$u_{1,1}$	$0.2393^{+0.0230}_{-0.0116}$	$0.2582^{+0.0100}_{-0.0167}$
$u_{1,2}$	$0.5777^{+0.0469}_{-0.0316}$	$0.6395^{+0.0122}_{-0.0361}$
$u_{2,1}$	$0.5048^{+0.0379}_{-0.0352}$	$0.4767^{+0.0406}_{-0.0156}$
$u_{2,2}$	$0.4034^{+0.0331}_{-0.0239}$	$0.3927^{+0.0357}_{-0.0161}$
F	$1.778^{+0.0102}_{-0.4461}$	$0.9098^{+0.2803}_{-0.0052}$
f_1	$0.0193^{+0.2414}_{-0.0182}$	$0.0023^{+0.0075}_{-0.0016}$
f_2	$0.0154^{+0.0850}_{-0.0144}$	$0.0024^{+0.0105}_{-0.0015}$
a	$0.0033^{+0.0019}_{-0.0032}$	$0.0017^{+0.0037}_{-0.0021}$
b	$0.0010^{+0.0006}_{-0.0009}$	$0.00010^{+0.0038}_{-0.0039}$
$e\mathrm{cos}\omega$	$-0.000058^{+0.000041}_{-0.000067}$	$-0.000055^{+0.000031}_{-0.000029}$
$e\mathrm{sin}\omega$	$-0.00000^{+0.00181}_{-0.00069}$	$0.000013^{+0.00012}_{-0.000029}$
P	$4.70438^{+0.00002}_{-0.00001}$	$4.704362^{+0.0000051}_{-0.0000052}$
T_0	$105.56034^{+0.00006}_{-0.00006}$	$105.55972^{+0.00033}_{-0.00034}$
γ	$23.9106^{+0.1143}_{-0.0924}$	$23.9136^{+0.09975}_{-0.1052}$

Table 4.6:: Joint Model Parameters^a

Parameter	Value (Prim. spots, $L_3 = 0$)	Value (Prim. spots, $L_3 = 0.01$)
$J_{\rm MEarth}$	$0.893^{+0.011}_{-0.027}$	$0.892^{+0.011}_{-0.020}$
$(R_1 + R_2)/a$	$0.05710^{+0.00044}_{-0.00043}$	$0.05706^{+0.00053}_{-0.00058}$
R_2/R_1	$0.673^{+0.032}_{-0.023}$	$0.672^{+0.041}_{-0.033}$
$\cos i$	$0.04200^{+0.00047}_{-0.00053}$	$0.04192^{+0.00049}_{-0.00072}$
M_2/M_1	$0.6314^{+0.0033}_{-0.0045}$	$0.6299^{+0.0035}_{-0.0039}$
$K_1 + K_2$	$100.76^{+0.54}_{-0.58}$	$101.15^{+0.53}_{-0.59}$
$u_{1,1}$	$0.2417^{+0.0087}_{-0.0086}$	$0.2413^{+0.0080}_{-0.0077}$
$u_{1,2}$	$0.593^{+0.038}_{-0.023}$	$0.577^{+0.022}_{-0.015}$
$u_{2,1}$	$0.507^{+0.012}_{-0.026}$	$0.510^{+0.012}_{-0.031}$
$u_{2,2}$	$0.414^{+0.020}_{-0.022}$	$0.410^{+0.010}_{-0.023}$
F (season 1)	$1.217^{+0.012}_{-0.015}$	$1.215^{+0.013}_{-0.021}$
f_1 (season 1)	1 (fixed)	1 (fixed)
f_2 (season 1)	0 (fixed)	0 (fixed)
a (season 1)	$0.001356^{+0.000126}_{-0.000029}$	$0.00140^{+0.00020}_{-0.00005}$
b (season 1)	$-0.000487^{+0.000063}_{-0.000020}$	$-0.000497^{+0.000017}_{-0.000032}$
F (season 2)	$1.23018^{+0.00092}_{-0.00071}$	$1.23043^{+0.00071}_{-0.00084}$
f_1 (season 2)	1 (fixed)	1 (fixed)
f_2 (season 2)	0 (fixed)	0 (fixed)
a (season 2)	$0.00112^{+0.00024}_{-0.00042}$	$0.00120^{+0.00015}_{-0.00043}$
b (season 2)	$-0.00044^{+0.00016}_{-0.00005}$	$-0.000484^{+0.000068}_{-0.000012}$
$e\cos\omega$	0 (fixed)	0 (fixed)
$e\sin\omega$	0 (fixed)	0 (fixed)
P	$4.7043505^{+0.0000017}_{-0.0000014}$	$4.7043510^{+0.0000016}_{-0.0000015}$
T_0	$105.560427^{+0.000063}_{-0.000082}$	$105.560376^{+0.000082}_{-0.000067}$
γ	$23.95^{+0.15}_{-0.14}$	$23.99^{+0.18}_{-0.16}$

Table 4.6 (Continued)

Value (Sec. spots, $L_3 = 0$)	Value (Sec. spots, $L_3 = 0.01$)
$0.891^{+0.015}_{-0.017}$	$0.893^{+0.010}_{-0.023}$
$0.05730^{+0.00035}_{-0.00031}$	$0.05697^{+0.00045}_{-0.00038}$
$0.679^{+0.033}_{-0.018}$	$0.675^{+0.027}_{-0.032}$
$0.04218^{+0.00039}_{-0.00037}$	$0.04185^{+0.00046}_{-0.00054}$
$0.6320^{+0.0081}_{-0.0048}$	$0.6328^{+0.0055}_{-0.0073}$
$100.84^{+0.53}_{-0.64}$	$100.86^{+0.59}_{-0.53}$
$0.2429^{+0.0188}_{-0.0095}$	$0.2423^{+0.0152}_{-0.0075}$
$0.582^{+0.046}_{-0.028}$	$0.512^{+0.015}_{-0.029}$
$0.511^{+0.020}_{-0.023}$	$0.512^{+0.013}_{-0.028}$
$0.411^{+0.014}_{-0.022}$	$0.411^{+0.013}_{-0.026}$
$1.000^{+0.088}_{-0.094}$	$0.987^{+0.042}_{-0.080}$
1 (fixed)	1 (fixed)
0 (fixed)	0 (fixed)
$0.0001002^{+0.0000049}_{-0.0000035}$	$0.0001004^{+0.0000078}_{-0.0000066}$
$0.0001005^{+0.0000043}_{-0.0000029}$	$0.0000997^{+0.0000045}_{-0.0000072}$
$1.249^{+0.057}_{-0.029}$	$1.242^{+0.062}_{-0.032}$
1 (fixed)	1 (fixed)
0 (fixed)	0 (fixed)
$0.00136^{+0.00014}_{-0.00005}$	$0.001379^{+0.000092}_{-0.000047}$
$-0.000495^{+0.000016}_{-0.000030}$	$-0.000495^{+0.000015}_{-0.000035}$
0 (fixed)	0 (fixed)
0 (fixed)	0 (fixed)
$4.7043515^{+0.0000012}_{-0.0000017}$	$4.7043513^{+0.0000014}_{-0.0000014}$
$105.560361^{+0.000075}_{-0.000069}$	$105.560390^{+0.000072}_{-0.000087}$
23.94 ± 0.15	$23.93^{+0.14}_{-0.10}$

a) We believe that star spot must be located on the primary component due to the behavior of F between seasons. We utilize $L_3 = 0.01$ as an upper limit on the third light contamination and it is likely that L_3 is much less than 0.01. Of these four models, we believe the first column (Prim. spots, $L_3 = 0$) to be the most likely scenario.

Table 4.7:: Physical parameters of LP 661-13

Parameter	Value	Source
M_1 ($M_\odot$)	0.3057 ± 0.0032	This work
M_2 ($M_\odot$)	0.1930 ± 0.0014	This work
R_1 ($R_\odot$)	0.3192 ± 0.0037	This work
R_2 ($R_\odot$)	0.2159 ± 0.0061	This work
V	14.03	Reid et al. (2004b)
R	12.75	Reid et al. (2004b)
I	11.17	Reid et al. (2004b)
J	9.63 ± 0.02	Skrutskie et al. (2000)
H	9.07 ± 0.02	Skrutskie et al. (2000)
K_s	8.76 ± 0.02	Skrutskie et al. (2000)
Spectral Type	M3.5	Reid et al. (2004b)
NIR Spectral Type	M4.27	Terrien et al. (2012)
Distance (pc)	24.9 ± 1.3	This work
Proper motion (RA, mas yr^{-1})	75.1 ± 2.0	This work
Proper motion (DEC, mas yr^{-1})	-227.3 ± 2.0	This work
γ (km/s)	$23.95^{+0.15}_{-0.14}$	This work

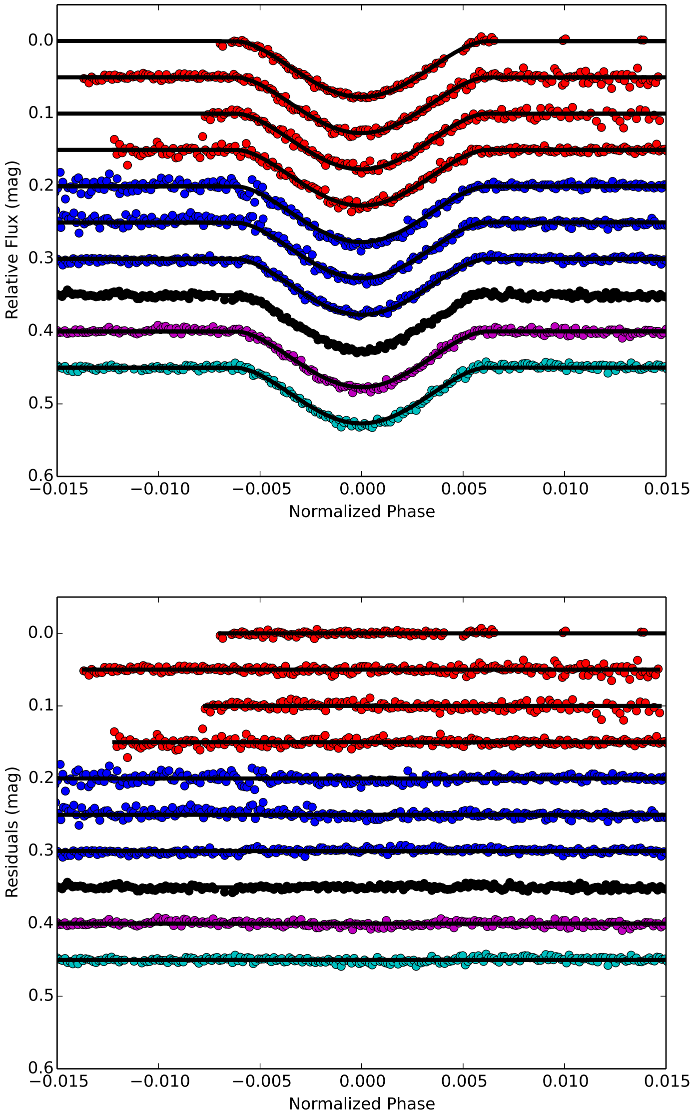

Figure 4.4: Photometric data of all primary eclipses (offset for clarity) from the 2014 - 2015 observing seasons and our model with starspots located on the primary component. We have corrected the data for normalization, meridian offsets, and common mode, which are known systematics in the MEarth data. Residuals are are located in the lower plot. Each color represents data taken from a different MEarth-South telescope.

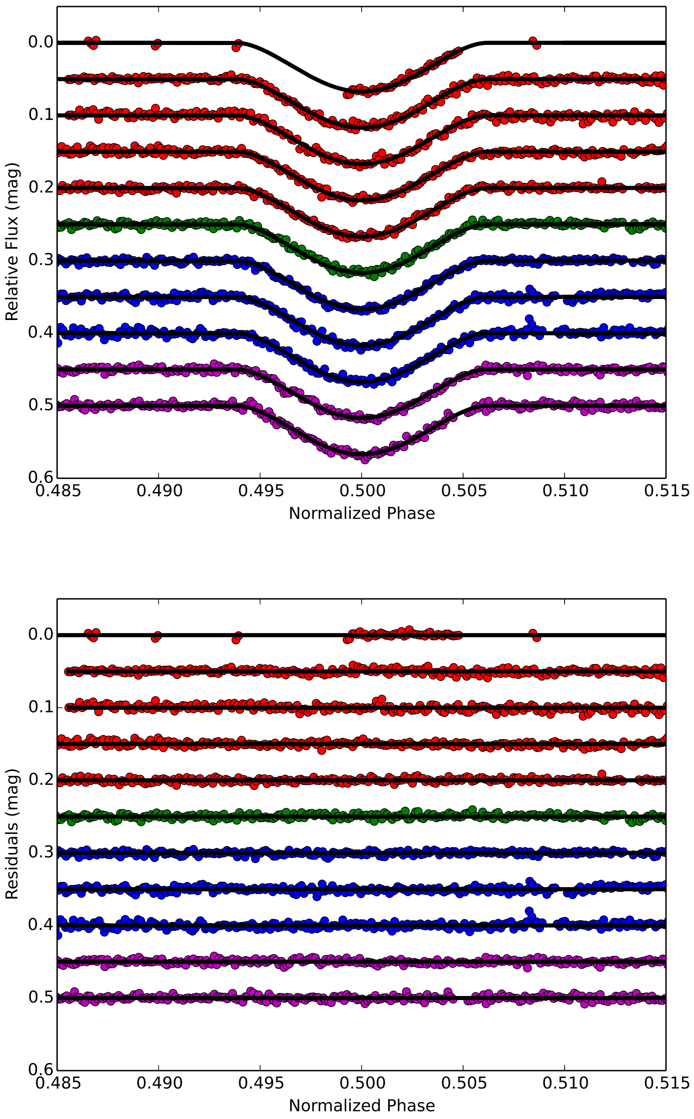

Figure 4.5: Photometric data of all secondary eclipses (offset for clarity) from the 2014 - 2015 observing seasons. The partial secondary eclipse was data taken before we knew the period of the LP 661-13 system. MEarth-South automatically detected an event in-progress and began collecting high cadence follow-up observations until the event ended before resuming normal operations. The colors correspond to the same telescopes as in Figure 4.4. Residuals from the fit are shown in the lower panel.

4.4.1 Third Light

Archival SuperCOSMOS images (see Figure 4.1) indicate that there is a faint background star currently in the MEarth aperture for LP 661-13. This third light can potentially limit our ability to measure the fundamental parameters of each component in this system. The SuperCOSMOS catalogues measures this background star to be 5.3 magnitudes fainter than LP 661-13 in the 103a-E red plate bandpass. Unfortunately, we do not know the color of the background star and therefore do not know the magnitude difference in the MEarth bandpass. While it is unlikely that the background star is as red as LP 661-13, we can measure the maximum possible effect that third light contamination has on determination of LP 661-13's physical parameters by repeating our analysis with third light fixed (arbitrarily) at 1% of the total light of the system. In Tables 4.6 and 4.7 we list the system parameters jointly fitting both seasons of data for third light, L_3 = 0 and 0.01 for models with starspots only on the primary stellar component, and for starspots only on the secondary stellar component. The most likely physical scenario is one where the starspots are concentrated on the more luminous primary and that third light is insignificant for this system. We find that with 1% third light contamination, the masses and radii of each component of LP 661-13 are affected at the 0.5% level, and therefore we do not believe third light to be a significant concern for this system.

4.5 Discussion

We have measured the masses of the primary and secondary components of LP 661-13 to a precision of 1.5% and 1.1% and the radii to 1.1% and 1.8%, respectively. Our error in the mass measurements is dominated by the precision of the TRES instrument while the error in the radii is dominated predominantly by the systematics associated with the starspots, and further seasons of data will aid in reducing these errors. Particularly, if the starspot signal changes significantly between seasons this will aid our ability to break the degeneracies of this model. In future seasons, LP 661-13 will achieve wider separation with the background star, allowing us to measure its color and assess its third light contribution.

Interestingly, the orbit of this system is circular while at least one of the components is not rotating synchronously with the orbit. However, tidal theory suggests that the timescale for synchronous rotation is much shorter than the time scale for circularization, so it is unclear how this system can currently be in the state that we observe it in. We are unable to offer an explanation of this phenomenon.

With these measurements in hand, we can now use these stars as tests of stellar models. In Figure 4.6 we plot the masses and radii for other low-mass eclipsing binary systems, along with the stellar models of (Baraffe et al. 2015) for a 5 Gyr system of solar metallicity. We find that each of the individual components of LP 661-13 are higher than, but marginally compatible with, the most recent stellar models. However, since in eclipsing binary observations the sum of the component radii are better determined than each individual component's radius we can investigate whether this radius sum is significantly higher than expected from stellar models. This also allows us to utilize the 1% precision of our mass measurements in order to fully leverage the available data and test these models. We find that given the measured stellar masses of $0.305M_{\odot}$ and $0.193M_{\odot}$, that we expect a total radius sum of $0.510 \pm 0.005R_{\odot}$. The measured radius sum, $0.536 \pm 0.006R_{\odot}$ lies 5% above the model value, implying a significant radius inflation at 4σ confidence.

One of the most straightforward ways in which an M dwarf might be inflated is due to youth. M dwarfs take significantly longer to settle onto the main-sequence than solar type stars, and may maintain significantly larger radii for up to a billion years. If LP 661-13 is relatively young, we might expect both components to be slightly inflated. We find no evidence for Lithium in either component in our measured spectra, which can set a lower limit on their age. However, since both stars are fully convective, any Lithium originally present in the star would be convected into the interior and destroyed in approximately 10 Myr (Baraffe et al. 2015). Using the stellar models from Baraffe et al. (2015), we find that in order to reproduce the radius sum that we measure, LP 661-13 would need to be approximately 200 Myr old. However, we find no detectable eccentricity in the system and the circularization timescale is 4.3 Gyr. Therefore, we find it unlikely that the average inflation of these stars can be explained through youth and that it is likely that LP 661-13 is a field age system. Furthermore, at this age, we would expect significant X-Ray activity from the system, for which we do not have significant evidence in archival ROSAT data.

Another possible mechanism that may be responsible for M dwarfs' inflated radii is the presence of metals in the atmosphere. The presence of metals and the cool temperatures present in the atmospheres are conducive to the formation of molecules. In turn, these molecules act as a significant source of opacity in the optical, suppressing the amount of energy that is emitted in these frequency bands. To compensate for this the star emits significantly more light in the infrared than in the optical compared to a blackbody spectrum. However, it is possible that the star may also expand slightly to have a greater surface area from which to emit the energy it is producing in the

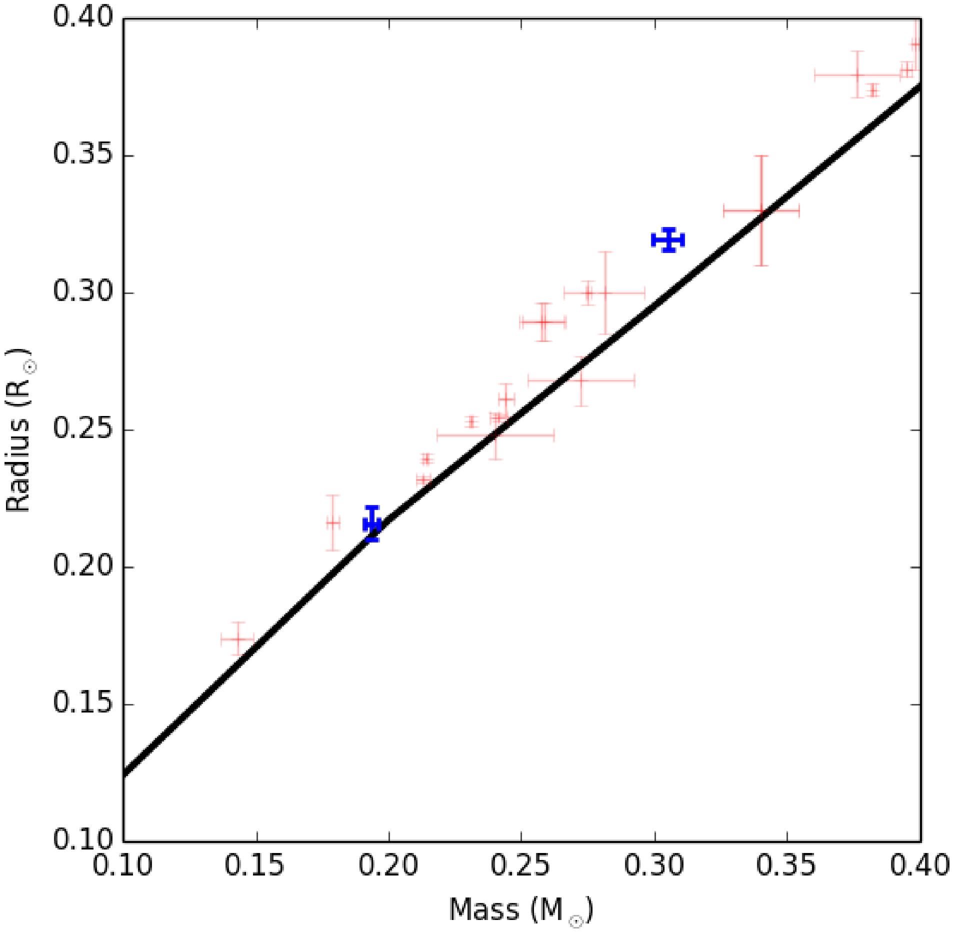

Figure 4.6: The masses and radii for nearby double lined low-mass eclipsing binary stars with highly precise measurements. We plot SDSS-MEB-1 (Blake et al. 2008), GJ 3236 (Irwin et al. 2009b), CMDra (Morales et al. 2009), LP 133-373 (Vaccaro et al. 2007), MG1-2056316, KOI-126 (Carter et al. 2011b), CU Cnc (Ribas 2003), 1RXSJ154727 (Hartman et al. 2011b), HATS551-027 (Zhou et al. 2015b), LSPM J1112+7626 (Irwin et al. 2011b), and WTS19g-4-02069 (Nefs et al. 2013) in red. LP661-13 A and B are indicated by the dark blue crosses. The black line is the stellar model from Baraffe et al. (2015) for a 5 Gyr system with solar metallicity. We find that in aggregate the stellar models tend to underpredict the radius for a star of a given mass. While the radius for each component of LP 661-13 is marginally consistent with the stellar models, we find that the much better constrained radius sum is significantly inflated compared to that predicted by the stellar model.

stellar interior. In this case, the presence of more metals would lead to a slightly larger radius than for a star depleted in metals. While the new stellar models published by Baraffe et al. (2015) are not computed over a range of different metallicities, previous versions of these models (Baraffe et al. 1998), found that metallicity can only account for a 3% increase in the radius from [Fe/H] = -0.5 to [Fe/H] = 0.0. Since the average radius inflation for LP 661-13 is higher than this, it is unlikely that metallicity can fully account for the discrepancy from the stellar models, and likely there is still theoretical considerations to be addressed to fully understand the mass-radius relation of low-mass stars.

4.6 Conclusions

We present here the discovery and analysis of the eclipsing M dwarf - M dwarf binary LP 661-13. We have collected 2 years of eclipse data and precise radial velocity measurements of both components in order to obtain accurate, model-independent measurements of their masses and radii. We find that LP 661-13A is a 0.3057 ± 0.0032 $M_\odot$ star with a $0.307^{+0.010}_{-0.007}$ $R_\odot$ radius while LP661-13B is a 0.1930 ± 0.0014 $M_\odot$ star with a $0.231^{+0.014}_{-0.016}$ $R_\odot$ radius. Both components are slightly inflated in radius when compared to stellar models. However, the radius sum (which is much better constrained) is significantly (4 σ) inflated when compared to the expected radius sum from stellar models. Because the orbit of the system is circularized, it is unlikely that this inflation can be explained through youth. Metallicity is also insufficient to explain the total radius inflation we observe.

In the future, the most straightforward way to improve the measurements of this system is to continue out of eclipse monitoring and obtain additional eclipse observations. Because we have observed some spot evolution between observing seasons, additional evolution will help to break the degeneracies between starspot coverage and inferred stellar radii in the model and provide better constraints on the fundamental parameters of this system. Additionally, we can potentially probe the origin of the radius inflation by investigating the marginal X-ray activity as seen by ROSAT and attempt to measure its surface magnetic field. Eclipse measurements in other photometric bandpasses will allow us, with the trigonometric parallax distance we have in hand, to measure the effective temperatures of each component as well, which will serve as another test of stellar models. LP 661-13 represents another low-mass stellar test case measured with high accuracy and will be a useful benchmark for current and future stellar models. LP 661-13 is positioned equatorially on the sky and therefore is a good object for further study from both northern and southern facilities.

Acknowledgments

The MEarth Team gratefully acknowledges funding from the David and Lucille Packard Fellowship for Science and Engineering (awarded to D.C.). This material is based upon work supported by the National Science Foundation under grants AST-0807690, AST-1109468, and AST-1004488 (Alan T. Waterman Award). This publication was made possible through the support of a grant from the John Templeton Foundation. The opinions expressed in this publication are those of the authors and do not necessarily reflect the views of the John Templeton Foundation. This research has made extensive use of NASAs Astrophysics Data System (ADS), and the SIMBAD database, operated

at CDS, Strasbourg, France.

Chapter 5

Absolute Sloan *griz* Photometry of 150 Mid-to-Late Northern Solar Neighborhood M Dwarfs and a Color-Color Metallicity Relation with 0.10 Dex Precision

This thesis chapter will be submitted to The Astrophysical Journal

J. A. Dittmann, J. M. Irwin, D. Charbonneau, A. Bieryla, A. A. West

Abstract

The USNO $u'g'r'i'z'$ photometric system has become the standard magnitude system for large-scale photometric surveys. However, the USNO system lacks a significant number of photometric standard stars at red colors, leaving this end of the system poorly constrained. We have obtained measurements of $g'r'i'z'$ photometric standard stars with a sloan *griz* filter set along with observations of 150 mid-to-late M dwarfs in the solar neighborhood with a precision of 1%. We provide linear relations to convert measurements between our *griz* photometric system and the $g'r'i'z'$ system. Magnitudes we measure in our *griz* system of mid-to-late M dwarfs that overlap with the Sloan Digitized Sky Survey (SDSS) are found to be inconsistent, and we conclude that the differences between the SDSS *griz* filters and our *griz* filters, when convolved with an M dwarf stellar spectrum, create significant differences. These differences are not reconcilable through typical color equations, and therefore the photometric metallicity relations found in SDSS data will not apply surveys that utilize Sloan-like filters. We find that there is no combination of colors in *griz* filters alone that can reliably determine an M dwarf's metallicity to reasonable accuracy. However, we find that if a near infrared K band magnitude is included, that the $(g-i,\ i-K)$ color plane can be used to photometrically determine an M dwarf's metallicity to 0.1 dex precision. This relation is comparable in precision to NIR spectroscopic methods that have been developed in recent years. Source overlap between the Large Synoptic Survey Telescope (LSST) survey and the Visible and Infrared Survey Telescope for Astronomy (VISTA) survey will allow M dwarfs to act as chemical probes of the Milky Way.

5.1 Introduction

M dwarfs make up 75% of all stars in the Milky Way. The M dwarf sequence begins at approximately 0.6 $M_\odot$ and ends at the main sequence turn off at 0.08 $M_\odot$, although this boundary can vary with age and composition. Midway through this mass sequence, M dwarfs lose their interior radiative zone and become fully convective from core to surface. In contrast, the Sun's outer convective envelope (containing 2% of the solar mass) only extends approximately 200,000 km (28% of the solar radius) inwards. Models of stellar structure that try to capture these changes have difficulties reproducing the observed mass-radius relation at the low mass end (Torres 2013). Particularly, stellar models tend to under predict the radius and over predict the temperature compared to observations. The temperatures present in M dwarf atmospheres allow molecular species such as TiO, VO, FeH, and CaH, among others, to form. These molecules blanket the optical spectrum with many overlapping lines and bands, eliminating the spectral continuum and suppressing the star's optical flux. Complete line lists for identified species in M dwarf atmospheres, particularly at relevant temperatures, are lacking and some species remain to be identified. The absence of continuum also inhibits directly measuring an M dwarf's metallicity from direct measurements of line strengths.

While forward modeling an M dwarf spectrum to compare to observations and measure metallicities has proven difficult, empirical relationships have shown significant ability to determine an M dwarf's physical properties. M dwarfs in wide binaries with more massive F, G, or K primary stars likely formed out of the same bulk composition. Therefore, the metallicity measured in the primary star can be assumed for the M dwarf to calibrate an empirical relation. Bonfils et al. (2005) analyzed a sample of 20 M dwarfs with solar type primary stars and calibrated a photometric metallicity relation using the stars' absolute K band magnitudes (M_K and its $V - K$ color). They estimated the precision of this relation to be 0.2 dex. However, Johnson & Apps (2009) found that this calibration was not useful outside of Bonfils et al. (2005)'s narrow calibration range and significantly underestimated the metallicity of M dwarfs with high metallicities. Follow-up work by Schlaufman & Laughlin (2010) expanded the calibration sample and widened the spectral type range as well. Their photometric metallicity relation had a precision of 0.15 dex, although Neves et al. (2012) tested this calibration on a separate sample of FGK - M common proper motion binaries and found an RMS precision of 0.19 dex in metallicity.

Advances in estimating metallicity directly from a stellar spectrum have been made by moving from the optical to the near infrared, where the density of spectral lines and molecular features is much lower. Rojas-Ayala et al. (2010) found that the combination of the Na I doublet and the Ca I triplet in the K-band can reliably determine an M dwarf's metallicity with a correction for the effects of temperature. This calibration was then updated by Rojas-Ayala et al. (2012) and applied to 133 solar neighborhood M dwarfs. A similar metallicity index in the near infrared H band was discovered by Terrien et al. (2012) with a precision of 0.14 dex. Taking a broad approach, Mann et al. (2013a) used stellar spectra spanning 0.35 - 2.45 microns and found metallicity sensitive features throughout. Infrared features produced a metallicity precision of 0.1 dex, but they found an optical-only calibration could be accurate to 0.16 dex (Mann et al. 2013a). By using early M dwarf - late M dwarf binary pairs, Mann et al. (2014) was able to bootstrap this calibration towards lower mass stars. These techniques were also refined and pushed towards redder target stars by Newton et al. (2014), who obtained metallicities for 447 nearby M dwarfs with a precision of 0.12 dex using solely the K band Na line.

The Sloan Digital Sky Survey (SDSS) has provided us with 32 million M dwarfs in its photometric study (Bochanski et al. 2010), of which 40,000 M and L dwarfs have optical spectra (West et al. 2008). These stars have also served as useful probes of the local Milky Way thin and thick disks (Fuchs et al. 2009; Bochanski et al. 2010). The ratio of the strengths of an M dwarf's TiO and CaH molecular indices serves as a useful metallicity indicator, and these indices can be measured directly from the SDSS spectra of SDSS M dwarfs (Lépine et al. 2007). West et al. (2011b) took advantage of this index in order to identify a correlation between these indices and the $g - r$ and $r - z$ colors of SDSS M dwarfs. Even though this relationship was coarse, West et al. (2011b) was able to exploit the ubiquitousness of M dwarfs in the Milky Way and this relation in order to probe the metallicity distribution of the Milky Way as a function of height above the Galactic plane.

The future Large Synoptic Survey Telescope (LSST) is slated to be on sky in 2019. LSST will observe the full southern sky in the Sloan *ugriz* filters every few nights, collecting millions of exposures over its 10-year survey lifetime. During this survey, LSST will uncover millions of M dwarfs in the Milky Way, out to a distance of 10 kpc. As LSST is a photometric survey only, it will be necessary to push photometric techniques as far as possible in preparation for the wealth of data and discoveries that LSST is set to unveil.

In this paper, we describe calibrations and differences between various filter systems. In order to clarify this discussion, we will define here the various filter systems and nomenclature we will use through the rest of this paper. The Sloan filter system, particularly the response function of its filters, is defined in Fukugita et al. (1996). However, the academic definition of this filter system is also defined by the camera at the SDSS Monitor telescope, whose sensitivity is different from the system used for the SDSS survey. In fact, Fukugita et al. (1996) defines the Sloan filters themselves, but does not describe any physical Sloan *photometric system*.

There are currently two nominal Sloan photometric systems, with differences that will become important throughout this text. There is the primed $u'g'r'i'z'$ system and the unprimed $ugriz$ system. The primed system is defined by the United States Naval Observatory (USNO) 40 inch telescope, which defines a network of primary standard stars and their primed magnitudes (Smith et al. 2002). In contrast, the unprimed $ugriz$ system refers to the magnitudes as measured by the SDSS survey itself. The differences between these systems originate in shifts in the Sloan filters in the SDSS telescope. The filters used for the SDSS survey, when placed under vacuum in the same housing as the SDSS detectors, show a decrease in their effective refractive index. Because the Sloan filters use an interference cutoff at the red end of each filter, this moves the red edges of the filter blueward by approximately 2.5% of the cutoff wavelengths, compared to the $u'g'r'i'z'$ system at USNO, where the filters are kept in ambient air. The SDSS collaboration has provided linear transformations with small color terms to convert between the primed and unprimed systems, but they explicitly note that these transformations are not to be applied to very cool objects or objects with complex spectra[1]. M dwarfs, by their nature, are very cool objects and have complex spectra, and therefore we can expect there to be significant differences between the $u'g'r'i'z'$ system

---

[1] http://classic.sdss.org/dr7/algorithms/fluxcal.html

and the *ugriz* system for these stars.

In this paper, we describe a photometric calibration of the Sloan system for cool, red objects observed with the Fred Lawrence Whipple Observatory (FLWO) 48 inch telescope with KeplerCam. All together, we will discuss 3 photometric systems. The primed $u'g'r'i'z'$ system magnitudes, which we described above, are measurements defined by the USNO 40 inch telescope and the network of standard stars observed in Smith et al. (2002). We will further reference two unprimed systems, which we will denote with subscripts. $u_{SDSS}g_{SDSS}r_{SDSS}i_{SDSS}z_{SDSS}$ will refer to the system defined by the SDSS survey, with its shifted filter system. $u_{48}g_{48}r_{48}i_{48}z_{48}$ will refer to the observations we describe in this paper, taken using the FLWO 48 inch telescope with Keplercam and its set of Sloan filters.

We have observed 150 mid-to-late M dwarfs in g_{48}, r_{48}, i_{48}, and z_{48} from this site on photometric nights, calibrated against Sloan standard stars from the primed system observed on these same nights. By combining these observations with trigonometric parallax measurements and spectroscopic metallicity measurements, we calibrate a luminosity-color-metallicity relation with a precision of 0.12 dex and a color-color metallicity relation with a precision of 0.10 dex. In section 2, we describe our observing program and our target stars. In section 3, we detail our analysis method, our photometric model, and a detailed description of our photometric system, as well as a conversion between the $g_{48}r_{48}i_{48}z_{48}$ and the $g'r'i'z'$ system. Section 4 details our metallicity relation and implications for LSST.

5.2 Observations

All observations were taken with the 48-inch telescope on Fred Lawrence Whipple Observatory (FLWO) on Mt. Hopkins, AZ with the KeplerCam CCD. KeplerCam uses back illuminated 4096×4096 Fairchild CCD 486 detector with a pixel scale of $0.336''$ pix^{-1} unbinned. All images were taken in the 2×2 binning mode, with a detector full well of 100,000 counts per pixel. KeplerCam images are read out by 4 amplifiers, subdividing its 23.1×23.1 arcmin field of view into 4 equal sections. For this work, we used only one quarter of the full CCD, with all of our targets centered in amplifier 2. This is typical of work done with this instrument, as amplifier 2 has the lowest gain and a more uniform flat field, though the full CCD was used for the Kepler Input Catalog.

The FLWO 48-inch has a set of Sloan filters available for use. [2] In Figure 5.1, we show the filter transmission curves for the 48-inch Sloan filters, and we list the transmission curve for each filter in Table 5.1.

We obtained data on 21 nights that we believed were going to yield photometric conditions based upon satellite imagery and the meteorological instrumentation on Mt. Hopkins. Due to this opportunistic observing strategy, these nights were typically shared with other observing programs on the instrument on a first-half/second-half basis, although occasionally we were the sole program observing on a given night.

Each observing night, prior to sunset, we obtained a series of bias and $g'r'i'z'$

---

[2] The filters used in this work differ from the Sloan filter set used to make the Kepler Input Catalog (KIC) (Brown et al. 2011), as the FLWO filter set was replaced in 2011. We caution that the results presented in this paper should not necessarily be applied to the magnitudes reported in the KIC, as differences in these filter sets may be significant.

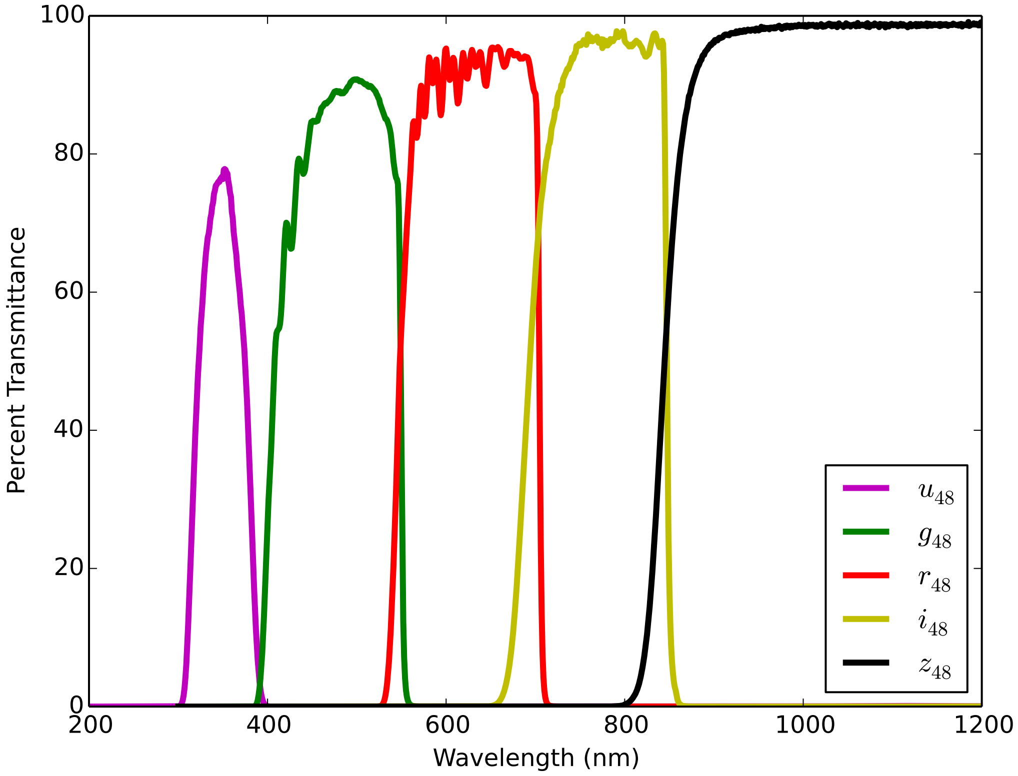

Figure 5.1: Filter transmission profiles for the *ugriz* filter set available at the FLWO 48-inch telescope. These filters are a different filter set than those used to make the KIC (Brown et al. 2011). The new filters more closely match the definitional Sloan filters. We make the filter curves available in Table 5.1.

dome flat images for calibration purposes. We began science observations with a series of equatorial Landolt standard fields (Landolt 1992) with measured $g'r'i'z'$ magnitudes from Smith et al. (2002). We only observed standard fields that are at or below an airmass of $X = 2.0$. We took 8 exposures of each field, in the filter order $g_{48}, r_{48}, i_{48}, z_{48}, z_{48}, i_{48}, r_{48}, g_{48}$, providing two independent frames per filter per pointing. After this set of calibration images, we took a set of exposures of two or three bright ($r_{SDSS} \approx 14$) Sloan Digitized Sky Survey (SDSS) M dwarfs from West et al. (2011b). These calibration and SDSS M dwarf observations typically take between 60 and 90 minutes to perform. Once complete, we obtained $g_{48}, r_{48}, i_{48}, z_{48}, z_{48}, i_{48}, r_{48}, g_{48}$ science images of our target M dwarfs. Before observing each field, an acquisition image was taken to verify pointing and to move the target star to the same region on the detector (typical precision of 10 pixels).

Our target M dwarfs are a subset of the MEarth-North target list. The MEarth-North target list is itself a subset of 1844 nearby M dwarfs from the LSPM-North catalog (Lépine & Shara 2005) believed to be within 33 parsecs of the Sun (Lépine 2005). Our targets are further downselected to stars whose colors indicate that they likely have $R < 0.33 R_{\odot}$ (Nutzman & Charbonneau 2008). For this program, we further required that our targets have trigonometrically measured distances, and metallicity measurements derived from near infrared spectroscopy from Newton et al. (2015a). One set of target observations is chosen to take the same amount of exposure time as our standard field and SDSS M dwarf observations, typically one hour. After each set of target stars we repeat our standard star and SDSS M dwarf observations, replacing fields that have set with fields that are rising. Each set of target star observations contains a new set of targets; we do not return to the same target stars in a given night. However, on some nights we do obtain additional observations of target stars that had been observed in previous nights in order to assess possible systematic errors between nights. The majority of target stars are observed on only one individual night. We begin and end each night of observations with a set of standard star observations, to ensure that we have full time-domain coverage of the atmospheric conditions.

The data presented here were taken between October 28, 2014 and June 01, 2015, Arizona time. Typical seeing on Mt. Hopkins on photometric nights and across our observations is $1''$. We combined our bias frames from each night with the IRAF[3] command *zerocombine*. We bias-subtract each image and then median-combine our bias subtracted flat field images. We divide each image by the normalized flat field to correct for flat-fielding effects. We have not corrected our z_{48} band images for fringing effects nor made a nonlinearity correction. We performed aperture photometry using the task PHOT in the IRAF DAOPHOT package. We utilized a 13 pixel ($8.7''$) diameter aperture for all observations, with an inner sky annulus of 15 pixels and an outer sky annulus of 20 pixels. Using apertures of 10 pixels (with the same sky annulus) and 16 pixels (with an inner and outer sky annulus at 20 and 25 pixels) did not significantly change the number of measured counts (in ADU). Therefore, we believe that we are not significantly affected by counts that lie outside of our aperture and do not need to perform an aperture correction. All observed calibration and target stars are chosen to be contamination-free (or nearly contamination-free in the case of close binaries) and we do not believe contamination to be a significant source of error in our measurements.

---

[3] IRAF is distributed by the National Optical Astronomy Observatory, which is operated by the Association of Universities for Research in Astronomy, Inc., under cooperative agreement with the National Science Foundation.

5.3 Analysis

We adopt the following model to describe out observations:

$$m_{*,f} = z_f^i - 2.5\log_{10}(f_{obs}/t_{exp}) - \Big(k_{1,f}^i + k_{2,f}^i(m_{*,g} - m_{*,i})\Big)\times(X-1) \tag{5.1}$$

where $m_{*,f}$ is the magnitude of the star in filter f, z_f^i is the zero point of the instrument on night i in filter f, f_{obs} is the observed flux (in counts per second) for the star, t_{exp} is the exposure time of the image, $k_{1,f}^i$ and $k_{2,f}^i$ are fitted coefficients for airmass and color effects, respectively, for night i in filter f, and X is the airmass of the object. Here, i and f denote the night of the observation and the filter used.

We initialize the 48-inch system close to the $g'r'i'z'$ system defined in Smith et al. (2002) by fitting for the airmass coefficient, color coefficient, and zero point offset for each night and each filter. Once we have this initial solution, we relax the requirement that our measured magnitudes match that of Smith et al. (2002) and we fit for the $g_{48}r_{48}i_{48}z_{48}$ magnitudes for each star. We then iterate between fitting the magnitude of each star across all nights and the nightly atmospheric coefficients for each night until the solution has converged. During this process, we eliminate 3 nights for which the standard star magnitudes show RMS deviations great than 0.05 magnitudes (23 December 2014, 4 January 2015, and 08 May 2015). These nights also show significantly higher extinction (via the telescope zero points) than for other nights and we believe these nights to not be photometric. We also eliminate two additional nights, April 8-9, 2015. On these nights there was an error with the telescope filter wheel control system, and observations were not taken in the correct filters. The median absolute deviation

(MAD, Hoaglin et al. 1983) for any given night ranges from 0.005 magnitudes to 0.02 magnitudes. In Table 5.2, we list the atmospheric parameters (k_1, k_2, z) for each filter on each night as well as the MAD for each night.

All together, we obtained observations on 16 nights that exhibited photometric conditions. On these 16 nights, we obtained observations of 34 standard stars from the selected areas in Landolt (1992) with $g'r'i'z'$ measured by Smith et al. (2002), observations of 10 M dwarfs from SDSS, and observations of 150 mid-to-late Northern hemisphere M dwarfs from the LSPM-N catalog. In Tables 5.3 and 5.4 we list the observed 48-inch Sloan $g_{48}r_{48}i_{48}z_{48}$ magnitudes for our standard stars and target M dwarfs, respectively. For our target stars, we also list the MAD for the night the measurement was made, whereas for the standard stars and SDSS M dwarfs we list the MAD across all photometric nights of observations for that star. We also list the variance for each star. The magnitudes for stars with high variance (0.05 magnitudes and larger) should be treated with caution. Particularly, M dwarfs with high variance in their blue magnitudes may have been undergoing a flare at the time of observations. Due to the low number of total observations made of each star, we cannot eliminate data points based on stellar activity.

5.3.1 Converting between the FLWO Sloan and the USNO Sloan Systems

It is desirable to be able to convert our native FLWO $g_{48}r_{48}i_{48}z_{48}$ magnitude system to the USNO $g'r'i'z'$ system. Unfortunately, the $g'r'i'z'$ system lacks a significant number of red standard stars. Of the 158 stars in the Smith et al. (2002) standard star network, only 12 have a $g' - i'$ color greater than 2, and only 5 of those have a $g' - i'$ color greater than 2.5. In contrast, all of our observed SDSS M dwarf stars have a $g - i$ color greater than 2 and only 3 of 150 of our target M dwarfs have a $g - i$ color less than 2.5. We show a histogram of the $g_{48} - i_{48}$ colors for the Sloan standard stars and for our M dwarf target stars in Figure 5.2. This lack of red standard stars in the USNO $g'r'i'z'$ system limits the effectiveness of converting between these two systems. When fitting the atmospheric color coefficient (k_2) in our native system, we made use of the SDSS M dwarfs we observed as part of our calibration observations. As these M dwarfs are significantly redder than the USNO standards, they are affected by the k_2 term more than bluer stars and therefore have significant weight in determining that term in our model, even though all stars are weighted equally. While this is desirable because we would like our photometric system to be constrained over as broad a color range as feasible, we may also accrue additional error at the blue color end because the USNO $g'r'i'z'$ system did not have to fit atmospheric color effects for stars this red. Nevertheless, we adopt a simple linear model in $g - r$ color space to convert our measured $griz$ magnitudes to the $g'r'i'z'$ photometric system. We use solely our observations of stars from Smith et al. (2002), and do not use our SDSS M dwarf observations or convert their SDSS magnitudes from West et al. (2011b) to the $g'r'i'z'$ system. We find:

$$g_{48} - g' = -0.0228(g_{48} - i_{48}) + 0.0119 \tag{5.2}$$

$$r_{48} - r' = -0.0016(g_{48} - i_{48}) - 0.0046 \tag{5.3}$$

$$i_{48} - i' = -0.0075(g_{48} - i_{48}) - 0.0075 \tag{5.4}$$

$$z_{48} - z' = -0.0192(g_{48} - i_{48}) - 0.0019 \tag{5.5}$$

The median absolute deviation of these relations are 0.015, 0.012, 0.016, and 0.017 magnitudes for the g-band, r-band, i-band, and z-band, respectively. In Figure 5.3, we plot these relations along with all of the photometric standards observed in our program.

5.3.2 The problem with r_{48}, r', r_{SDSS} and red stars

We further find that our calibration observations of SDSS M dwarfs show significant differences in measured magnitudes in our Sloan $g_{48}r_{48}i_{48}z_{48}$ system when compared directly to the SDSS magnitude system. The differences in magnitudes between the $g_{48}r_{48}i_{48}z_{48}$ magnitudes and the $g_{SDSS}r_{SDSS}i_{SDSS}z_{SDSS}$ magnitudes for our observed SDSS M dwarfs have median absolute deviations of 0.1 magnitudes or larger in all filters, making direct conversion between the SDSS magnitude system and our Sloan magnitude system at red colors highly uncertain. The reason for this dispersion is likely due to the significant difference between the SDSS filters (which exhibited an effective wavelength shift when put under a vacuum in the SDSS telescope) and the shape of an M dwarf spectrum in this wavelength regime. In Figure 5.4, we plot the Sloan and SDSS filter passbands on top of an M4V stellar spectrum. We note in particular that the edge of the r' band lies close to a prominent molecular TiO feature, and therefore small shifts in the bandpass or sensitivity of the filter may significantly affect the r magnitude, making estimating stellar parameters with high accuracy difficult. In contrast, the g-band is relatively free of this problem (although there are features at the edges of all filters). Therefore, for the rest of this paper, we will utilize our Sloan g_{48} measurements in obtaining a photometric metallicity relation relevant for M dwarfs in place of r_{48}.

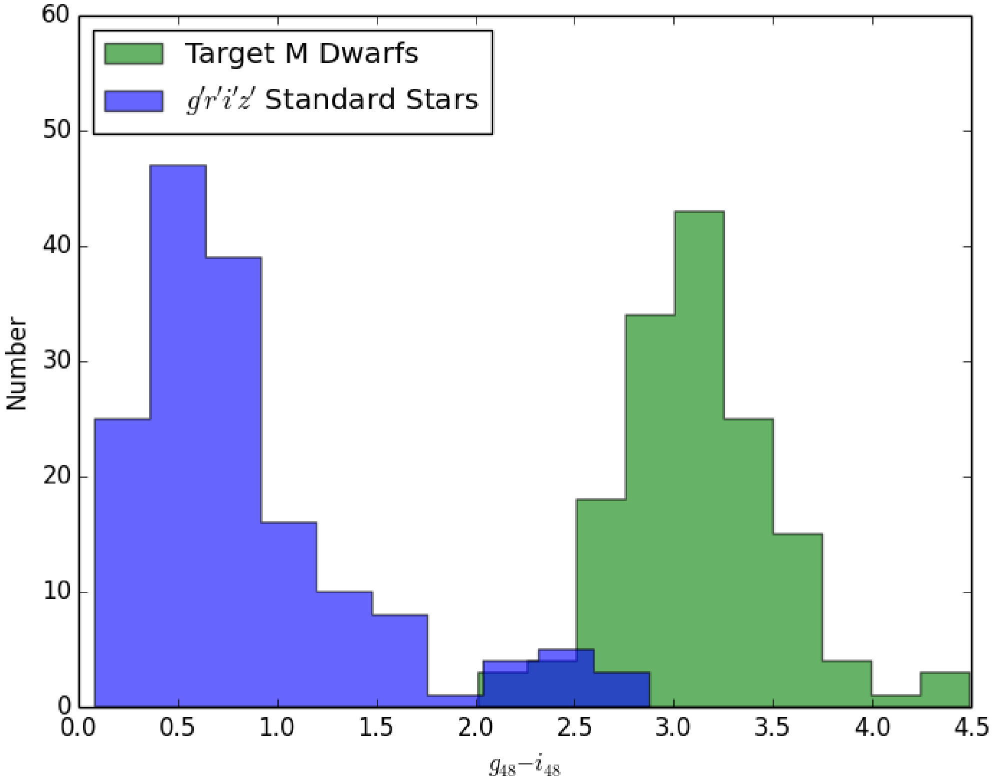

Figure 5.2: Histogram of the $g' - i'$ colors of the $g'r'i'z'$ standard star network (blue) with the measured $g_{48} - i_{48}$ colors of our target M dwarfs (green). The primed system standard star network lacks a significant number of red standard stars, making the red end of the Sloan filter system highly uncertain. In contrast, nearly all of our target M dwarfs have a $g_{48} - i_{48}$ color greater than 2.5, making the atmospheric color term much more important when performing our calibration.

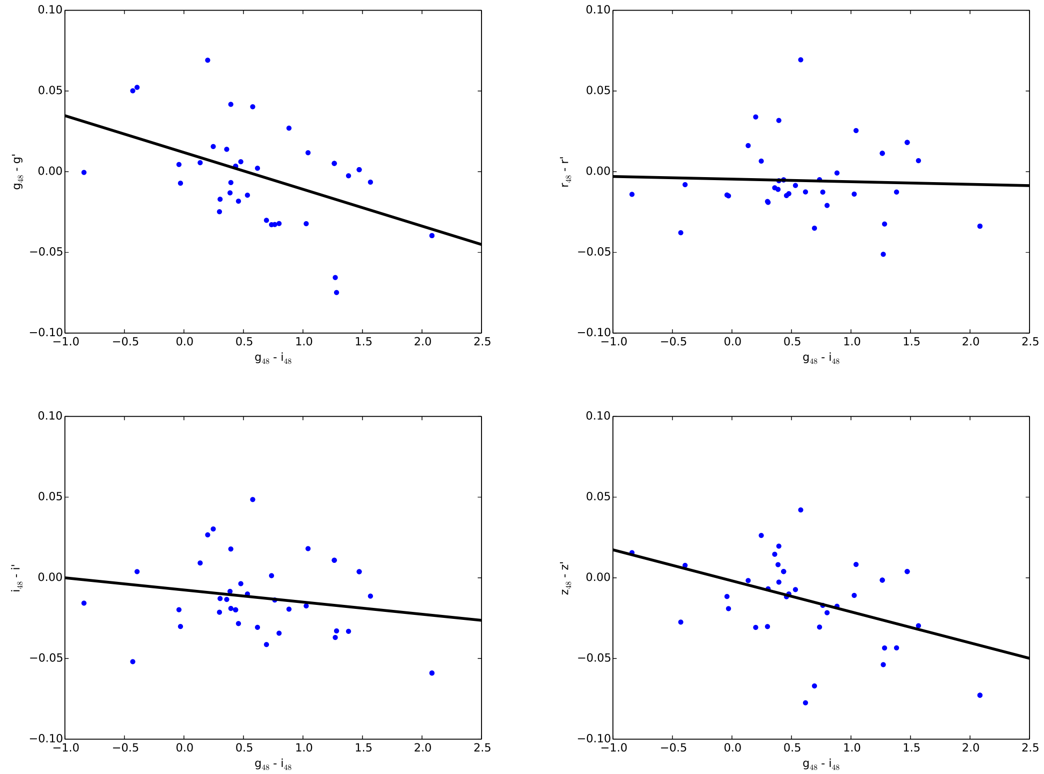

Figure 5.3: Differences between the 48-inch FLWO Sloan system and the USNO Sloan system as a function of $g-i$ color in the FLWO Sloan system. Each blue point represents an observed star from the standard star network presented in Smith et al. (2002). We note that the USNO $g'r'i'z'$ system lacks standard stars at significantly red colors. Particularly, only 5 of the 158 standard stars in Smith et al. (2002) have a $g' - i' > 2.5$ while only 3 of our 150 target M dwarfs have a $g_{48} - i_{48} < 2.5$. The lack of dwarf standard stars at these colors (where the k_2 term in equation 5.1 becomes more significant) may account for some of these differences in our filter system, as Smith et al. (2002) did not have to account for these red of colors.

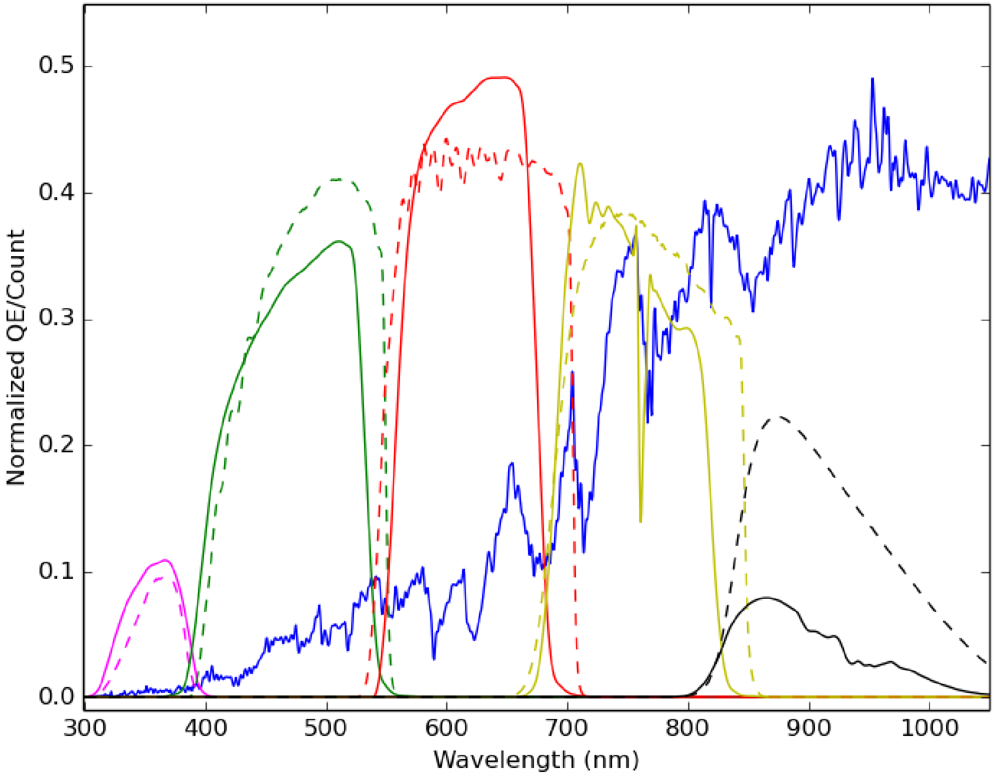

Figure 5.4: Filter curves for the *ugriz* filter system (magenta, green, red, yellow, black), with the SDSS filters as solid lines and the FLWO 48-inch filter system as dashed lines. An M4V spectrum from the Pickles (1998) library is plotted in blue. We note the large difference in the red cutoff in the two r filters and its placement close to a sharp molecular TiO feature in the stellar spectrum. For this reason, we recommend not using broad band r measurements for photometric studies of M dwarfs, as slight differences between filters and radial velocity differences in stars may push this feature into and out of the broad band filter, creating metallicity and kinematic biases. Instead, we recommend the use of the g band magnitudes for these stars, as this portion of the spectrum does not exhibit this problem.

5.4 Discussion

5.4.1 A luminosity-color-metallicity relation for mid-to-late M dwarfs

Armed with natively measured *griz* magnitudes for 150 mid-to-late M dwarfs with spectroscopically measured metallicities, we can calibrate a photometric metallicity relation and eliminate the need for (time-consuming) spectroscopic measurements and allow M dwarfs in large-scale surveys to be used as Galactic probes. We first attempt to calibrate a luminosity-color-metallicity relation, as the M dwarfs in our sample all have measured trigonometric parallaxes. In Figure 5.5, we plot the absolute 2MASS K_s magnitude and the absolute i_{48} magnitude for our M dwarf sample as a function of $g_{48} - i_{48}$ color. Metallicity measurements are taken from Newton et al. (2015a), which is a calibration of the metallicity combinations of Mann et al. (2013a) and Mann et al. (2014). Similar to previous studies (Bonfils et al. 2005; Neves et al. 2012; Schlaufman & Laughlin 2010) and our own previous work (Dittmann et al. 2016), we find that at a fixed absolute magnitude (both i_{48} and M_K), metal rich M dwarfs are generally redder than their metal poor counterparts.

We fit a 2d linear spline in color, absolute magnitude, and metallicity to our target stars using the method described in Dierckx (1981). We overplot a [Fe/H] = 0 main sequence of this interpolation in Figure 5.5, and make this main sequence available in Table 5.5. Our interpolation utilizing $g_{48} - i_{48}$ and M_i is able to reproduce the measured metallicities with a median absolute deviation of 0.080 dex (0.118 dex standard deviation), comparable to the precision of the spectroscopic measurements themselves.

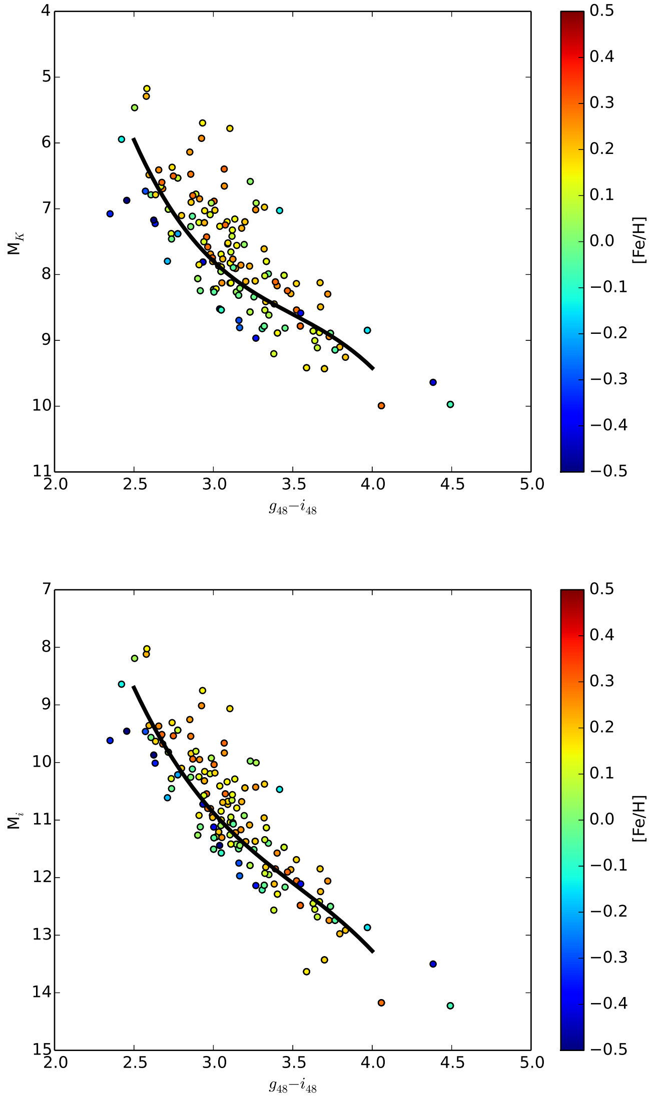

Figure 5.5: Color-Luminosity-Metallicity diagrams for the target M dwarfs in our observing program. The top plot shows the absolute K band magnitude as a function of $g_{48} - i_{48}$ color, while the bottom plot shows the absolute i_{48} band magnitude as a function of $g_{48} - i_{48}$ color. Target star data points are colored according to their spectroscopic metallicity derived from near-infrared spectra (Newton et al. 2015a). We plot an interpolated [Fe/H] = 0 main sequence in black. As we found in Dittmann et al. (2016) for these stars, the more metal rich stars at a given M$_K$ appear redder in color than metal poor stars. We have calibrated a $(g - i,\ M_K)$ metallicity relationship with a median absolute deviation of 0.080 dex and a $(g_{48} - i_{48},\ M_K)$ metallicity relationship with a median absolute deviation of 0.077 dex. We do not make any attempt to remove possible unresolved binaries or over luminous sources. Both binaries and over luminous sources will have a bright absolute magnitude than their color would suggest, allowing them to masquerade as metal-rich stars of higher mass.

Our interpolation utilizing $g_{48} - i_{48}$ and M_K performs slightly better, with a median absolute deviation of 0.077 dex (0.114 dex standard deviation).

5.4.2 A color-color-metallicity relation for mid-to-late M dwarfs

A significant downside of requiring an absolute magnitude to determine through photometric means an M dwarf's metallicity is the requirement of a distance measurement or estimate of the star in question. The upcoming LSST survey will discover millions of M dwarfs in the Milky Way, but very few of these stars will be bright enough to have a distance measurement from GAIA or will ever have a near-infrared spectrum taken from which to determine metallicity. Therefore, their use as Galactic probes will be limited by our ability to determine their fundamental properties from purely photometric data.

West et al. (2011b) note that the metallicity indicator ζ, a measure of the relative strength of the TiO and CaH bands (Lépine et al. 2007), correlates with the SDSS $g - r$ and $r - z$ colors of SDSS M dwarfs. West et al. (2011b) also note that ζ correlates with an M dwarf's height above the Galactic plane. Because height above the Galactic plane is expected to increase with age, they suggest that ζ is a useful metallicity indicator, as older stars are more likely to be metal poor. In Figure 5.6 we plot our measured $g - r$ and $r - z$ colors for our target stars, again colored by their measured spectroscopic metallicity. We do not find a significant metallicity calibration with this color combination alone. We believe this failure to be due to the shift in the SDSS r filter when compared to the standard r' filter (see section 5.3.2), as the spectral features present in ζ lie near the red edge of the r' band.

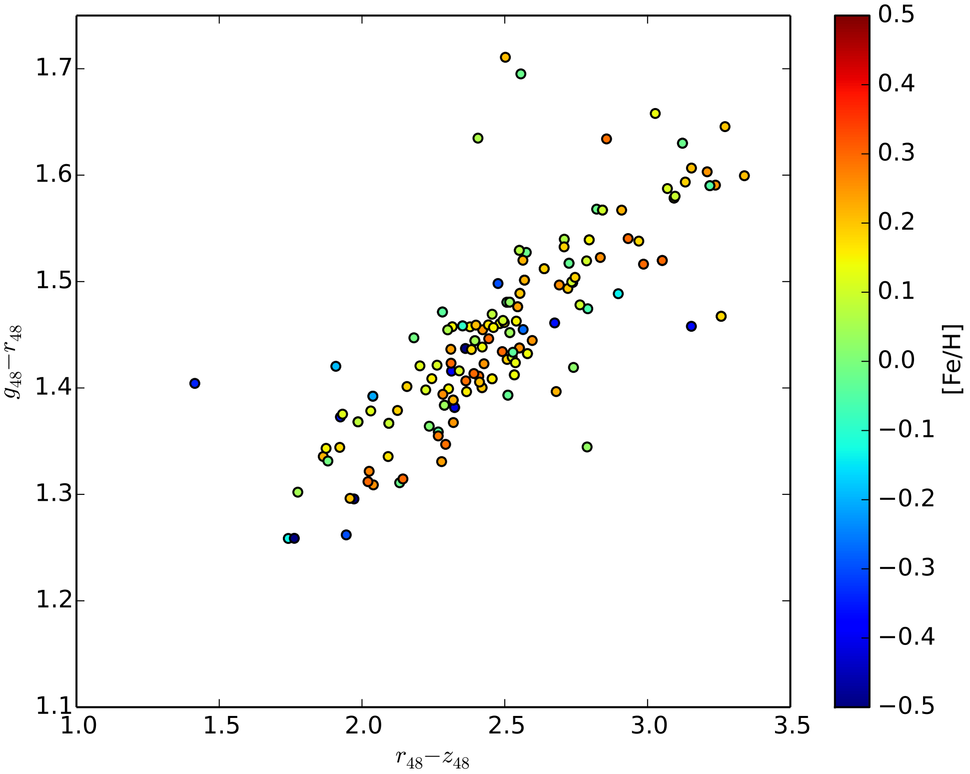

Figure 5.6: $g_{48} - r_{48}$ vs $r_{48} - z_{48}$ for our target M dwarfs. Each data point is colored with the spectroscopic metallicity determined by Newton et al. (2015a). This color index has been previously shown by West et al. (2011b) using SDSS data to be correlated with ζ (Lépine et al. 2007), an optical spectroscopic metallicity indicator. The ζ index relies on the relative strength of the TiO features and CaH, CaH_2 and CaH_3 features, which lie between 681.4 and 699.0 nanometers. The location of the TiO feature in particular lies on the red cut-off of the SDSS r-band filter. We suggest that the photometric metallicity relationship found by West et al. (2011b) applies to data taken with only the (wavelength-shifted) SDSS filters and is not valid for studies with filters closer to the Sloan photometric system. We do not find any significant correlation with metallicity solely with these two colors.

We attempted to calibrate a color-color metallicity relation utilizing our remaining colors. In Figure 5.7 we show the $g_{48} - i_{48}$ vs. $i_{48} - z_{48}$ color plane for our observed targets. We find a slight correlation with metallicity with these two colors. The median absolute deviation in the metallicity of our interpolation when attempting to predict the metallicity of our target stars is 0.093 dex, while the standard deviation is 0.160 dex. This is only slightly smaller than the 0.19 dex standard deviation of the metallicity of our target stars. Therefore, while we find that a star's location in the $g_{48} - i_{48}$ vs. $i_{48} - z_{48}$ color-color plane is marginally sensitive to an M dwarf's metallicity, we find that this relation is too inaccurate to be of use in future studies. Furthermore, we find that there is no precise color-color metallicity indicator that uses solely optical Sloan colors.

If we use data from the 2 Micron All Sky Survey (2MASS) (Skrutskie et al. 2000), we are able to find a set of colors that is sufficiently correlated with metallicity to create a robust calibration. In particular we find that utilizing the 2MASS K_s band photometric data is the most effective. This is not surprising, as Delfosse et al. (2000) has previously found that the absolute K_s magnitude of an M dwarf is a good indicator of the star's mass and is not particularly sensitive to metallicity. Using the K_s magnitude in one of our colors allows us to decouple the color change caused by a changing stellar mass with the color change caused by the increase or decrease of metals in the stellar atmosphere.

In Figure 5.8, we show the $g_{48} - i_{48}$ vs. $i_{48} - K_s$ color plane for our observed targets, with each data point colored by its spectroscopically determined metallicity. We find these colors to be an indicatior of the metallicity of the object, with a bluer $g_{48} - i_{48}$ at a given $i_{48} - K_s$ color trending towards lower metallicities. An interpolation using our data is able to reproduce the spectroscopically measured metallicities from Newton et al. (2015a) with a median absolute deviation of 0.065 dex (standard deviation of 0.096 dex).

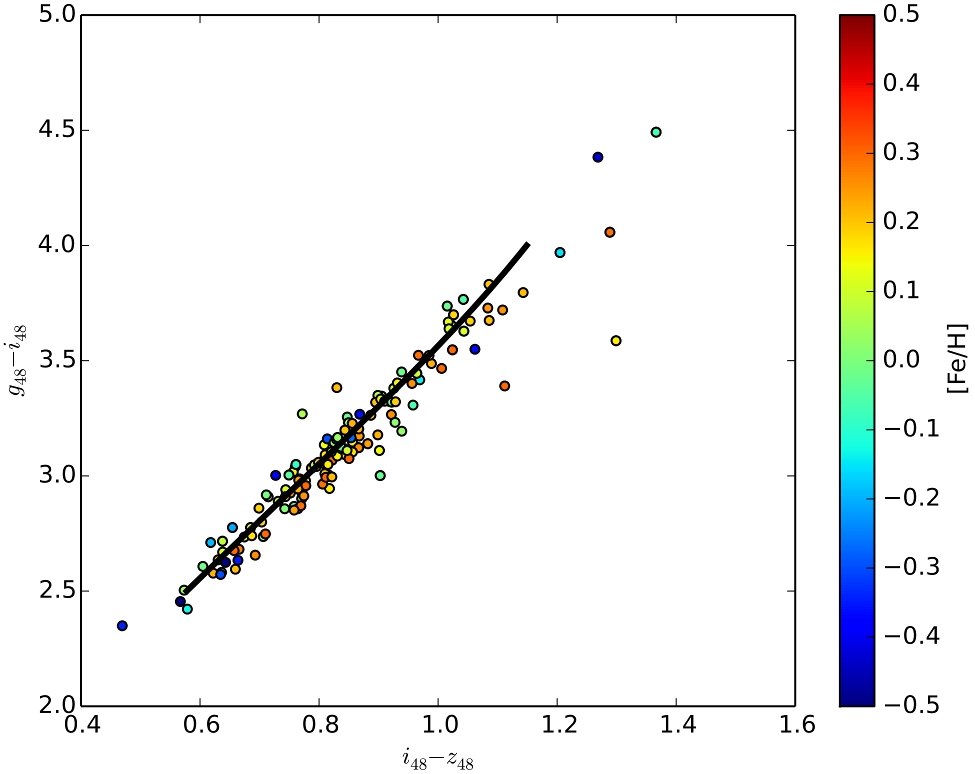

Figure 5.7: $g_{48} - i_{48}$ vs $i_{48} - z_{48}$ for our target M dwarfs. Each data point is colored with the spectroscopic metallicity determined by Newton et al. (2015a). We show an interpolated [Fe/H] = 0 main sequence in black. While these two colors show a slight correlation in metallicity, the standard deviation of the residuals of our interpolation is 0.16 dex. This is only slightly less than the natural standard deviation of our sample (0.19 dex), and therefore these two colors do not provide a very sensitive metallicity diagnostic. We are unable to find any color-color metallicity sensitive index that relies solely on measurements in the Sloan optical bands.

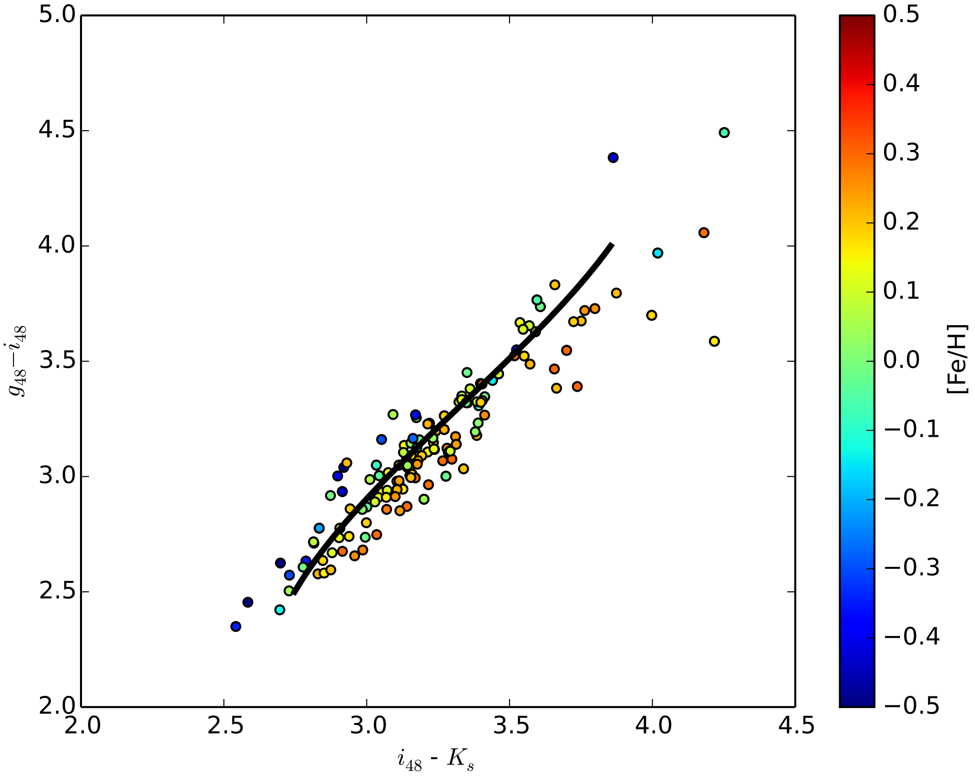

Figure 5.8: $g_{48} - i_{48}$ vs $i_{48} - K_s$ for our target M dwarfs. Each data point is colored with the spectroscopic metallicity determined by Newton et al. (2015a). We show an interpolated [Fe/H] = 0 main sequence in black. Our interpolation is able to reproduce these spectroscopically determined metallicities with a median absolute deviation of 0.065 dex, and a standard deviation of 0.107 dex, comparable to the precision of the spectroscopically determined parameters themselves. Including a near-infrared magnitude in our color-color relations significantly improves our ability to determine the metallicity of M dwarfs, and will be essential if M dwarfs are to be used as probes of Galactic structure and assembly.

5.4.3 Potential Effects of Activity, Age, and Surface Gravity

When calibrating broadband photometric relations to stellar physical parameters, like metallicity, it is important to consider possible systematic effects associated with other physical parameters of the star. Low-mass subdwarf stars are older, smaller, low metallicity stars that are kinematically associated with the Galactic halo. Their smaller sizes means that at a given color, a subdwarf will have a dimmer absolute magnitude (Lépine et al. 2007), moving the target lower in the plots in Figure 5.5, as well as in Figure 3.3. This method would assume, however, that these stars were low mass main sequence stars instead ofe sub dwarfs, and therefore underestimate their mass. Since we would erroneously believe the star to be a lower mass (instead of a subdwarf), we would also believe that the star had a lower metallicity than it actually had.

Lépine et al. (2007) found that dwarfs and subdwarfs can be distinguished by where they fall in the [CaH2+CaH3,TiO5] spectral indices diagram. However, this method requires the collection of optical spectra for all of our targets, which are not currently available. We are currently undertaking a survey to collect low resolution optical spectra of many of our targets, however. In the Solar Neighborhood, the population of stars is dominated by the thin disk, and the relative number of halo subdwarfs is expected to be small, and therefore we do not believe that subdwarf contamination is a significant effect on our results. Similarly, we ignore potential contamination from young stars, as the relative number of young systems in our sample of field stars should be small.

Activity and surface gravity are additional eternal parameters which may significantly affect a target M dwarf's color, aside from metallicity. More active stars with stronger magnetic fields may be able to inflate the upper atmosphere of the star.

Because this is where the emergent stellar spectrum is generated, the spectrum will have a lower surface gravity than for a comparatively inactive star of the same spectral type. This will decrease the width of the spectral features throughout the spectrum and in all photometric passbands. Because of this, it is not possible to say a priori how the color of an M dwarf will change with a corresponding change in magnetic field as the effect will depend on the relative strength change of the lines within each passband. We have not calibrated this effect in this chapter or in chapter three. Additionally, the effect of surface gravity and stellar activity was not calibrated in the original spectroscopic determinations of our M dwarfs, as the spectral measurements themselves are calibrated off of wide FGK - M star binaries for which the metallicity was determined from the more massive primary star and correlated with M dwarf spectral features - irrespective of the M dwarfs potential activity. Therefore, this potential systematic effect is embedded at a fundamental level within our sample. These effects, if left uncalibrated, may represent a lower limit of precision photometric metallicity calibrations may achieve, and larger samples are needed in order to calibrate all of these potential effects. However, we have shown that these photometric measurements are correlated with spectroscopically based metallicity determinations, and we believe that the majority of the photometric variation seen in the M dwarf population can be attributed to the effects of metallicity.

5.4.4 Implications for the Large Synoptic Survey Telescope (LSST)

We have found that there is no precise color-color-metallicity relation for M dwarfs that relies solely on the optical $g_{48}r_{48}i_{48}z_{48}$ magnitudes of an M dwarf. In order to accurately determine an M dwarf's metallicity using photometric data alone, a near infrared magnitude measurement is essential. LSST will observe the entire southern sky every few days with an 8 meter telescope in the Sloan photometric system. However, LSST will not observe in the near infrared J, H, or K_s bands. While the survey will discovery millions of M dwarfs in the Milky Way with its unprecedented depth, one would not be able to determine stellar metallicities solely from these data, and therefore they will not be useable for determining the chemical structure of the Milky Way. Losing the lower mass end of the main sequence is detrimental, as on average the M dwarfs should be older than other dwarf stars in the Milky Way, as their main sequence lifetimes are greater than a Hubble time. Therefore, M dwarfs have the potential to probe the earliest formation epoch of the Milky Way, provided their kinematic history hasn't been erased and can be recovered. Furthermore, being at the lowest mass end of the main-sequence, any changes in the initial mass function over the lifetime of the Milky Way will be felt most strongly by stars on extremes of the main sequence. For these reasons, it is essential that LSST be able to measure the metallicities of the M dwarfs it discovers.

The VISTA survey is a European survey aiming to map the Southern hemisphere in the 2MASS J and K_s bands to a limiting magnitude of $J = 20.2$ and $K_s = 18.5$, significantly deeper than the 2MASS catalog. Due to the red colors of M dwarfs, many of the new M dwarfs detected by LSST at optical passbands will have a counterpart detected in the VISTA Hemisphere Survey. These two data sets, when combined, will allow the photometric determination of the metallicities of M dwarfs throughout the Galaxy and enable their use as chemical probes of the Milky Way.

5.5 Conclusions

We used the 48-inch telescope and KeplerCam at the FLWO on Mt. Hopkins, AZ to measure Sloan *griz* magnitudes for 150 Northern hemisphere solar neighborhood M dwarfs. By combining these measurements with known trigonometric parallaxes and spectroscopic metallicity measurements from Newton et al. (2015a), we have calibrated a new color-magnitude-metallicity relation and a color-color-metallicity relation. We find that the location of an M dwarf in the M_K (or M_i) vs $g_{48} - i_{48}$ plane is a metallicity indicator with a standard deviation of 0.114 (or 0.118) dex.

We further find that metallicity indicators that do not rely on a distance measurement but solely on an optical colors are unable to accurately determine the metallicity of an M dwarf. Previous SDSS color-color relations that correlated with the spectroscopic ζ parameter (itself believed to be a metallicity indicator) are shown not to be effective. We ascribe this result to known shifts in the SDSS r-band filter relative to the r' and r_{48} filter.

We have found an accurate color-color-metallicity relation that utilizes a near infrared magnitude in one of its colors. We find that the location of an M dwarf in the $g_{48} - i_{48}$ vs. $i_{48} - K_s$ color plane is a robust indicator of the star's metallicity, with a standard deviation of 0.096 dex. In order for future all sky surveys to take advantage of this relationship, LSST and VISTA sources will have to be cross-matched.

Acknowledgments

This publication was made possible through the support of a grant from the John Templeton Foundation. The opinions expressed in this publication are those of the authors and do not necessarily reflect the views of the John Templeton Foundation. This research has made extensive use of data products from the Two Micron All Sky Survey, which is a joint project of the University of Massachusetts and the Infrared Processing and Analysis Center/California Institute of Technology. This research has made extensive use of NASAs Astrophysics Data System (ADS), and the SIMBAD database, operated at CDS, Strasbourg, France.

Table 5.1:: Filter transmission for the FLWO 48-inch telescope

Filter	Wavelength (nm)	Percent Transmission
u	200	0.00000
u	201	0.00016
u	202	0.00032
u	203	0.00000
u	204	0.00001
...	...	...

Table 5.2:: Atmospheric Parameters in the Sloan Filters for Observed Nights

Date	$k_{1,g}$	$k_{2,g}$	z_g	$k_{1,r}$	$k_{2,r}$	z_r	$k_{1,i}$	$k_{2,i}$	z_i
Oct 28, 2014	0.0992	0.0675	22.3995	0.0948	0.0236	22.4474	0.1162	-0.0032	22.0417
Nov 07, 2014	0.1205	-0.0040	22.3789	0.0884	-0.0033	22.4243	0.0702	0.0044	22.0105
Nov 08, 2014	0.3637	-0.0756	22.4633	0.2386	-0.0700	22.4462	0.1299	-0.0474	21.9779
Nov 09, 2014	0.1137	0.0414	22.3967	0.1147	-0.0023	22.4398	0.0827	0.0038	22.0139
Nov 27, 2014	-0.0256	0.0519	22.3125	0.0258	0.0110	22.3792	0.0323	0.0049	21.9712
Nov 28, 2014	0.1066	0.0517	22.3661	0.1461	-0.0188	22.4002	0.1480	-0.0426	21.9800
Nov 29, 2014	0.0381	0.0196	22.3093	-0.0112	-0.0070	22.3670	0.0571	-0.0027	21.9764
Jan 05, 2015	0.1406	0.0041	22.3123	0.0952	-0.0058	22.3406	0.0536	-0.0139	21.9233
Feb 05, 2015	0.1044	0.0012	22.2893	0.0560	-0.0025	22.3154	0.0502	-0.0061	21.8879
Mar 27, 2015	0.1715	0.0104	22.4375	0.0689	0.0286	22.5663	0.0343	0.0280	22.1434
Apr 01, 2015	-0.0070	0.0934	22.4178	0.0147	0.0469	22.5551	0.0127	0.0121	22.1200
Apr 07, 2015	0.2292	-0.0129	22.4160	0.1328	-0.0125	22.5236	0.2272	-0.0650	22.1083
Apr 22, 2015	0.2361	0.0538	22.3534	0.1470	0.0580	22.4539	-0.0256	0.2293	22.0138
Apr 30, 2015	0.2054	0.0041	22.3602	0.1130	0.0061	22.4567	0.0628	0.0037	22.0273
May 09, 2015	0.1510	0.0261	22.3690	0.1018	0.0064	22.4564	0.0573	0.0145	22.0421
Jun 01, 2015	0.1654	0.0447	22.3743	0.1036	0.1837	22.4485	0.0898	0.2853	22.0428

Table 5.2 (Continued):

$k_{1,z}$	$k_{2,z}$	z_z	MAD (mag)
0.1342	-0.0229	21.1940	0.0079
0.0582	-0.0173	21.1696	0.0107
0.1344	-0.0515	21.1343	0.0201
0.1003	-0.0166	21.1592	0.0100
0.0770	-0.0158	21.1635	0.0097
0.2073	-0.0909	21.1496	0.0233
0.1677	-0.0415	21.1811	0.0195
0.0414	-0.0177	21.1413	0.0066
0.0534	-0.0092	21.0751	0.0044
0.0392	0.0187	21.2748	0.0075
0.0503	-0.0057	21.2394	0.0106
0.1355	-0.0151	21.2019	0.0100
0.0819	0.0761	21.1581	0.0169
0.0723	0.0082	21.1360	0.0246
0.0166	0.0325	21.1665	0.0098
0.0470	0.0523	21.1385	0.0217

Table 5.3:: 48-inch Sloan *griz* magnitudes for USNO Sloan $g'r'i'z'$ standard stars

Star Name	m_g	σ_g^a	N_{obs}	m_r	σ_r	N_{obs}	m_i	σ_i	N_{obs}	m_z	σ_z	N_{obs}^b
SA115-420	11.395	0.027	20	11.095	0.023	20	11.001	0.011	20	10.996	0.011	20
SA104-428	13.061	0.022	22	12.316	0.012	21	12.034	0.028	21	11.893	0.016	21
SA94-251	11.779	0.044	22	10.790	0.027	22	10.397	0.024	22	10.174	0.031	22
SA114-654	12.161	0.009	15	11.741	0.086	14	11.584	0.015	14	11.537	0.019	14
SA114-656	13.094	0.011	15	12.351	0.015	14	12.051	0.014	14	11.885	0.021	14
...	...	...	...	...	...	...	...	...	...	...	...	...

a) Error is estimated from the scatter in all standard star measurements taken on photometric nights.

b) Each visit to a standard star generates two observations, as per our observing strategy. Occasionally, telescope automation glitches have resulted in one observation being made in a single visit.

Table 5.4:: 48-inch Sloan *griz* magnitudes for Northern hemisphere M dwarfs

Star	m_g	σ_g^a	MAD$_g^b$	N$_{obs}$	m_r	σ_r^a	MAD_r^b	N$_{obs}$	m_i	σ_i^a	MAD_i^b	N$_{obs}$
J2343+3632	13.434	0.002	0.009	4	11.996	0.004	0.009	4	10.386	0.008	0.009	4
J2223+3227	11.482	0.001	0.008	2	10.139	0.002	0.008	2	8.901	0.003	0.008	2
J0144+1620	14.802	0.011	0.020	2	13.345	0.002	0.020	2	11.785	0.002	0.020	2
J1125+4319	15.843	0.061	0.025	2	14.442	0.099	0.025	2	12.809	0.058	0.025	2
J1413+0506W	14.917	0.002	0.010	2	13.562	0.002	0.010	2	12.060	0.004	0.010	2
...	...	...	...	...	...	...	...	...	...	...	...	...

Table 5.4 (Continued):

m_z	σ_z^a	MAD_z^b	N$_{obs}$
9.575	0.008	0.009	4
8.265	0.001	0.008	2
11.029	0.001	0.020	2
12.022	0.011	0.025	2
11.295	0.006	0.010	2
...	...	...	...

a) σ here means the square root of the variance (even when only 2 observations have been taken). High variance means that the individual measurements of the target stars were significantly different (even if only taken 10 minutes apart). If the reported value is high (> 0.05 mag), treat the reported magnitude with caution. Our small number of observations of individual target stars make us sensitive to stellar activity, for which we cannot correct.

b) Here, the MAD refers to the median absolute deviation of the residuals of all observations of all standard stars taken on the night the target M dwarf was observed. This is not a measure of the variation in the target star's magnitude, but actually a measure of how well we can constrain the properties of the atmosphere through our model on the night of observation. We believe this value to represent the true uncertainty on the magnitude measurements we present here.

Table 5.5:: [Fe/H] = 0.0 Main Sequence Colors and Absolute Magnitudes[a]

$g_{48} - i_{48}$	$i_{48} - K_s$	$i_{48} - z_{48}$	M_i	M_K
2.500	2.748	0.578	8.701	5.954
2.541	2.768	0.594	8.936	6.168
2.582	2.789	0.610	9.158	6.369
2.622	2.812	0.626	9.369	6.558
2.663	2.836	0.643	9.570	6.734
...	...	...	...	...

a) In all cases we have interpolated a [Fe/H] = 0 main sequence using $g_{48} - i_{48}$, the spectroscopic metallicity, and the variable in one of the other 4 columns. We do not recommend using the $i_{48} - K_s$, $i_{48} - z_{48}$, M_i, or M_K columns with each other, as the interpolations that produced them are fitted independently.

References

Ahrens, D. 1994, Meteorology Today - an introduction to weather, climate and the environment (West Publishing Co. 5th ed.)

Allard, F., Hauschildt, P. H., Alexander, D. R., & Starrfield, S. 1997, ARA&A, 35, 137

Alonso-Floriano, F. J., et al. 2015, A&A, 577, A128

Andersen, J. 1991, A&A Rev., 3, 91

Anglada-Escudé, G., Rojas-Ayala, B., Boss, A. P., Weinberger, A. J., & Lloyd, J. P. 2013a, A&A, 551, A48

—. 2013b, A&A, 551, A48

Armitage, P. J. 2003, ApJ, 582, L47

Bakos, G. Á., Lázár, J., Papp, I., Sári, P., & Green, E. M. 2002, PASP, 114, 974

Ballard, S., & Johnson, J. A. 2016, ApJ, 816, 66

Baraffe, I., Chabrier, G., Allard, F., & Hauschildt, P. H. 1998, A&A, 337, 403

Baraffe, I., Homeier, D., Allard, F., & Chabrier, G. 2015, A&A, 577, A42

Barrell, H. 1951, J. Opt. Soc. Am., 41, 295

Bayless, A. J., & Orosz, J. A. 2006, ApJ, 651, 1155

Bean, J. L., et al. 2011, ApJ, 743, 92

Benedict, G. F., McArthur, B. E., Franz, O. G., Wasserman, L. H., & Henry, T. J. 2000, AJ, 120, 1106

Benedict, G. F., et al. 1999, AJ, 118, 1086

—. 2001, AJ, 121, 1607

Berta, Z. K., Irwin, J., & Charbonneau, D. 2013, ApJ, 775, 91

Berta, Z. K., Irwin, J., Charbonneau, D., Burke, C. J., & Falco, E. E. 2012a, AJ, 144, 145

Berta, Z. K., et al. 2012b, ApJ, 747, 35

Berta-Thompson, Z. K., et al. 2015, Nature, 527, 204

Bessel, F. W. 1838, Astronomische Nachrichten, 16, 65

Bessell, M. S. 1991, AJ, 101, 662

Beuzit, J.-L., et al. 2004a, A&A, 425, 997

—. 2004b, A&A, 425, 997

Biazzo, K., et al. 2015, A&A, 583, A135

Bigourdan, G. 1909, Bulletin Astronomique, Serie I, 26, 466

Blake, C. H., Torres, G., Bloom, J. S., & Gaudi, B. S. 2008, ApJ, 684, 635

Bochanski, J. J., Hawley, S. L., Covey, K. R., West, A. A., Reid, I. N., Golimowski, D. A., & Ivezić, Ž. 2010, AJ, 139, 2679

Bochanski, J. J., Hawley, S. L., Reid, I. N., Covey, K. R., West, A. A., Tinney, C. G., & Gizis, J. E. 2005, AJ, 130, 1871

Bonfils, X., Delfosse, X., Udry, S., Santos, N. C., Forveille, T., & Ségransan, D. 2005, A&A, 442, 635

Bonfils, X., et al. 2013, A&A, 549, A109

Bowler, B. P., Liu, M. C., Shkolnik, E. L., & Tamura, M. 2015, ApJS, 216, 7

Boyajian, T., et al. 2015, MNRAS, 447, 846

Boyajian, T. S., et al. 2012, ApJ, 757, 112

Brown, T. M., Latham, D. W., Everett, M. E., & Esquerdo, G. A. 2011, AJ, 142, 112

Buchhave, L. A., & Latham, D. W. 2015, ApJ, 808, 187

Buchhave, L. A., et al. 2010, ApJ, 720, 1118

—. 2012a, Nature, 486, 375

—. 2012b, Nature, 486, 375

—. 2014a, Nature, 509, 593

—. 2014b, Nature, 509, 593

Burke, C. J., et al. 2015, ApJ, 809, 8

Carter, J. A., et al. 2011a, Science, 331, 562

—. 2011b, Science, 331, 562

Chabrier, G., & Baraffe, I. 1997, A&A, 327, 1039

Chabrier, G., Baraffe, I., & Plez, B. 1996, ApJ, 459, L91

Charbonneau, D., Brown, T. M., Latham, D. W., & Mayor, M. 2000, ApJ, 529, L45

Charbonneau, D., Brown, T. M., Noyes, R. W., & Gilliland, R. L. 2002, ApJ, 568, 377

Charbonneau, D., et al. 2009, Nature, 462, 891

Ciddor, P. E. 1996, Applied Optics, 35, 1566

Claret, A. 2000, VizieR Online Data Catalog, 336, 31081

Clem, J. L., & Landolt, A. U. 2013, AJ, 146, 88

Close, L. M., Siegler, N., Freed, M., & Biller, B. 2003, ApJ, 587, 407

Cosentino, R., et al. 2012, in Proc. SPIE, Vol. 8446, Ground-based and Airborne Instrumentation for Astronomy IV, 84461V

Coughlin, J. L., et al. 2015, ArXiv e-prints

Crane, J. D., Shectman, S. A., Butler, R. P., Thompson, I. B., Birk, C., Jones, P., & Burley, G. S. 2010, in Proc. SPIE, Vol. 7735, Ground-based and Airborne Instrumentation for Astronomy III, 773553

Croll, B., Albert, L., Jayawardhana, R., Miller-Ricci Kempton, E., Fortney, J. J., Murray, N., & Neilson, H. 2011, ApJ, 736, 78

Crossfield, I. J. M., Barman, T., & Hansen, B. M. S. 2011, ApJ, 736, 132

Cruz, K. L., & Reid, I. N. 2002, AJ, 123, 2828

Cruz, K. L., Reid, I. N., Liebert, J., Kirkpatrick, J. D., & Lowrance, P. J. 2003, AJ, 126, 2421

Cruz, K. L., et al. 2007, AJ, 133, 439

Daemgen, S., Siegler, N., Reid, I. N., & Close, L. M. 2007, ApJ, 654, 558

Dahn, C. C., et al. 1976, Publications of the U.S. Naval Observatory Second Series, 24, 1

—. 2002, AJ, 124, 1170

Danchi, W. C., & Lopez, B. 2013, ApJ, 769, 27

de Mooij, E. J. W., et al. 2013, ApJ, 771, 109

Delfosse, X., Forveille, T., Beuzit, J.-L., Udry, S., Mayor, M., & Perrier, C. 1999, A&A, 344, 897

Delfosse, X., Forveille, T., Ségransan, D., Beuzit, J.-L., Udry, S., Perrier, C., & Mayor, M. 2000, A&A, 364, 217

Désert, J.-M., et al. 2011, ApJ, 731, L40

Deshpande, R., et al. 2013, AJ, 146, 156

Dierckx, P. 1981, IMA J. Num. Anal., 267

Dieterich, S. B., Henry, T. J., Jao, W.-C., Winters, J. G., Hosey, A. D., Riedel, A. R., & Subasavage, J. P. 2014, AJ, 147, 94

Dittmann, J. A., Close, L. M., Green, E. M., & Fenwick, M. 2009a, ApJ, 701, 756

Dittmann, J. A., Close, L. M., Green, E. M., Scuderi, L. J., & Males, J. R. 2009b, ApJ, 699, L48

Dittmann, J. A., Close, L. M., Scuderi, L. J., & Morris, M. D. 2010, ApJ, 717, 235

Dittmann, J. A., Close, L. M., Scuderi, L. J., Turner, J., & Stephenson, P. C. 2012, New Astronomy, 17, 438

Dittmann, J. A., Irwin, J. M., Charbonneau, D., & Berta-Thompson, Z. K. 2014a, ApJ, 784, 156

—. 2014b, ApJ, 784, 156

Dittmann, J. A., Irwin, J. M., Charbonneau, D., & Newton, E. R. 2016, ApJ, 818, 153

Donati, J.-F., Forveille, T., Collier Cameron, A., Barnes, J. R., Delfosse, X., Jardine, M. M., & Valenti, J. A. 2006, Science, 311, 633

Doyle, L. R., et al. 2011, Science, 333, 1602

Dressing, C. D., & Charbonneau, D. 2013, ApJ, 767, 95

—. 2015, ApJ, 807, 45

Ducourant, C., Dauphole, B., Rapaport, M., Colin, J., & Geffert, M. 1998, A&A, 333, 882

Dumusque, X., et al. 2014, ApJ, 789, 154

—. 2015, ApJ, 814, L21

Dunham, E. W., Mandushev, G. I., Taylor, B. W., & Oetiker, B. 2004, PASP, 116, 1072

Dupuy, T. J., & Liu, M. C. 2012, ApJS, 201, 19

Eggen, O. J., & Sandage, A. 1967, ApJ, 148, 911

Everett, M. E., Howell, S. B., Silva, D. R., & Szkody, P. 2013, ApJ, 771, 107

Faherty, J. K., et al. 2012, ApJ, 752, 56

Faria, J. P., et al. 2016, ArXiv e-prints

Filippenko, A. V. 1982, PASP, 94, 715

Fischer, D. A., & Marcy, G. W. 1992, ApJ, 396, 178

Fischer, D. A., & Valenti, J. 2005, ApJ, 622, 1102

Foreman-Mackey, D., Hogg, D. W., Lang, D., & Goodman, J. 2013, PASP, 125, 306

Forveille, T., et al. 2005, A&A, 435, L5

Fraine, J. D., et al. 2013, ApJ, 765, 127

Fressin, F., et al. 2013, ApJ, 766, 81

Fuchs, B., et al. 2009, AJ, 137, 4149

Fukugita, M., Ichikawa, T., Gunn, J. E., Doi, M., Shimasaku, K., & Schneider, D. P. 1996, AJ, 111, 1748

Gaidos, E. 2013, ApJ, 770, 90

Gaidos, E., Fischer, D. A., Mann, A. W., & Lépine, S. 2012, ApJ, 746, 36

Gaidos, E., et al. 2014, MNRAS, 443, 2561

Gatewood, G. 2008, AJ, 136, 452

Gatewood, G., & Coban, L. 2009, AJ, 137, 402

Gatewood, G., de Jonge, K. J., & Stephenson, B. 1993, PASP, 105, 1101

Gettel, S., et al. 2016, ApJ, 816, 95

Giclas, H. L., Burnham, R., & Thomas, N. G. 1971, Lowell proper motion survey Northern Hemisphere. The G numbered stars. 8991 stars fainter than magnitude 8 with motions > 0".26/year (Flagstaff, Arizona: Lowell Observatory, 1971)

Giclas, H. L., Burnham, Jr., R., & Thomas, N. G. 1978, Lowell Observatory Bulletin, 8, 89

Gillon, M., Jehin, E., Delrez, L., Magain, P., Opitom, C., & Sohy, S. 2013, in Protostars and Planets VI, Heidelberg, July 15-20, 2013. Poster #2K066, 66

Gizis, J., & Reid, I. N. 1995, AJ, 110, 1248

Gizis, J. E. 1997, AJ, 113, 806

—. 1998, AJ, 115, 2053

Gizis, J. E., Monet, D. G., Reid, I. N., Kirkpatrick, J. D., & Burgasser, A. J. 2000a, MNRAS, 311, 385

Gizis, J. E., Monet, D. G., Reid, I. N., Kirkpatrick, J. D., Liebert, J., & Williams, R. J. 2000b, AJ, 120, 1085

Gizis, J. E., & Reid, I. N. 1997, PASP, 109, 849

Gizis, J. E., & Reid, N. I. 1996, AJ, 111, 365

Gliese, W., Jahreiss, H., & Upgren, A. R. 1986, in The Galaxy and the Solar System, ed. R. Smoluchowski, J. M. Bahcall, & M. S. Matthews, 13–34

Gómez Maqueo Chew, Y., et al. 2014, A&A, 572, A50

Gressler, W., et al. 2014, in Proc. SPIE, Vol. 9145, Ground-based and Airborne Telescopes V, 91451A

Harrington, R. S., & Dahn, C. C. 1980, AJ, 85, 454

—. 1984, IAU Circ., 3989, 1

Harrington, R. S., et al. 1993, AJ, 105, 1571

Hartman, J. D., Bakos, G. Á., Noyes, R. W., Sipőcz, B., Kovács, G., Mazeh, T., Shporer, A., & Pál, A. 2011a, AJ, 141, 166

—. 2011b, AJ, 141, 166

Haykin, S. 1998, Neural Networks: A Comprehensive Foundation, 2nd edn. (Upper Saddle River, NJ, USA: Prentice Hall PTR)

Haywood, M. 2001, MNRAS, 325, 1365

Hébrard, G., et al. 2013, A&A, 554, A114

Hellier, C., et al. 2011, in European Physical Journal Web of Conferences, Vol. 11, European Physical Journal Web of Conferences, 01004

Helling, C., & Casewell, S. 2014, A&A Rev., 22, 80

Helmi, A., White, S. D. M., de Zeeuw, P. T., & Zhao, H. 1999, Nature, 402, 53

Henry, T. J., Franz, O. G., Wasserman, L. H., Benedict, G. F., Shelus, P. J., Ianna, P. A., Kirkpatrick, J. D., & McCarthy, Jr., D. W. 1999a, ApJ, 512, 864

—. 1999b, ApJ, 512, 864

Henry, T. J., Ianna, P. A., Kirkpatrick, J. D., & Jahreiss, H. 1997, AJ, 114, 388

Henry, T. J., Jao, W.-C., Subasavage, J. P., Beaulieu, T. D., Ianna, P. A., Costa, E., & Méndez, R. A. 2006, AJ, 132, 2360

Henry, T. J., Kirkpatrick, J. D., & Simons, D. A. 1994, AJ, 108, 1437

Henry, T. J., & McCarthy, Jr., D. W. 1993, AJ, 106, 773

Henry, T. J., Subasavage, J. P., Brown, M. A., Beaulieu, T. D., Jao, W.-C., & Hambly, N. C. 2004, AJ, 128, 2460

Henry, T. J., Walkowicz, L. M., Barto, T. C., & Golimowski, D. A. 2002, AJ, 123, 2002

Hoaglin, D. C., Mosteller, F., & Tukey, J. W. 1983, Understanding robust and exploratory data analysis (Wiley-Interscience)

Hosey, A. D., Henry, T. J., Jao, W.-C., Dieterich, S. B., Winters, J. G., Lurie, J. C., Riedel, A. R., & Subasavage, J. P. 2015, AJ, 150, 6

Howard, A. W., et al. 2012, ApJS, 201, 15

Ireland, M. J., Kraus, A., Martinache, F., Lloyd, J. P., & Tuthill, P. G. 2008, ApJ, 678, 463

Irwin, J., Berta, Z. K., Burke, C. J., Charbonneau, D., Nutzman, P., West, A. A., & Falco, E. E. 2011a, ApJ, 727, 56

Irwin, J., et al. 2009a, ApJ, 701, 1436

—. 2009b, ApJ, 701, 1436

—. 2010, ApJ, 718, 1353

Irwin, J. M., Berta-Thompson, Z. K., Charbonneau, D., Dittmann, J., Falco, E. E., Newton, E. R., & Nutzman, P. 2015, in Cambridge Workshop on Cool Stars, Stellar Systems, and the Sun, Vol. 18, Cambridge Workshop on Cool Stars, Stellar Systems, and the Sun, ed. G. T. van Belle & H. C. Harris, 767–772

Irwin, J. M., et al. 2011b, ApJ, 742, 123

Irwin, M. J. 1985, MNRAS, 214, 575

Janson, M., Bergfors, C., Brandner, W., Kudryavtseva, N., Hormuth, F., Hippler, S., & Henning, T. 2014, ApJ, 789, 102

Janson, M., et al. 2012a, ApJ, 754, 44

—. 2012b, ApJ, 754, 44

Jao, W.-C., Henry, T. J., Subasavage, J. P., Brown, M. A., Ianna, P. A., Bartlett, J. L., Costa, E., & Méndez, R. A. 2005, AJ, 129, 1954

Jao, W.-C., Henry, T. J., Subasavage, J. P., Winters, J. G., Riedel, A. R., & Ianna, P. A. 2011, AJ, 141, 117

Jenkins, J. S., Ramsey, L. W., Jones, H. R. A., Pavlenko, Y., Gallardo, J., Barnes, J. R., & Pinfield, D. J. 2009, ApJ, 704, 975

Jenkins, L. F. 1952, General catalogue of trigonometric stellar parallaxes. ([New Haven, Yale University Observatory] 1952.)

Johns-Krull, C. M., & Valenti, J. A. 1996, ApJ, 459, L95

Johnson, J. A., & Apps, K. 2009, ApJ, 699, 933

Kapteyn, J. C. 1900, Publications of the Kapteyn Astronomical Laboratory Groningen, 1, 3

Khodachenko, M. L., et al. 2007, Astrobiology, 7, 167

Khrutskaya, E. V., Izmailov, I. S., & Khovrichev, M. Y. 2010, Astronomy Letters, 36, 576

Kirkpatrick, J. D., Beichman, C. A., & Skrutskie, M. F. 1997, ApJ, 476, 311

Kirkpatrick, J. D., Henry, T. J., & McCarthy, Jr., D. W. 1991, ApJS, 77, 417

Kirkpatrick, J. D., Henry, T. J., & Simons, D. A. 1995, AJ, 109, 797

Kirkpatrick, J. D., et al. 2000, AJ, 120, 447

Kopparapu, R. K., et al. 2013, ApJ, 765, 131

Kuiper, G. P. 1936, ApJ, 84, 359

Lacy, C. H. 1977, ApJ, 218, 444

Landolt, A. U. 1992, AJ, 104, 340

—. 2009, AJ, 137, 4186

—. 2013, AJ, 146, 131

Law, N. M., Hodgkin, S. T., & Mackay, C. D. 2006, MNRAS, 368, 1917

—. 2008, MNRAS, 384, 150

Lépine, S. 2005, AJ, 130, 1680

Lépine, S., & Gaidos, E. 2011, AJ, 142, 138

Lépine, S., Hilton, E. J., Mann, A. W., Wilde, M., Rojas-Ayala, B., Cruz, K. L., & Gaidos, E. 2013a, AJ, 145, 102

—. 2013b, AJ, 145, 102

Lépine, S., Rich, R. M., Neill, J. D., Caulet, A., & Shara, M. M. 2002a, ApJ, 581, L47

Lépine, S., Rich, R. M., & Shara, M. M. 2003, AJ, 125, 1598

—. 2007, ApJ, 669, 1235

Lépine, S., & Shara, M. M. 2005, AJ, 129, 1483

Lépine, S., Shara, M. M., & Rich, R. M. 2002b, AJ, 123, 3434

Lépine, S., Thorstensen, J. R., Shara, M. M., & Rich, R. M. 2009, AJ, 137, 4109

Lindegren, L., & Perryman, M. A. C. 1998, Highlights of Astronomy, 11, 581

Luyten, W. J. 1979, New Luyten catalogue of stars with proper motions larger than two tenths of an arcsecond; and first supplement; NLTT. (Minneapolis (1979))

Mahadevan, S., et al. 2012, in Society of Photo-Optical Instrumentation Engineers (SPIE) Conference Series, Vol. 8446, Society of Photo-Optical Instrumentation Engineers (SPIE) Conference Series

Makarov, V. V., Zacharias, N., Hennessy, G. S., Harris, H. C., & Monet, A. K. B. 2007, ApJ, 668, L155

Mandel, K., & Agol, E. 2002, ApJ, 580, L171

Mann, A. W., Brewer, J. M., Gaidos, E., Lépine, S., & Hilton, E. J. 2013a, AJ, 145, 52

—. 2013b, AJ, 145, 52

Mann, A. W., Deacon, N. R., Gaidos, E., Ansdell, M., Brewer, J. M., Liu, M. C., Magnier, E. A., & Aller, K. M. 2014, AJ, 147, 160

Mann, A. W., Gaidos, E., Lépine, S., & Hilton, E. J. 2012, ApJ, 753, 90

Martin, E. L., & Kun, M. 1996, A&AS, 116, 467

Mason, B. D., Wycoff, G. L., Hartkopf, W. I., Douglass, G. G., & Worley, C. E. 2001, AJ, 122, 3466

Mayor, M., & Queloz, D. 1995, Nature, 378, 355

McCarthy, C., Zuckerman, B., & Becklin, E. E. 2001, AJ, 121, 3259

McCullough, P. R., Stys, J. E., Valenti, J. A., Fleming, S. W., Janes, K. A., & Heasley, J. N. 2005, PASP, 117, 783

McMahon, R. 2012, in Science from the Next Generation Imaging and Spectroscopic Surveys, 37

Metcalfe, T. S., Mathieu, R. D., Latham, D. W., & Torres, G. 1996, ApJ, 456, 356

Monet, D. G., Dahn, C. C., Vrba, F. J., Harris, H. C., Pier, J. R., Luginbuhl, C. B., & Ables, H. D. 1992, AJ, 103, 638

Montagnier, G., et al. 2006, A&A, 460, L19

Morales, J. C., et al. 2009, ApJ, 691, 1400

Morton, T. D., & Swift, J. J. 2013, submitted, ArXiv:1303.3013

Motalebi, F., et al. 2015, A&A, 584, A72

Moutou, C., Coustenis, A., Schneider, J., St Gilles, R., Mayor, M., Queloz, D., & Kaufer, A. 2001, A&A, 371, 260

Muñoz, D. J., Lai, D., & Liu, B. 2016, ArXiv e-prints

Muirhead, P. S., et al. 2015, ApJ, 801, 18

Murgas, F., Pallé, E., Cabrera-Lavers, A., Colón, K. D., Martín, E. L., & Parviainen, H. 2012, A&A, 544, A41

Nefs, S. V., et al. 2013, MNRAS, 431, 3240

Neves, V., et al. 2012, A&A, 538, A25

Newton, E. R., Charbonneau, D., Irwin, J., Berta-Thompson, Z. K., Rojas-Ayala, B., Covey, K., & Lloyd, J. P. 2014, AJ, 147, 20

Newton, E. R., Charbonneau, D., Irwin, J., & Mann, A. W. 2015a, ApJ, 800, 85

Newton, E. R., Irwin, J., Charbonneau, D., Berta-Thompson, Z. K., Dittmann, J. A., & West, A. A. 2015b, ArXiv e-prints

Nutzman, P., & Charbonneau, D. 2008, PASP, 120, 317

Penev, K., et al. 2013, AJ, 145, 5

Pepper, J., et al. 2007, PASP, 119, 923

Perryman, M. A. C., et al. 1997, A&A, 323, L49

Petigura, E. A., Howard, A. W., & Marcy, G. W. 2013, Proceedings of the National Academy of Science, 110, 19273

Pickles, A. J. 1998, PASP, 110, 863

Pinsonneault, M. H., Stauffer, J., Soderblom, D. R., King, J. R., & Hanson, R. B. 1998, ApJ, 504, 170

Pollacco, D. L., et al. 2006, PASP, 118, 1407

Popper, D. M., & Etzel, P. B. 1981, AJ, 86, 102

Pravdo, S. H., Shaklan, S. B., Henry, T., & Benedict, G. F. 2004, ApJ, 617, 1323

Pravdo, S. H., Shaklan, S. B., Lloyd, J., & Benedict, G. F. 2005, in Astronomical Society of the Pacific Conference Series, Vol. 338, Astrometry in the Age of the Next Generation of Large Telescopes, ed. P. K. Seidelmann & A. K. B. Monet, 288

Pravdo, S. H., Shaklan, S. B., Wiktorowicz, S. J., Kulkarni, S., Lloyd, J. P., Martinache, F., Tuthill, P. G., & Ireland, M. J. 2006, ApJ, 649, 389

Quirrenbach, A., et al. 2012, in Society of Photo-Optical Instrumentation Engineers (SPIE) Conference Series, Vol. 8446, Society of Photo-Optical Instrumentation Engineers (SPIE) Conference Series

Radovan, M. V., et al. 2014, in Proc. SPIE, Vol. 9145, Ground-based and Airborne Telescopes V, 91452B

Reid, I. N., Cruz, K. L., & Allen, P. R. 2007, AJ, 133, 2825

Reid, I. N., Cruz, K. L., Kirkpatrick, J. D., Allen, P. R., Mungall, F., Liebert, J., Lowrance, P., & Sweet, A. 2008, AJ, 136, 1290

Reid, I. N., & Gizis, J. E. 2005, PASP, 117, 676

Reid, I. N., Gizis, J. E., Kirkpatrick, J. D., & Koerner, D. W. 2001, AJ, 121, 489

Reid, I. N., Hawley, S. L., & Gizis, J. E. 1995, AJ, 110, 1838

Reid, I. N., Kirkpatrick, J. D., Liebert, J., Gizis, J. E., Dahn, C. C., & Monet, D. G. 2002, AJ, 124, 519

Reid, I. N., et al. 2003a, AJ, 125, 354

—. 2003b, AJ, 126, 3007

—. 2004a, AJ, 128, 463

—. 2004b, AJ, 128, 463

Reid, N. 1998, AJ, 115, 204

Reshetov, V., Herriot, G., Thibault, S., Désaulniers, P., Saddlemyer, L., & Loop, D. 2012, in Society of Photo-Optical Instrumentation Engineers (SPIE) Conference Series, Vol. 8446, Society of Photo-Optical Instrumentation Engineers (SPIE) Conference Series

Riaz, B., Gizis, J. E., & Harvin, J. 2006, AJ, 132, 866

Ribas, I. 2003, A&A, 398, 239

Ricker, G. R., et al. 2015, Journal of Astronomical Telescopes, Instruments, and Systems, 1, 014003

Riedel, A. R., Murphy, S. J., Henry, T. J., Melis, C., Jao, W.-C., & Subasavage, J. P. 2011, AJ, 142, 104

Riedel, A. R., et al. 2010, AJ, 140, 897

—. 2014, AJ, 147, 85

Robin, A. C., Reylé, C., Derrière, S., & Picaud, S. 2003, A&A, 409, 523

Rojas-Ayala, B., Covey, K. R., Muirhead, P. S., & Lloyd, J. P. 2010, ApJ, 720, L113

—. 2012, ApJ, 748, 93

Ross, F. E. 1939, AJ, 48, 163

Rupprecht, G., et al. 2004, in Proc. SPIE, Vol. 5492, Ground-based Instrumentation for Astronomy, ed. A. F. M. Moorwood & M. Iye, 148–159

Saar, S. H. 1996, in Magnetodynamic Phenomena in the Solar Atmosphere: Prototypes of Stellar Magnetic Activity, ed. Y. Uchida, T. Kosugi, & H. S. Hudson (Dordrecht: Kluwer Academics), 367–374

Salim, S., & Gould, A. 2003, ApJ, 582, 1011

Schlaufman, K. C. 2015, ApJ, 799, L26

Schlaufman, K. C., & Laughlin, G. 2010, A&A, 519, A105

—. 2011, ApJ, 738, 177

Schlesinger, F. 1904, ApJ, 20, 123

—. 1910a, Publications of the Allegheny Observatory of the University of Pittsburgh, 1, 1

—. 1910b, Publications of the Allegheny Observatory of the University of Pittsburgh, 1, 101

—. 1911, ApJ, 33, 8

—. 1924, Probleme der Astronomie, Seeliger Festschrift (Springer, Berlin)

Schlesinger, I. F. 1910c, ApJ, 32, 372

Scholz, R.-D., Meusinger, H., & Jahreiß, H. 2005, A&A, 442, 211

Schwamb, M. E., et al. 2013, ApJ, 768, 127

Seager, S., & Sasselov, D. D. 2000, ApJ, 537, 916

Shkolnik, E., Liu, M. C., & Reid, I. N. 2009, ApJ, 699, 649

Shkolnik, E. L., Anglada-Escudé, G., Liu, M. C., Bowler, B. P., Weinberger, A. J., Boss, A. P., Reid, I. N., & Tamura, M. 2012, ApJ, 758, 56

Shkolnik, E. L., Hebb, L., Liu, M. C., Reid, I. N., & Collier Cameron, A. 2010, ApJ, 716, 1522

Skrutskie, M. F., et al. 2000, VizieR Online Data Catalog, 2241, 0

Smart, R. L., Drimmel, R., Lattanzi, M. G., & Binney, J. J. 1998, Nature, 392, 471

Smart, R. L., Ioannidis, G., Jones, H. R. A., Bucciarelli, B., & Lattanzi, M. G. 2010, A&A, 514, A84

Smart, R. L., Lattanzi, M. G., Jahreiß, H., Bucciarelli, B., & Massone, G. 2007, A&A, 464, 787

Smith, J. A., et al. 2002, AJ, 123, 2121

Snellen, I. A. G. 2004, MNRAS, 353, L1

Solanki, S. K., Inhester, B., & Schüssler, M. 2006, Reports on Progress in Physics, 69, 563

Southworth, J. 2013, A&A, 557, A119

Southworth, J., Maxted, P. F. L., & Smalley, B. 2004, MNRAS, 351, 1277

Sozzetti, A., et al. 2013, in European Physical Journal Web of Conferences, Vol. 47, European Physical Journal Web of Conferences, 3006

Stauffer, J. R., Balachandran, S. C., Krishnamurthi, A., Pinsonneault, M., Terndrup, D. M., & Stern, R. A. 1997, ApJ, 475, 604

Stetson, P. B. 1990, PASP, 102, 932

Stone, R. C. 2002, PASP, 114, 1070

Tarter, J. C., et al. 2007, Astrobiology, 7, 30

Terrien, R. C., Mahadevan, S., Bender, C. F., Deshpande, R., Ramsey, L. W., & Bochanski, J. J. 2012, ApJ, 747, L38

Tinney, C. G. 1996, MNRAS, 281, 644

Torres, G. 2013, Astronomische Nachrichten, 334, 4

Torres, G., Andersen, J., & Giménez, A. 2010, A&A Rev., 18, 67

Upgren, A. R. 1996, QJRAS, 37, 453

Vaccaro, T. R., Rudkin, M., Kawka, A., Vennes, S., Oswalt, T. D., Silver, I., Wood, M., & Smith, J. A. 2007, ApJ, 661, 1112

van Altena, W. 1984, PASP, 96, 797

van Altena, W., & Hoffleit, D., eds. 1996a, Yale Parallax Catalogue

—. 1996b, Yale Parallax Catalogue

van Altena, W. F., & Lee, J. T. 1988, in IAU Symposium, Vol. 133, Mapping the Sky: Past Heritage and Future Directions, ed. S. Debarbat, 269 van Altena, W. F., Lee, J. T., & Hoffleit, E. D. 1995, The general catalogue of trigonometric [stellar] parallaxes

van de Kamp, P. 1935, AJ, 44, 74

van Leeuwen, F., ed. 2007a, Astrophysics and Space Science Library, Vol. 350, Hipparcos, the New Reduction of the Raw Data

van Leeuwen, F. 2007b, A&A, 474, 653

—. 2007c, A&A, 474, 653

—. 2007d, A&A, 474, 653

van Leeuwen, F., Evans, D. W., Grenon, M., Grossmann, V., Mignard, F., & Perryman, M. A. C. 1997, A&A, 323, L61

van Maanen, A. 1915, ApJ, 41, 187

Voges, W., et al. 2000, IAU Circ., 7432

Vrba, F. J., et al. 2004, AJ, 127, 2948

Wang, J., & Fischer, D. A. 2015, AJ, 149, 14

West, A. A., Hawley, S. L., Bochanski, J. J., Covey, K. R., Reid, I. N., Dhital, S., Hilton, E. J., & Masuda, M. 2008, AJ, 135, 785

West, A. A., Weisenburger, K. L., Irwin, J., Berta-Thompson, Z. K., Charbonneau, D., Dittmann, J., & Pineda, J. S. 2015, ApJ, 812, 3

West, A. A., et al. 2011a, AJ, 141, 97

—. 2011b, AJ, 141, 97

Winters, J. G., et al. 2015, AJ, 149, 5

Wolf, M. 1919, Veroeffentlichungen der Badischen Sternwarte zu Heidelberg, 7, 195

Worley, C. E. 1960, PASP, 72, 125

Wyttenbach, A., Ehrenreich, D., Lovis, C., Udry, S., & Pepe, F. 2015, A&A, 577, A62

Zhou, G., et al. 2015a, MNRAS, 451, 2263

—. 2015b, MNRAS, 451, 2263

Zickgraf, F.-J., Krautter, J., Reffert, S., Alcalá, J. M., Mujica, R., Covino, E., & Sterzik, M. F. 2005, A&A, 433, 151

Zucker, S., & Mazeh, T. 1994, ApJ, 420, 806